LASER INTERFEROMETER GRAVITATIONAL WAVE OBSERVATORY
- LIGO -
CALIFORNIA INSTITUTE OF TECHNOLOGY
MASSACHUSETTS INSTITUTE OF TECHNOLOGY

Technical Note	**LIGO-T070247-01-I**	**2008/04/08**

AdvLIGO Interferometer Sensing and Control Conceptual Design

Rich Abbott, Rana Adhikari, Stefan Ballmer, Lisa Barsotti, Matt Evans, Peter Fritschel, Valera Frolov, Guido Mueller, Bram Slagmolen, Sam Waldman

Distribution of this document:

ISC DRR/CDR Committee

This is an internal working note of the LIGO project

California Institute of Technology
LIGO Project, MS 18-34
Pasadena, CA 91125
Phone (626) 395-2129
Fax (626) 304-9834
E-mail: info@ligo.caltech.edu

Massachusetts Institute of Technology
LIGO Project, Room NW22-295
Cambridge, MA 02139
Phone (617) 253-4824
Fax (617) 253-7014
E-mail: info@ligo.mit.edu

LIGO Hanford Observatory
Route 10, Mile Marker 2
Richland, WA 99352
Phone (509) 372-8106
Fax (509) 372-8137
E-mail: info@ligo.caltech.edu

LIGO Livingston Observatory
19100 LIGO Lane
Livingston, LA 70754
Phone (225) 686-3100
Fax (225) 686-7189
E-mail: info@ligo.caltech.edu

http://www.ligo.caltech.edu/

Abstract

We present the conceptual design and supporting analysis for the Advanced LIGO Detector Interferometer Sensing and Control subsystem.

1 ISC subsystem description

1.1 Subsystem Context

The Interferometer Sensing and Control (ISC) Subsystem is responsible for maintaining optical resonance and optical alignment in the Dual-Recycled Fabry-Perot Michelson (DRFPM) interferometer. This includes photodetectors, demodulation electronics, A/D converter and the computer hard and software. ISC interfaces with the Suspension (SUS) Subsystem for the actuation on the optics, and with the Pre-Stabilized Laser (PSL) for actuation on the laser frequency. The design of the modulation and readout scheme is the responsibility of the ISC. The modulation is implemented by Input Optics (IO), according to the requirements of the ISC.

1.2 States of operation

The ISC system has to bring the interferometer from the unlocked stage to a configuration appropriate for collecting science data. This will involve the following states of operation:

1. Acquisition. In this state the length degrees-of-freedom go from being globally uncontrolled to globally controlled, and are brought to their operating points.

2. Transition. In this phase interferometer parameters such as control topology, input power and switchable filters are changed from the optimal values for lock acquisition to a configuration suitable for scientific data collecting.

3. Science mode. This is the traditional science mode as known from initial LIGO operation, during which science data is collected.

1.3 Modes of operation

The ISC system is being designed to operate in different science modes, which have different levels of operational complexity and different sensitivity spectra. Specifically we propose designing for the modes listed below, which we suggest are in roughly chronological order of implementation. Strain noise spectra for these modes are shown in Fig. 1 and operating parameters are given in Table 1.

mode 0 In this mode there is no signal recycling (SRM transmission of 100%), and modest input power (25 W). Since this configuration is so similar to the initial LIGO interferometer, we would expect to be able to get running in this mode fairly quickly, and start taking data with significantly better sensitivity than initial LIGO.

mode 1 In this mode there is broad-band signal recycling (i.e., no detuning of the signal recycling cavity). It appears to be easier to get good error signals for all the degrees-of-freedom in this mode, and of course there is no unstable optical spring to control. This mode could run with different input powers (the spectra for two are shown below), presumably starting with low power. At high power, the sensitivity to NS-NS inspirals is almost as good as can be achieved by specifically tuning for them.

mode 2 This is the canonical mode with full power and the SRC tuned to optimize sensitivity to NS-NS inspirals. We have however fixed the SRM transmission at 20%, which is a bit higher than the optimum for NS-NS sensitivity, as a compromise with the broad-band case (the difference is less than 0.4%).

mode 3 This mode optimizes for 30-30 solar mass BH-BH inspirals, with a fixed SRC detuning of 20 degrees and SRM transmission of 20% (i.e., laser power and homodyne phase are optimized). This corresponds to a particular achievable operating point of the SRC phase, as described later on.

mode 4 This mode optimizes laser power, homodyne phase and SRC phase for BH-BH (30 solar masses each) inspirals. This leads to a much higher SRC detuning than the preceding cases, which is more difficult to achieve with the sensing scheme. Note that this mode also gives very poor sensitivity about 100 Hz.

mode 5 This mode uses a smaller SRM transmission (1.1%) and full power to get improved sensitivity around 1 kHz. Note though that it achieves less than a factor of 2 improvement compared to the broad-band case (mode 1b).

Mode	*NS-NS Range*	*BH-BH Range*	P_{in}	T_{SRM}	ϕ_{SRC}
0	137 Mpc	1.17 Gpc	25 W	100%	–
1a	148 Mpc	1.49 Gpc	25 W	20%	0 deg.
1b	175 Mpc	1.23 Gpc	125 W	20%	0 deg.
2	179 Mpc	1.03 Gpc	125 W	20%	11 deg.
3	168 Mpc	1.61 Gpc	20 W	20%	20 deg.
4	158 Mpc	1.96 Gpc	4.5 W	20%	72 deg.
5	122 Mpc	1.38 Gpc	125 W	1.1%	4.7 deg.

Table 1: Parameters for the operational modes described above, and shown in Fig. 1. The homodyne detection phase is also optimized in each case, which in practice can be set via the Michelson dark fringe offset.

1.4 Interferometer Diagram

Refer to Fig. 2 for a block diagram of the interferometer, showing the ISC detection ports and the length degrees-of-freedom.

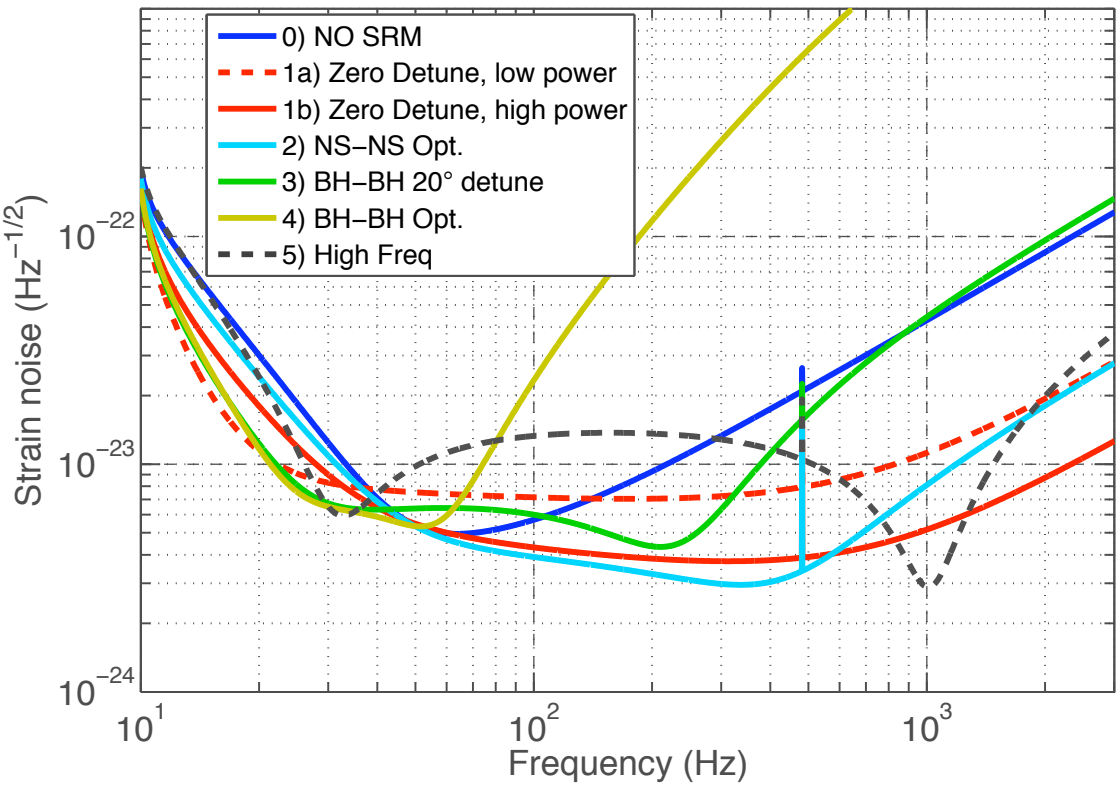

Figure 1: Proposed modes of operation for the Advanced LIGO interferometers. See text for description of the modes.

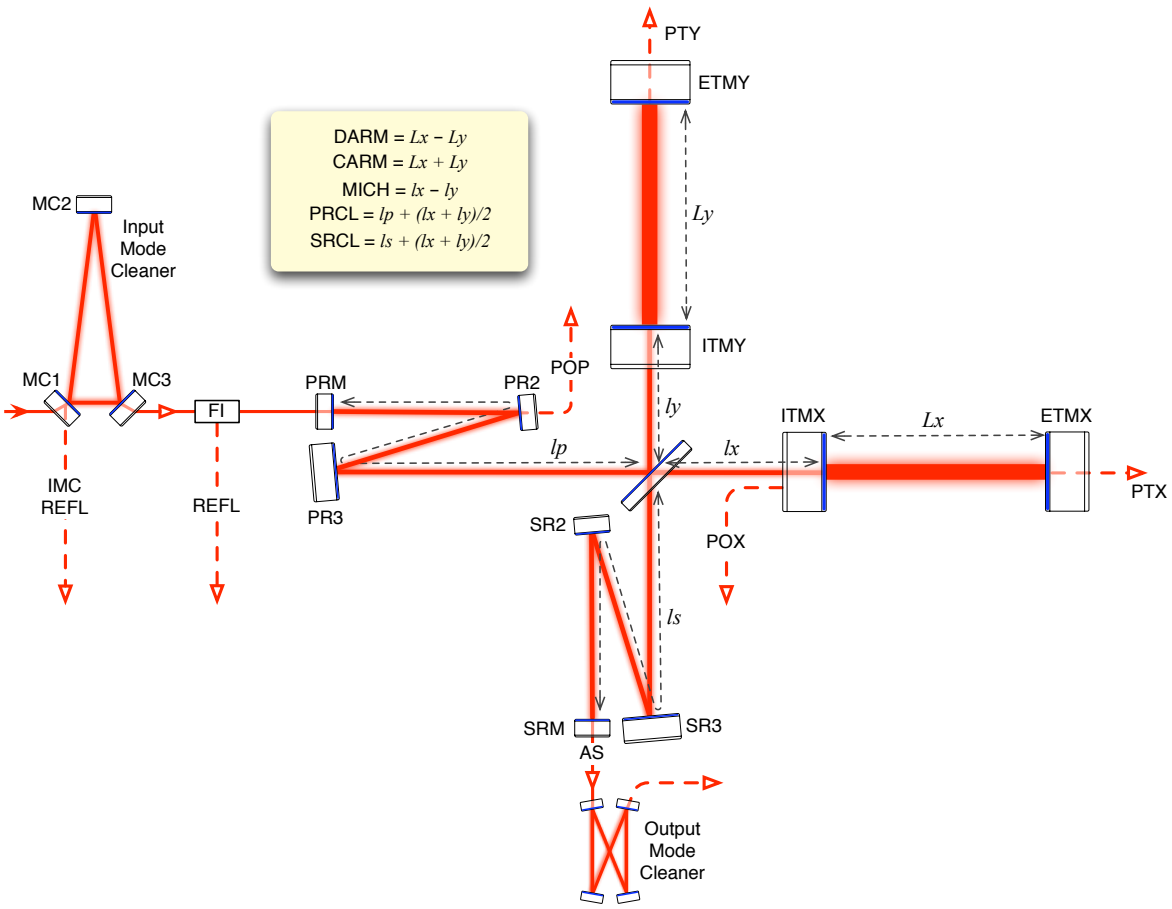

Figure 2: Interferometer diagram, showing ISC detection ports and length degrees-of-freedom. Port acronyms: REFL, reflection port; POP, power recycling cavity pick-off; POX, X arm pick-off; AS, anti-symmetric port; PTX/Y, transmitted power X/Y arm.

Quantity	*Non-Folded IFOs*	*Folded IFO*
Finesse	446	446
ITM transmission	0.014	0.014
PRM transmission	0.030	0.030
SRM transmission	0.200	0.200
Schnupp asymmetry	0.050	0.050
l_{PRC}	57.676 m	60.398 m
l_{SRC}	56.028 m	62.124 m
l_{IMC} (round trip)	32.957 m	34.513 m
l_{EX}	3994.75 m	3996.00 m
l_{EY}	3994.75 m	3996.00 m
Lower mod. frequency	9'096'270 Hz	8'686'280 Hz
Upper mod. frequency	45'481'350 Hz	43'431'400 Hz

Table 2: Basic interferometer parameters for both folded and non-folded case.

2 Modulation and Readout

2.1 Modulation

The laser light is phase modulated at two radio frequencies, $f_1 \approx 9$ MHz and $f_2 = 5f_1 \approx 45$ MHz. The two frequencies are phase-locked to avoid any beat from higher-order sidebands. We intend to use serial modulation in one crystal, i.e. we do not need a Mach-Zehnder interferometer (see appendix B). However a Mach-Zehnder could be retrofitted.

Additionally we want to avoid hitting arm resonances with a sideband, at least for the lowest order spatial arm modes. With test mass radii of curvature of 2191 m for the ETMs and 1971 m for the ITMs and an arm cavity free spectral range of 37.52 kHz the transverse mode spacing is 32.69 kHz. Table 3 shows the minimal separations from arm cavity resonances for all sidebands. It uses sideband frequencies of $f1 = 9.096270$ MHz and $f2 = 45.481350$ MHz for the non-folded interferometer, and $f1 = 8.686280$ MHz and $f2 = 43.431400$ MHz for the folded interferometer. No higher order mode comes closer to resonance than about 1.1 kHz, and all modes closer than 2 kHz (roughly the upper end of the GW band of interest) are highlighted in red. Note that in initial LIGO audio sidebands of RF sidebands becoming resonant in the arms were responsible for a significant increase in the phase noise coupling [1].

2.2 Optics properties and layout

2.2.1 Finesse and PRM transmission

We aim at an arm finesse of about 450, requiring an ITM transmission of $T_{ITM} = 0.014$. The finesse was lowered to this for a variety of reason, see "Arm Cavity Finesse for Advanced LIGO", LIGO-T070303. Assuming a loss of 37.5ppm per mirror (reference?) implies critical coupling at a Power Recycling mirror transmission of $T_{PRM}^{\text{crit}} = 0.023$. With $T_{PRM} = 0.03$ we aim for slight over-coupling (2% of carrier power reflected for nominal scattering loss, Figure 3). This both provides some robustness against the uncertainty in scatter loss, and -

Sideband offset from arm resonance			
Upper low frequency sideband (f1=9.0963 MHz)			
# FSR offset	l+m	offset from resonance	offset from anti-resonance
242	0	15.63 kHz	3.132 kHz
242	1	17.07 kHz	
241	1		**1.697** kHz
241	2	12.24 kHz	
240	2		6.525 kHz
240	3	7.408 kHz	
239	4	2.58 kHz	
238	5	2.249 kHz	
237	6	7.077 kHz	
Lower low frequency sideband (f1=9.0963 MHz)			
# FSR offset	l+m	offset from resonance	offset from anti-resonance
−242	0	15.63 kHz	
−243	0		3.132 kHz
−243	1	10.8 kHz	
−244	2	5.973 kHz	
−245	3	**1.144** kHz	
−246	4	3.684 kHz	
−247	5	8.512 kHz	
−248	6	13.34 kHz	5.421 kHz
Upper high frequency sideband (f2=45.4813 MHz)			
# FSR offset	l+m	offset from resonance	offset from anti-resonance
1212	0	3.102 kHz	
1211	1	7.931 kHz	
1210	2	12.76 kHz	6.002 kHz
1209	3	17.59 kHz	**1.174** kHz
1209	4	15.11 kHz	
1208	4		3.655 kHz
1208	5	10.28 kHz	
1207	6	5.45 kHz	
Lower high frequency sideband (f2=45.4813 MHz)			
# FSR offset	l+m	offset from resonance	offset from anti-resonance
−1212	0	3.102 kHz	
−1213	1	**1.726** kHz	
−1214	2	6.555 kHz	
−1215	3	11.38 kHz	
−1216	4	16.21 kHz	2.550 kHz
−1216	5	16.48 kHz	
−1217	5		2.278 kHz
−1217	6	11.65 kHz	
−1218	7	6.826 kHz	

Table 3: Table showing the closest sideband resonances in the arm cavities up to spatial modes with $l + m = 6$. Separation from exact anti-resonance is shown in column 4 if it is closer than 7 kHz. All offsets less than 2 kHz are highlighted in red. The table is for the non-folded interferometers.

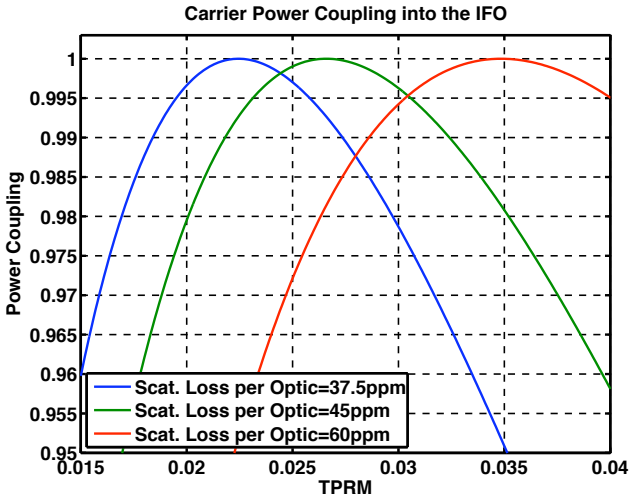

Figure 3: Carrier Power Coupling vs. T_{PRM} for a scatter loss of 37.5ppm, 45ppm and 60ppm per optic.

assuming we correctly estimated the scatter loss - provides alternative and potentially better error signals for MICH and SRCL at the REFL port.

2.2.2 SRM transmission

The Signal Recycling mirror transmission can be chosen to optimize the bottom-line sensitivity. The test mass thermal noise is limiting over a broad frequency band. Thus we don't get any benefit from a narrow-band SRC, but are instead pushed to a low SRC finesse, meaning a high T_{SRM}. For NS/NS inspirals this results in $T_{SRM} = 0.16$ for the detuned case (Science mode 2), and in $T_{SRM} = 0.26$ for zero detuning (Science mode 1). However, as long as we are in the low finesse regime, it is not a very critical parameter. The sensitivity only depends weakly on T_{SRM}. We thus chose a round $T_{SRM} = 0.2$, which allows to come within about 1% of the optima for each science mode. All the Signal Recycling mirror transmission tuning was done in *bench62.m*.

2.2.3 Schnupp Asymmetry

The Schnupp Asymmetry was chosen to get close to critical coupling for the f_2 sideband in the dual recycling cavity. This condition maximizes the f_2 sideband power in the signal recycling cavity. Note that, given T_{PRM} and T_{SRM}, there are two solutions for critical coupling the dual recycling cavity:

1. Small Schnupp Asymmetry, $l_{asy} \approx 4$ cm, $T_{asy} \approx 1.5e-3$: This requires that both Power and Signal Recycling Cavity are resonant for f_2.

2. Large Schnupp Asymmetry, $l_{asy} \approx 0.68$ m, $T_{asy} \approx 0.39$ This requires that exactly one of the two recycling cavities is resonant for f_2. The other one has to be anti-resonant.

Both solutions result in the same f_2 sideband power inside the Signal Recycling Cavity, but they generally result different sensing matrices.

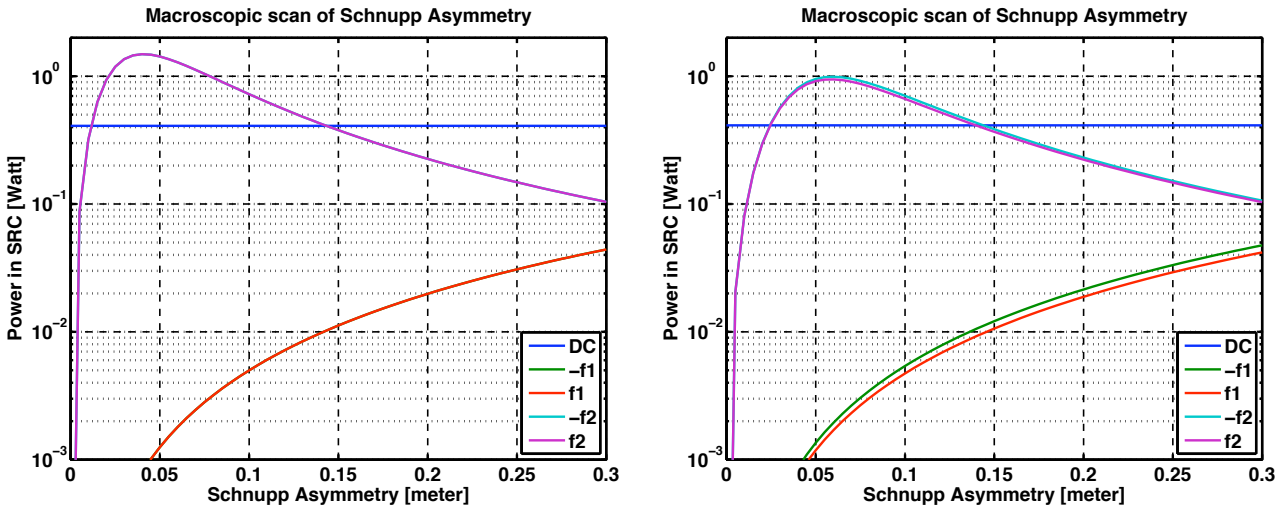

Figure 4: Power in Signal Recycling Cavity vs. Schnupp Asymmetry $l_{asy} = l_x - l_y$. The left plot is for zero SRM detuning (Science Mode 1), the right one is for the 11 deg detuning required for NS/NS tuning (Science Mode 2). Both recycling cavities are resonant for f_2, so the plot only shows the small Schnupp Asymmetry solution.

We chose the small Schnupp asymmetry (l_{asy}) because it allows a f1 to f2 sideband power ratio of 10^{-3} in the SRC, while the large l_{asy} only allows for about 10^{-1}. Thus the small l_{asy} provides a cleaner PRC / SRC separation in the error signals. Figure 4 also shows that the optimal Schnupp asymmetry changes from 4 cm to about 6 cm if we go to 11 deg SRM detuning.

Setting the Schnupp asymmetry to 5 cm is a good compromise between the two cases.

2.2.4 Power and Signal Recycling Cavity length

The Power Recycling Cavity has to be resonant for the f_1 and f_2 sideband when the arms are locked, i.e

$$l_{PRC} = (N + \frac{1}{2})\frac{c}{2f_1} \tag{2.1}$$

For a stable recycling cavity $l_{PRC} = 57.676$ meters, $(N = 3)$ and $l_{PRC} = 60.398$ meters, $(N = 3)$ are consistent with the preliminary opto-mechanical layout for the non-folded and folded interferometers.

The signal recycling has to be close to resonant for the f_2 sideband, while the f1 sideband is non-resonant.

$$l_{SRC} = M\frac{c}{2f_2}, \text{ but not } Q\frac{c}{2f_1} \tag{2.2}$$

M and Q integers. Figure 5 shows a macroscopic scan of the signal recycling cavity. For the non-folded IFOs we suggest $l_{SRC} = 56.028$ $(M = 17)$, while the folded IFO the opto-

mechanical constraints suggest $l_{SRC} = 62.124$ ($M = 18$). Equation 2.2 should be met within about 1 cm. This is because the relative demod angle of SRCL and MICH in the REFL double demod signal is exactly 90 deg and changes at a rate of about 9 deg per centimeter of offset from the resonance condition.

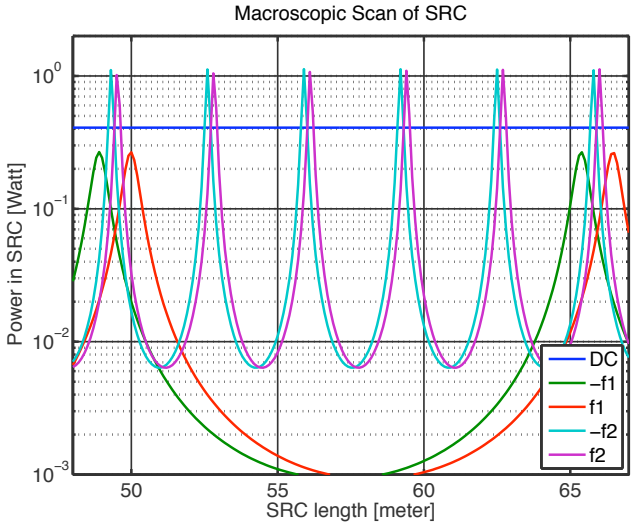

Figure 5: Power in Signal Recycling Cavity vs. Signal Recycling Cavity length for the non-folded interferometer and a detuned SRM (Science mode 2).

2.2.5 DC readout and DARM fringe offset

Loss difference in the arms and any asymmetry in the BS results in some light on the AS_DC photo diode even when the DARM offset is zero. Assuming a differential arm round trip loss of 30 ppm this light is on the order of $P_0 = 1$ mWatt (4 mWatt for 60 ppm, see figure 6).

The AS_DC light due to DARM offset is quadratic in DARM offset and reaches $P_{\mathrm{DARM}} =$ 100 mWatt at a DARM offset of about 12 pm (figure 6). 100 mWatt is also what we think our DC photo diode should be able to handle.

The homodyne phase is defined as the arctan (P_{DARM}/P_0). Theoretically the NS/NS range peaks at a homodyne phase somewhere around 100 deg, but the sensitivity gain compared to a homodyne phase of 90 deg is minimal. Also technical noise couplings such as Intensity noise become bigger for small DARM offsets, thus driving us to larger offsets (i.e. closer to 90 deg homodyne phase). Thus we most likely will operate at a DARM offset of about 10 pm.

2.3 Error signals

In addition to AS DC, length error signals are derived from demodulating the REFL and POX beam at f_1, f_2, $f_2 + f_1$ and $f_2 - f_1$. For primary feedback we will use REFL I1 for CARM (high bandwidth analog loop), AS DC for DARM, and POP I1 for PRCL, POP Q2 for MICH and REFL IM/IP for SRCL. Alternatively REFL I2 or POB I2 can be used for

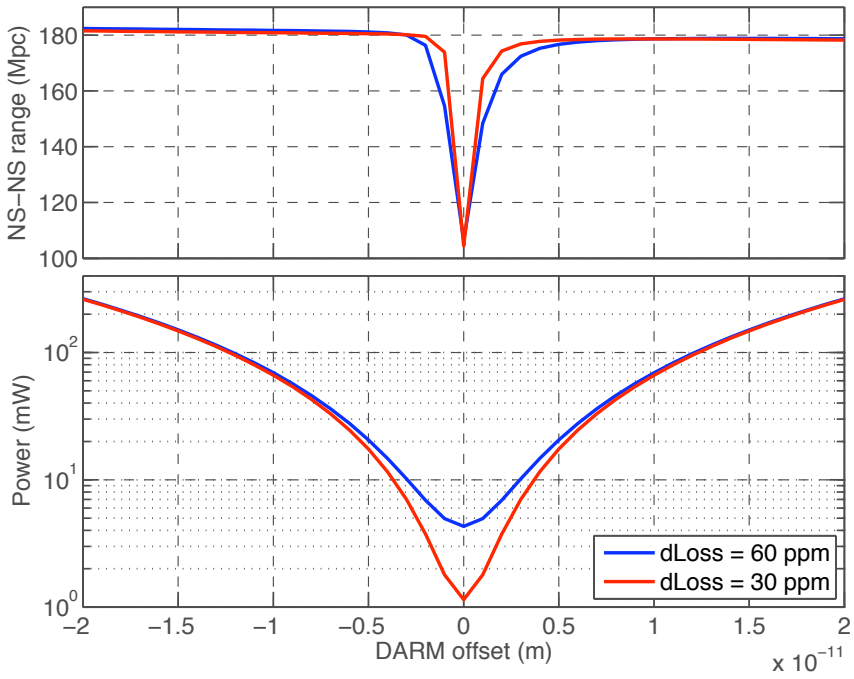

Figure 6: Sensitivity and AS DC power as a function of DARM offset. Here the sensitivity only includes contribution from Quatum noise and mirror thermal noise.

SRCL - these signals have the advantage that they also work at zero detuning. The sensing matrix for these ports is given in section 3.1.

In appendix A, Table 20 shows the the full sensing matrix for the detuned case, while Table 21 shows the Non-detuned case. The dominant matrix elements are highlighted in red.

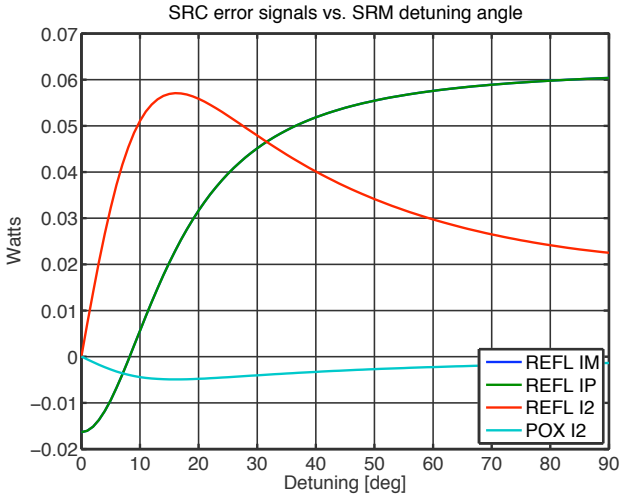

Figure 7: SRC error signals vs SRM detuning angle. Switching between REFL IM/IP and REFL I2/POX I2 at a detuning angle of about 5 deg allows for continuous detuning to any desired phase. POB looks identical to POX.

Figure 7 shows how the different SRCL error signals depend on the signal recycling detuning. After CARM and DARM are locked, the transfer functions from SRCL to both REFL I2 and POP I2 are basically flat and only vary in overall gain according to the (derivative) of Figure 7.

2.4 Optical power at sensing ports

The table below shows the power at each optical port in mWatt for science mode 2 (NS/NS case). REFL, POP and OMC were attenuated to 100 mWatt (REFL: 4%, POP: 39%, OMC: 61% transmission). The table doesn't change significantly for science mode 1.

Optical Port Power in mWatt

FREQ (MHz)	-56.4	-47.0	-37.6	-30.1	-9.4	0.0	9.4	30.1	37.6	47.0	56.4	Total
REFL	0.0	9.4	0.0	0.0	10.0	62.7	10.0	0.0	0.0	7.6	0.0	99.9
AS	0.0	0.0	0.0	0.0	0.0	81.6	0.0	0.0	0.0	0.0	0.0	81.6
POP	0.0	0.1	0.0	0.0	0.7	98.2	0.7	0.0	0.0	0.3	0.0	100.0
OMC	0.0	38.9	0.0	0.0	0.1	0.0	0.1	0.0	0.0	60.8	0.0	100.0
IMC	0.0	0.1	0.0	28.9	0.1	22.1	0.1	28.9	0.0	0.1	0.0	80.3

2.5 (Electrical) RF power at sensing ports

Finally, the two tables below show the RF signal level at the relevant frequencies for the REFL and POP port. The signals are still in mWatt - multiply with the photodiode gain of $\epsilon \cdot 0.86$ Ampere/Watt to get Amperes. ϵ is the quantum efficiency. The reported values include both quadratures.

RF power at ports in mWatt for zero-detuned operation (science mode 1)

FREQ (MHz)	0.0	9.1	18.2	36.4	45.5	54.6	91.0
REFL	90.14	0.08	20.19	21.58	0.04	19.37	7.05
POP2	99.89	0.00	1.43	1.13	0.00	1.13	0.22

RF power at ports in mWatt for detuned operation (science mode 2)

FREQ (MHz)	0.0	9.1	18.2	36.4	45.5	54.6	91.0
REFL	99.95	0.09	20.19	34.43	26.06	31.99	16.85
POP	100.01	0.00	1.43	1.41	4.14	1.41	0.33

3 Science mode length and frequency controls

The sensing matrix and noise at each port were calculated using the AdvLIGO Optickle and Looptickle model (see appendix C).

The following table summarizes the main features of the control loops:

Loop	*Error signal*	*UGF*	*Phase margin*
CARM	REFL_I1	65 kHz	68 deg
DARM	AS_DC	446 Hz	26 deg
PRCL	POP_I1	21 Hz	32 deg
MICH	POP_Q2	20 Hz	34 deg
SRCL	REFL_IM / REFL_IP	15 Hz	37 deg
IMCL	IMC_I3	377 kHz	68 deg

The table is for the NS/NS case. In the zero detuning case the SRCL loop uses POP_I2 or REFL_I2 as error signal.

The SRCL→DARM and MICH→DARM correction paths were implemented as described in paragraph 3.5 with an accuracy of about 1%. Additionally a very rough PRCL→DARM correction path was also implemented about 10% precision.

3.1 Sensing matrix

The following sensing matrices for Science mode 1 and 2 were calculated in Optickle:

Sensing Matrix in Watts per meter at 1 kHz, for Science Mode 2 (NS/NS inspiral)

Port	CARM	DARM	PRCL	MICH	SRCL
REFL I1	**9.4e+08**	2e+05	7.3e+07	1.1e+06	**5.5e+03**
AS DC	1.3e+06	**4.2e+09**	2.8e+05	1.5e+07	7.6e+06
POP I1	3.2e+07	6.7e+03	**1.2e+07**	**6.8e+03**	**3.1e+02**
POP Q2	1.5e+07	2.3e+04	**1.4e+06**	**4.3e+05**	**3e+04**
REFL IM	1.4e+06	**2.5e+04**	**5.1e+06**	**4.5e+05**	**2.8e+05**

Sensing Matrix in Watts per meter at 1 kHz, for Science Mode 1 (zero detuning)

Port	CARM	DARM	PRCL	MICH	SRCL
REFL I1	**9.4e+08**	1.3e+05	7.3e+07	1e+06	**1.4e+04**
AS DC	3e+06	**9.7e+09**	6.7e+05	3.4e+07	7e+03
POP I1	3.2e+07	4.4e+03	**1.2e+07**	**6.6e+03**	**3e+02**
POP Q2	8.7e+06	4.2e+04	**4.6e+05**	**7.4e+05**	**8.8e+04**
POP I2	8.7e+06	9e+03	**1.8e+06**	**9.9e+04**	**3e+05**

The contractions used in the port name are: I: I-phase, Q: Q-phase, 1: demodulated at f_1, 2: demodulated at f_2, M: demodulated at $f_2 - f_1$, P: demodulated at $f_2 + f_1$. The main matrix elements are in bold red. The biggest worrisome elements are in blue. The full sensing matrix with all available ports is shown in Figures 20 and 21 of appendix A.

3.2 Sensing noise

The shot noise for 100 mWatt on the detection diodes the shot noise is about $2e{-}10$ Watt/$\sqrt{\text{Hz}}$; it varies slightly between the ports because the non-stationary shot noise contribution depends on the amount of sideband. The following table summarizes the optical gain and approx. sensing noise at 100Hz. It is calculated for science mode 2 (NS/NS), but the numbers for zero-detuning are very similar. (See also sections 3.3 and 3.4 for detailed noise

budgets.)

Loop	*Port*	*optical gain at 100 Hz*	*sensing noise at 100 Hz*
CARM	REFL_I1	$8.5e+10$ m/Watt	$2.4e-21$ m/$\sqrt{\text{Hz}}$ (*)
DARM	AS_DC	$2.1e+10$ m/Watt	$9.5e-21$ m/$\sqrt{\text{Hz}}$
PRCL	POP_I1	$1.2e+7$ m/Watt	$1.7e-17$ m/$\sqrt{\text{Hz}}$
MICH	POP_Q2	$4.4e+5$ m/Watt	$4.5e-16$ m/$\sqrt{\text{Hz}}$
SRCL	REFL_IM	$2.9e+5$ m/Watt	$6.9e-16$ m/$\sqrt{\text{Hz}}$

(*): Because MC2 is the actuation point of the CARM loop, it's number is in meters of MC2 motion. Multiply by l_{arm}/l_{MC} for meters of CARM.

3.3 DARM noise budget

The various noise budgets below contain the following noise sources:

- **Quantum** or **Shot Noise** from the loop itself, calculated by injecting vacuum noise at every open optical port.
- **Shot Noise** from the other loops, calculated by propagating the quantum noise in the other loops through the control system.
- **Seismic Noise**, using the expected performance of the ISI and Quad suspension. Currently only the seismic noise of the 4 test mass suspensions is included.
- **Thermal Noise**, including Mirror Thermal and Suspension Thermal noise.
- **Frequency Noise** incident on the input mode cleaner (i.e. input mode cleaner and common mode sensing noise are counted as shot noise from those length loops). The used numbers are 1 Hz/rtHz at and below 20Hz, $2e-2$ Hz/rtHz at and above 1000Hz.
- **Intensity Noise** incident on the IMC. The used numbers are $2e-9$ 1/rtHz at and below 10Hz, $1e-7$ Hz/rtHz at and above 500Hz.
- **Oscillator Phase Noise**, using the specification of a Wenzel Crystal Oscillator ($1e-5$ rad/rtHz at and below 10Hz, $3e-7$ rad/rtHz at 100Hz, $2e-8$ rad/rtHz at and above 1000Hz). The coupling does include the light passing through the IMC. Currently the estimate does not include potential noise added after the EOM/LO split.
- **Oscillator Amplitude Noise**, using the specification of a Wenzel Crystal Oscillator ($1e-7$ rad/rtHz at and below 10Hz, $1e-8$ rad/rtHz at 100Hz, $3e-9$ rad/rtHz at and above 1000Hz).
- **Facility** includes Gravity Gradient noise and residual gas noise.

Arguably the most important noise source that is still missing in these budgets is the cross-coupling from angular control loops. See section 4 for more details.

The DARM noise budget for the NS/NS case is shown in figure 8, the zero-detuning case is shown in figure 9.

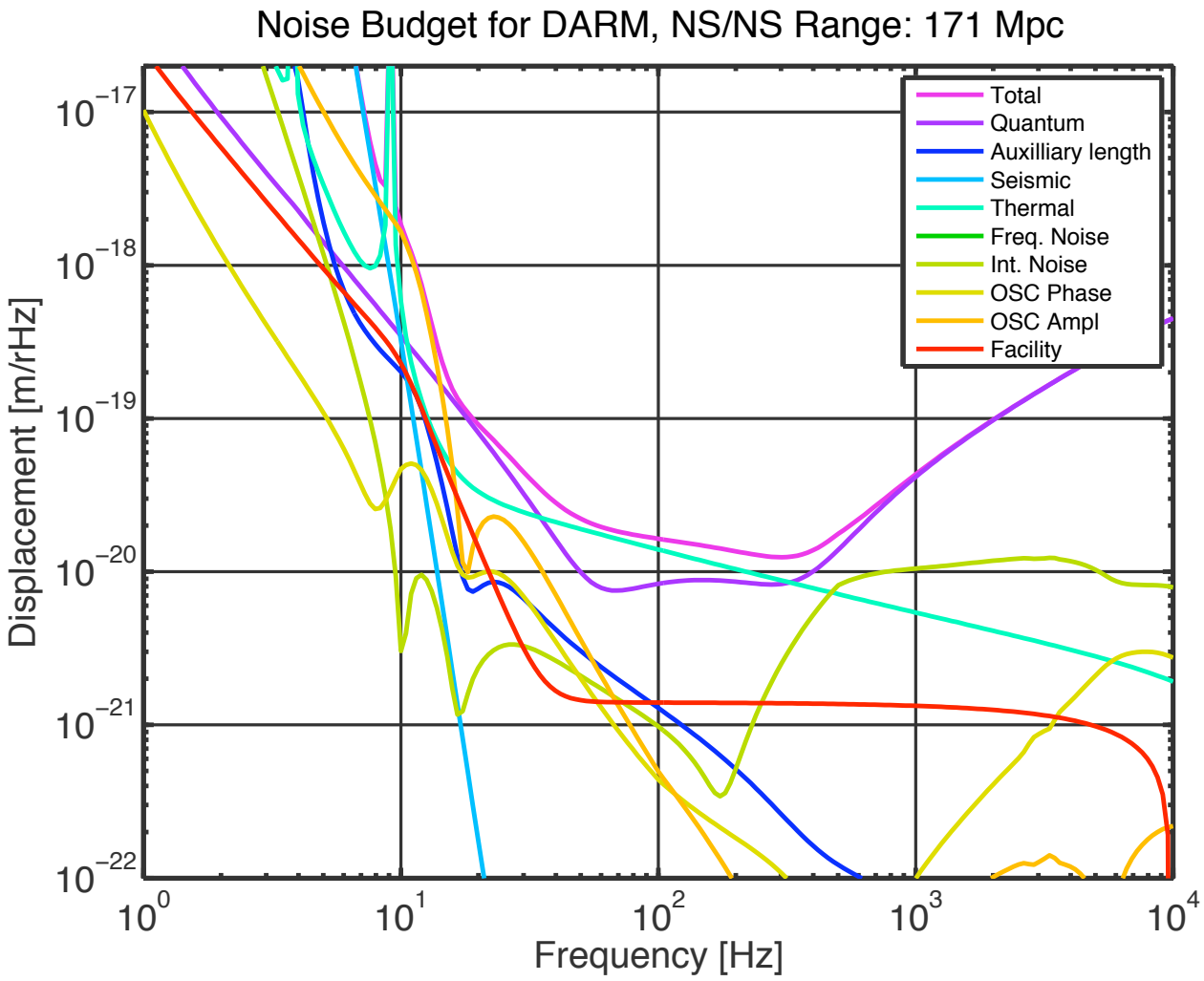

Figure 8: DARM noise budget for the NS/NS case.

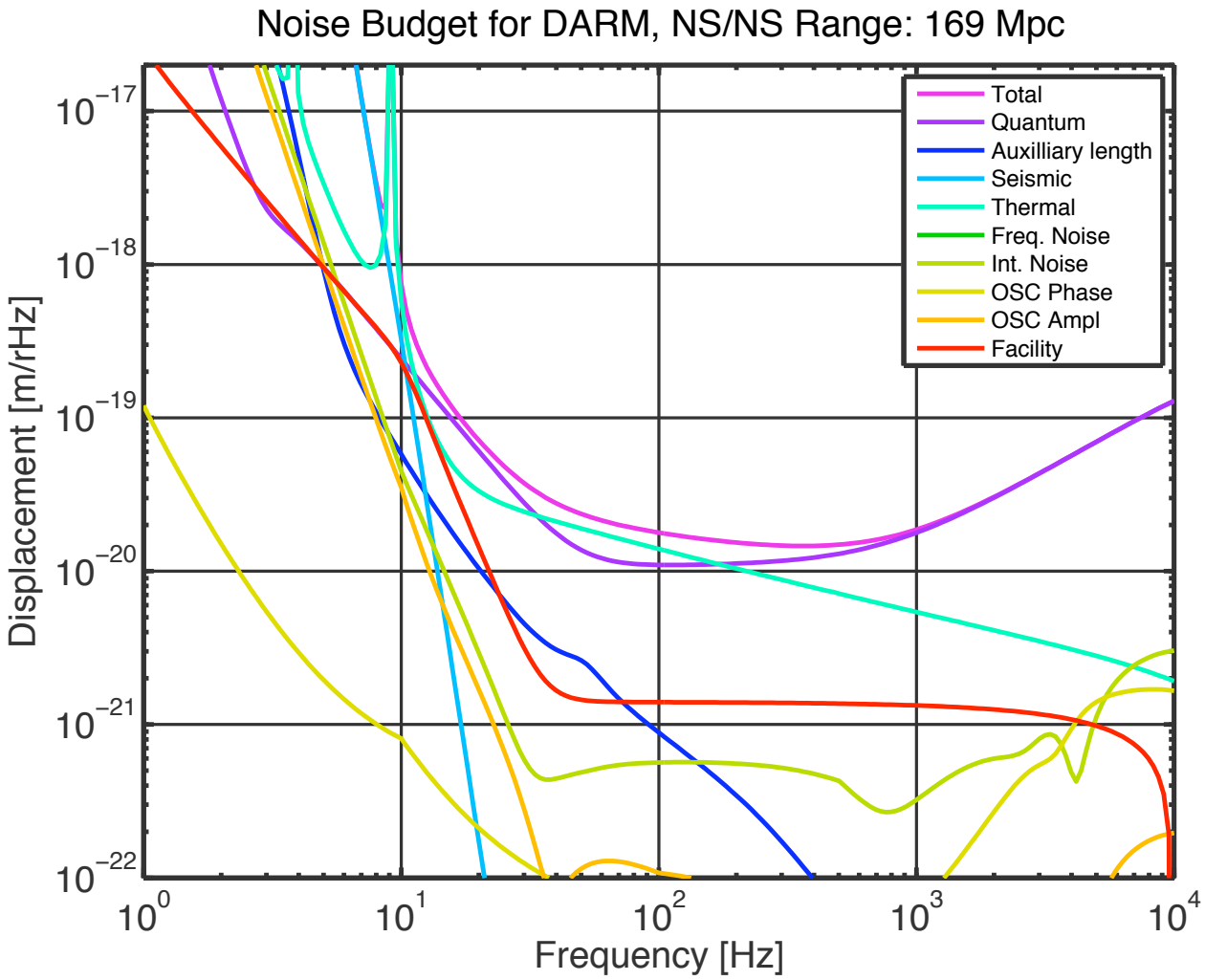

Figure 9: DARM noise budget for the zero detuning case.

3.4 Auxiliary loops noise budget

The figures 10 to 14 show noise budgets for all auxiliary loops. For SRCL and MICH both the NS/NS and zero-detuning cases are shown (figures 10,11,14, and 15).

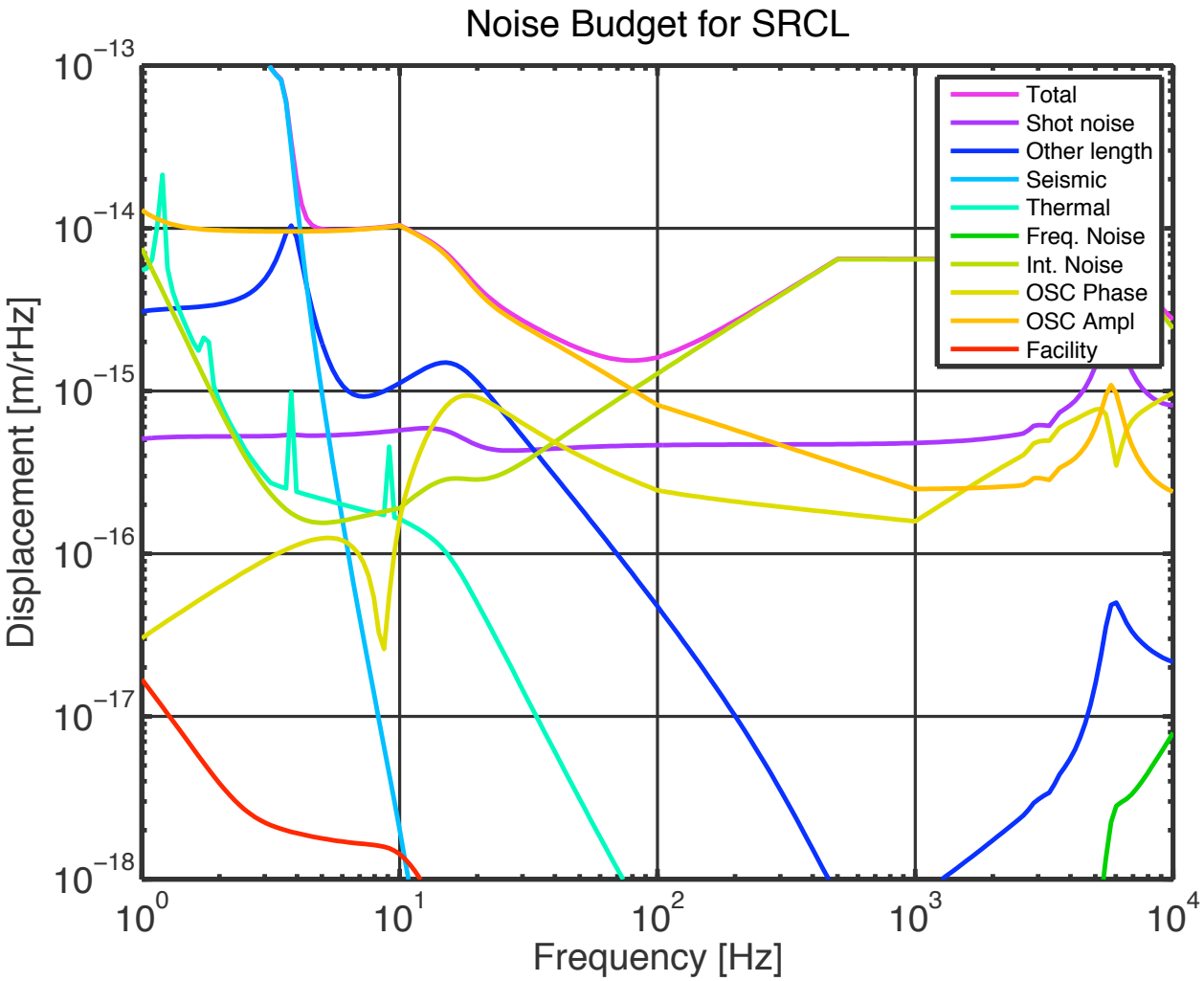

Figure 10: SRCL noise budget for the NS/NS case.

3.5 Required correction paths

The in-band noise of all auxiliary loops is sensing-noise limited, i.e the control system adds displacement noise to the auxiliary optics at the frequencies we care. This extra noise then couples to DARM through known mechanisms.

But since this coupling is known it is possible to cancel the noise by also sending a filtered copy of the auxiliary loop control signals to the ETMs, see figure 16.

The dominant coupling mechanisms are:

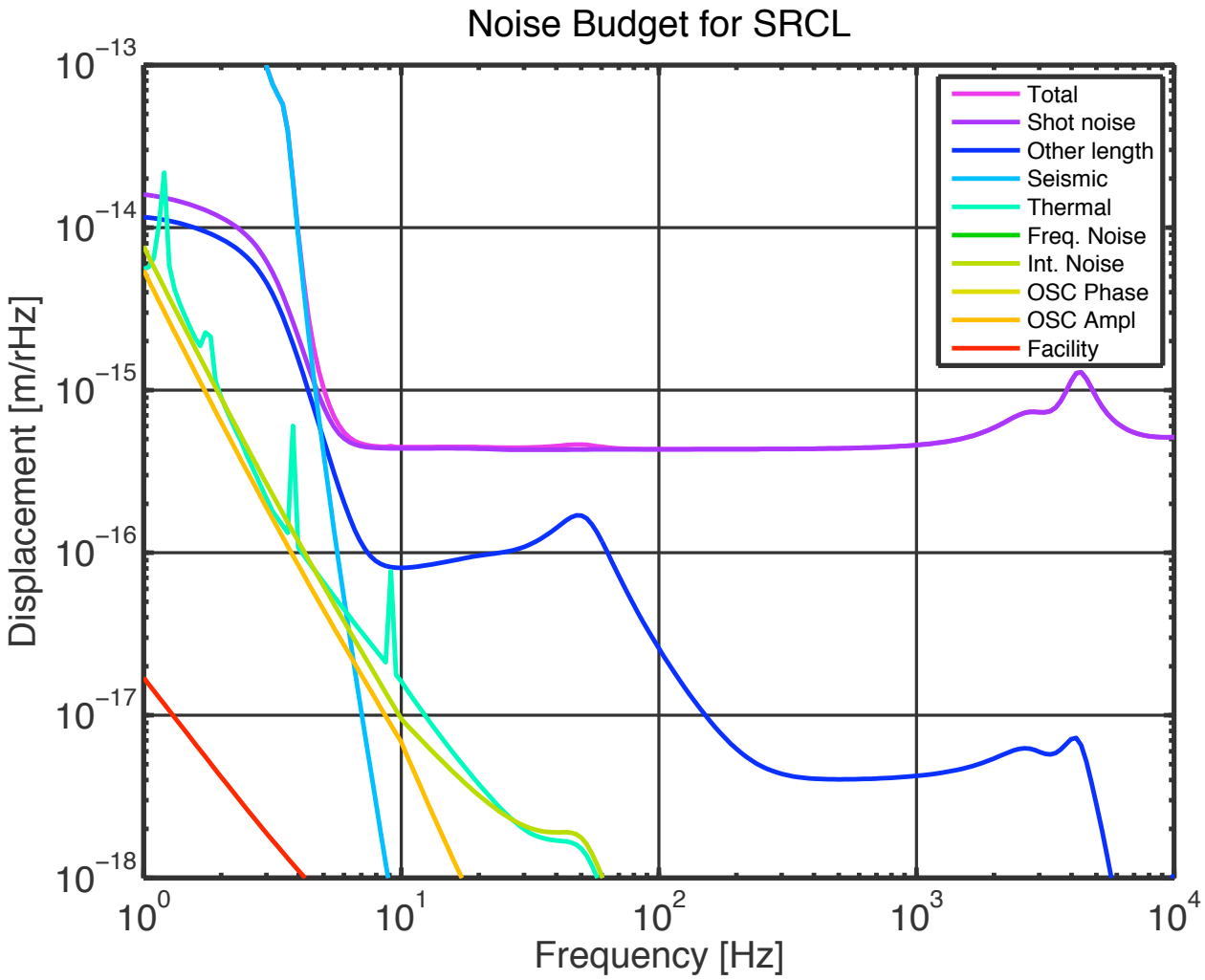

Figure 11: SRCL noise budget for the zero detuning case.

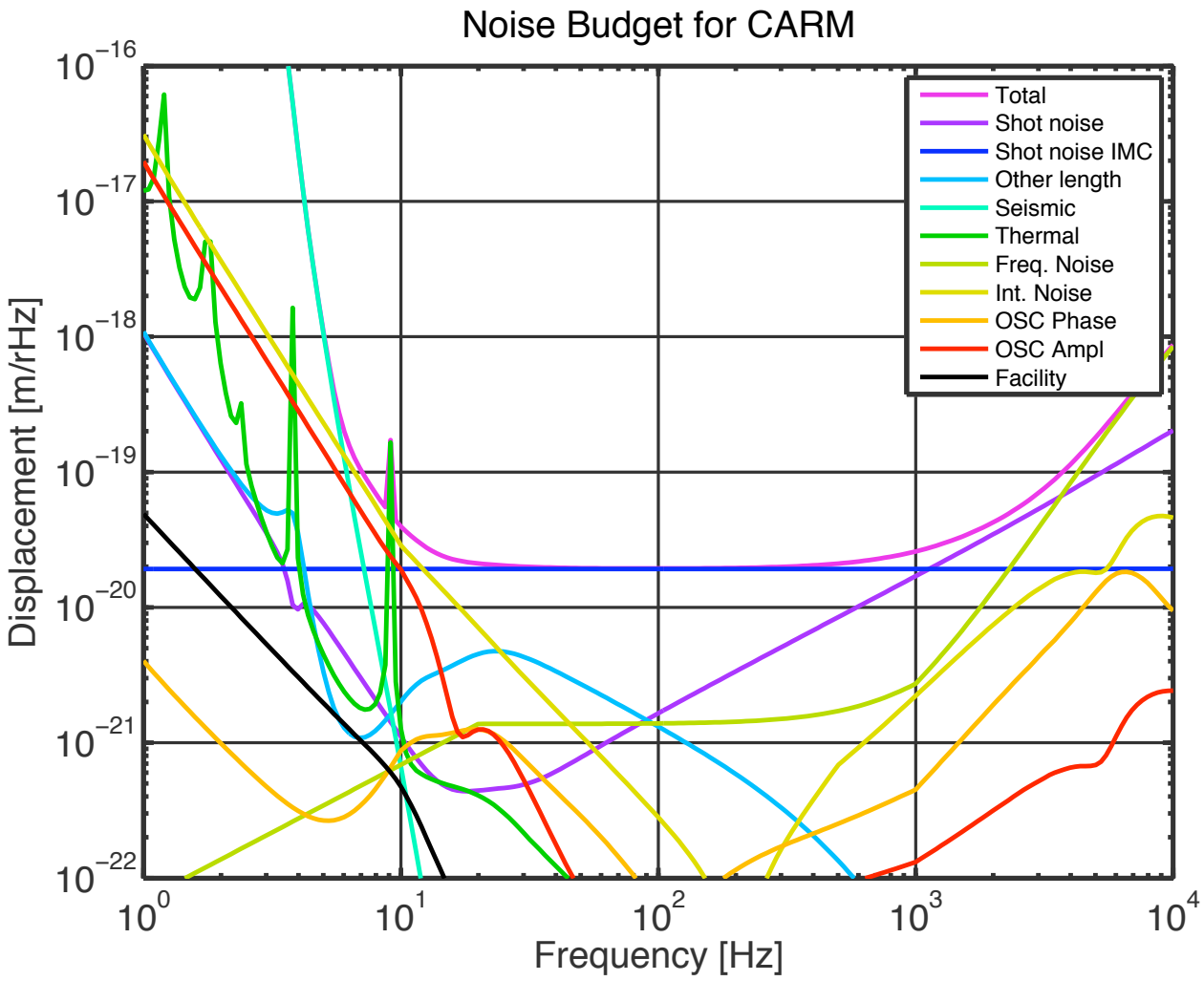

Figure 12: CARM noise budget for the NS/NS case.

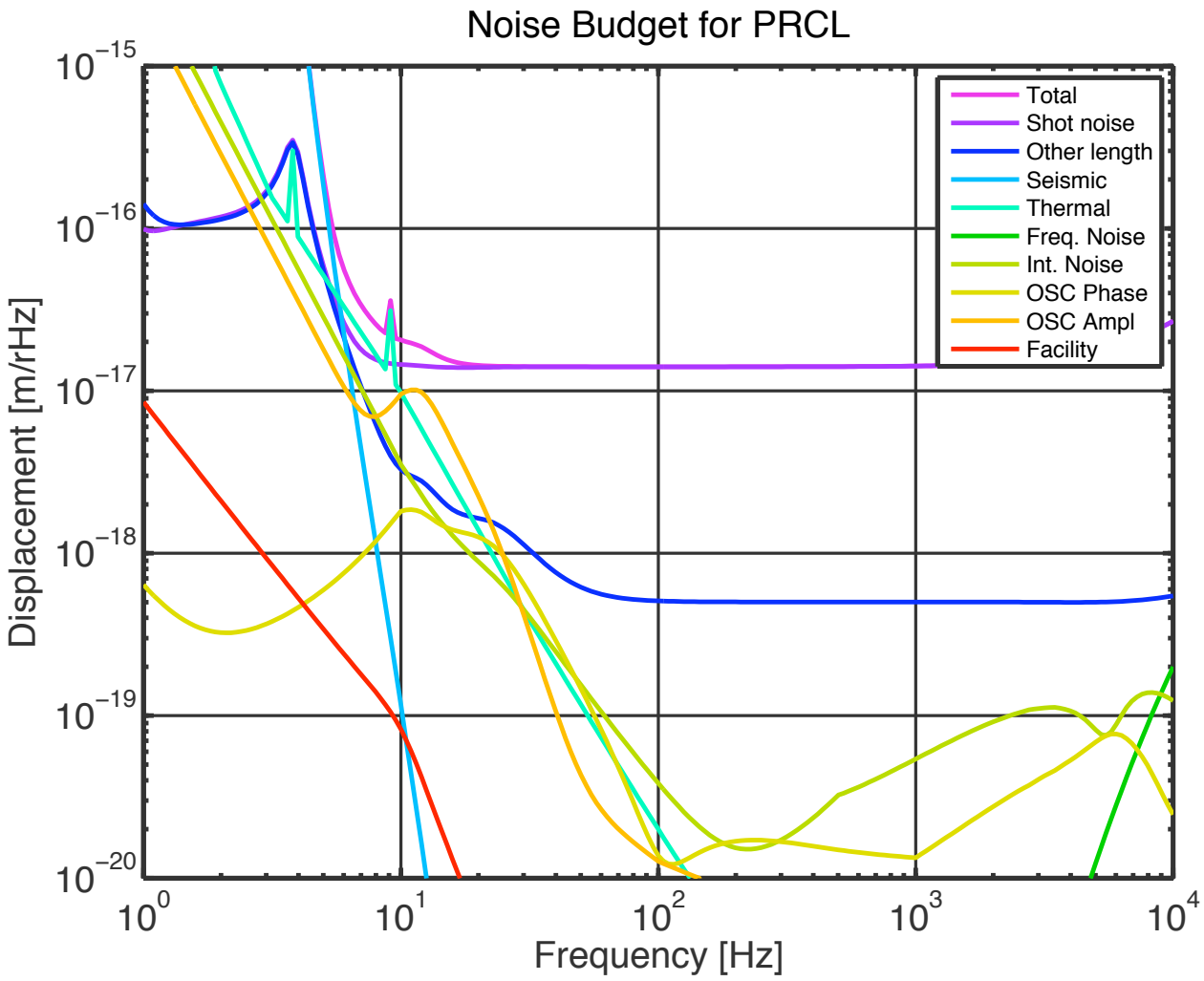

Figure 13: PRCL noise budget for the NS/NS case.

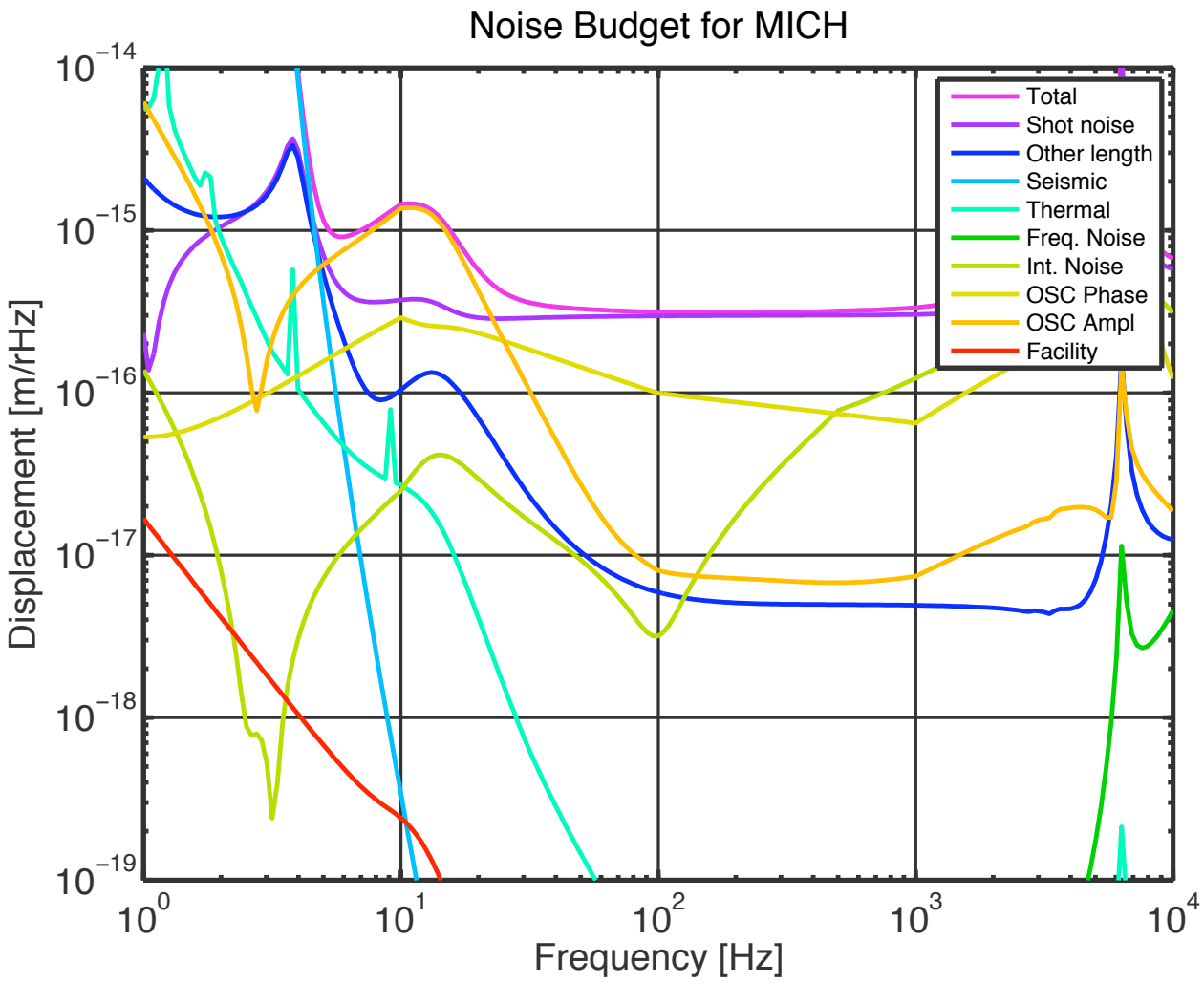

Figure 14: MICH noise budget for the NS/NS case.

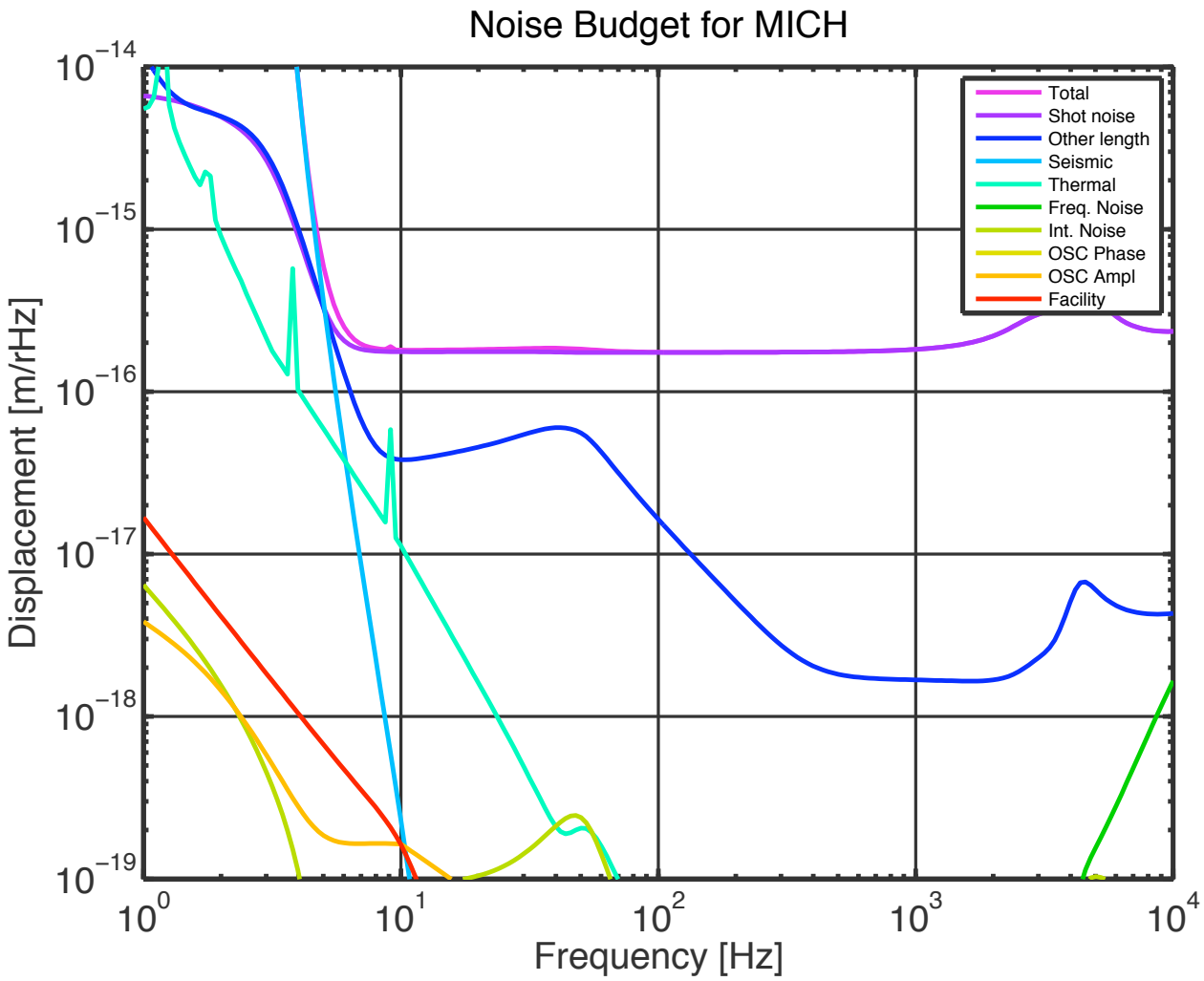

Figure 15: MICH noise budget for the zero detuning case.

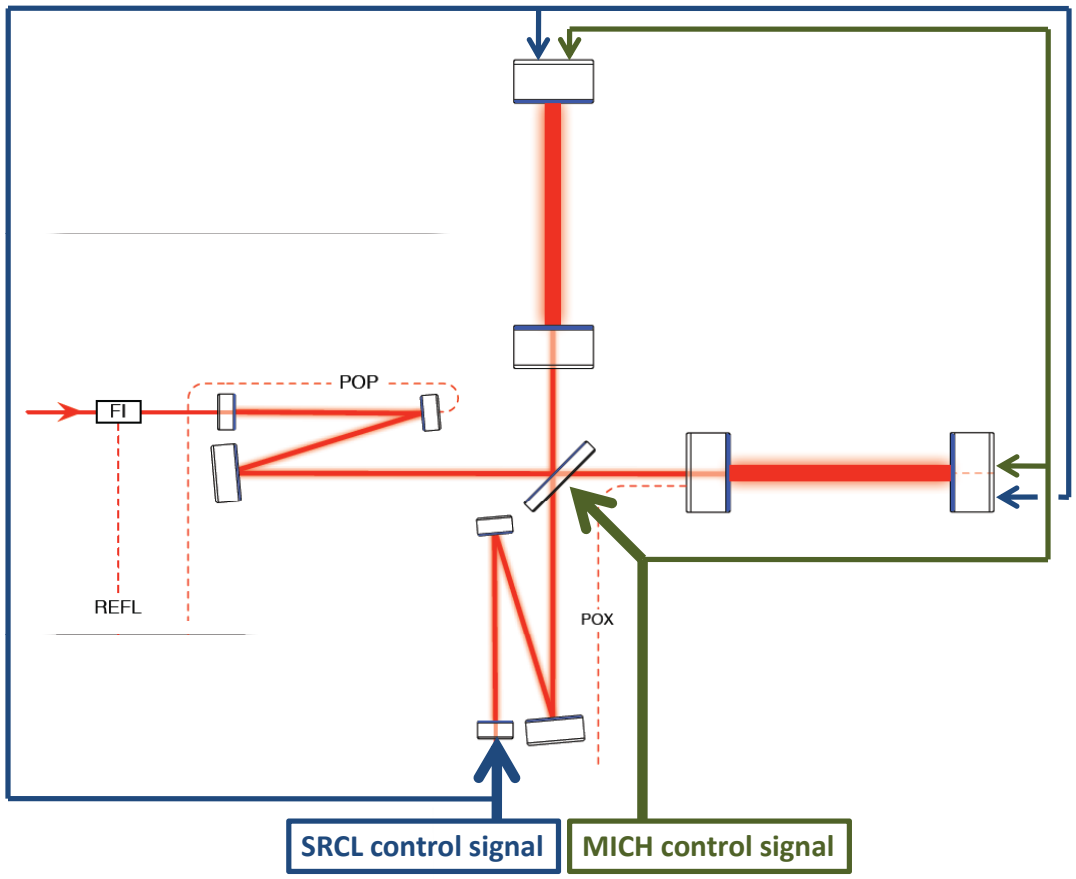

Figure 16: MICH and SRCL correction paths. A filtered copy of the sensing noise limited MICH and SRCL control signals is sent to the ETMs to cancel known couplings.

Loop	*Port*	*Fringe offset*
DARM	AS_DC	$1.5e-15$ m rms
PRCL	POP_I1	$4.5e-12$ m rms
MICH	POP_Q2	$1.8e-11$ m rms
SRCL	REFL_IM	$3.1e-12$ m rms

Table 4: RMS fringe offset for the main control loops. All loops are dominated by the micro-seism. No resonant gain filters have been applied so far.

- MICH coupling: It's coupling in DARM meters per MICH meters is given by

$$K_{\mathrm{MICH}} = \frac{\pi}{2F}, \tag{3.1}$$

  where F is the arm finesse. One MICH correction path with a precision of about 1% is needed.

- SRCL coupling: The SRCL to DARM coupling is not only the dominant coupling path for SRCL sensing noise, but also for other noise sources, such as PRCL sensing noise, intensity noise and oscillator phase noise. It's shape consists of two parts. At low frequency the coupling is dominated by radiation pressure and can be parametrized as

$$K^{(1)}_{\mathrm{SRCL}} = 0.012 \left(\frac{10\ \mathrm{Hz}}{f}\right)^2 \left(\frac{P_{\mathrm{arm}}}{750\ \mathrm{kW}}\right) \left(\frac{0.014}{T_{ITM}}\right) \left(\frac{\mathrm{DARM_{offset}}}{10\ \mathrm{pm}}\right) \tag{3.2}$$

At high frequencies on the other hand the coupling is independent of power and approximately given by

$$K^{(2)}_{\mathrm{SRCL}} = 3 \cdot 10^{-5} \left(\frac{f}{100\ \mathrm{Hz}}\right)^2 \left(\frac{SRC_{\mathrm{detuning}}}{10\ \mathrm{degree}}\right) \left(\frac{0.014}{T_{ITM}}\right) \left(\frac{\mathrm{DARM_{offset}}}{10\ \mathrm{pm}}\right) \tag{3.3}$$

We therefore need two SRCL to DARM correction paths, one that scales with arm power, and another static one. Both need to be accurate to about 1%.

3.6 Error and control signal size

Using the Optickle and Loopticke model the in-loop (i.e. loop-suppressed) error signals were calculated and plotted in Figure 17.

Also, Figure 18 show the required drive to the test masses. It was calibrated in Newtons acing on a free, 40 kg test mass, even though the other mirrors will be lighter (BS: 14.2 kg, PR, SR: TBD)

Finally, table 4 show the residual fringe offset. DARM, PRCL, MICH and SRCL are all dominated by the micro-seism, but no resonant gain filters have been applied so far.

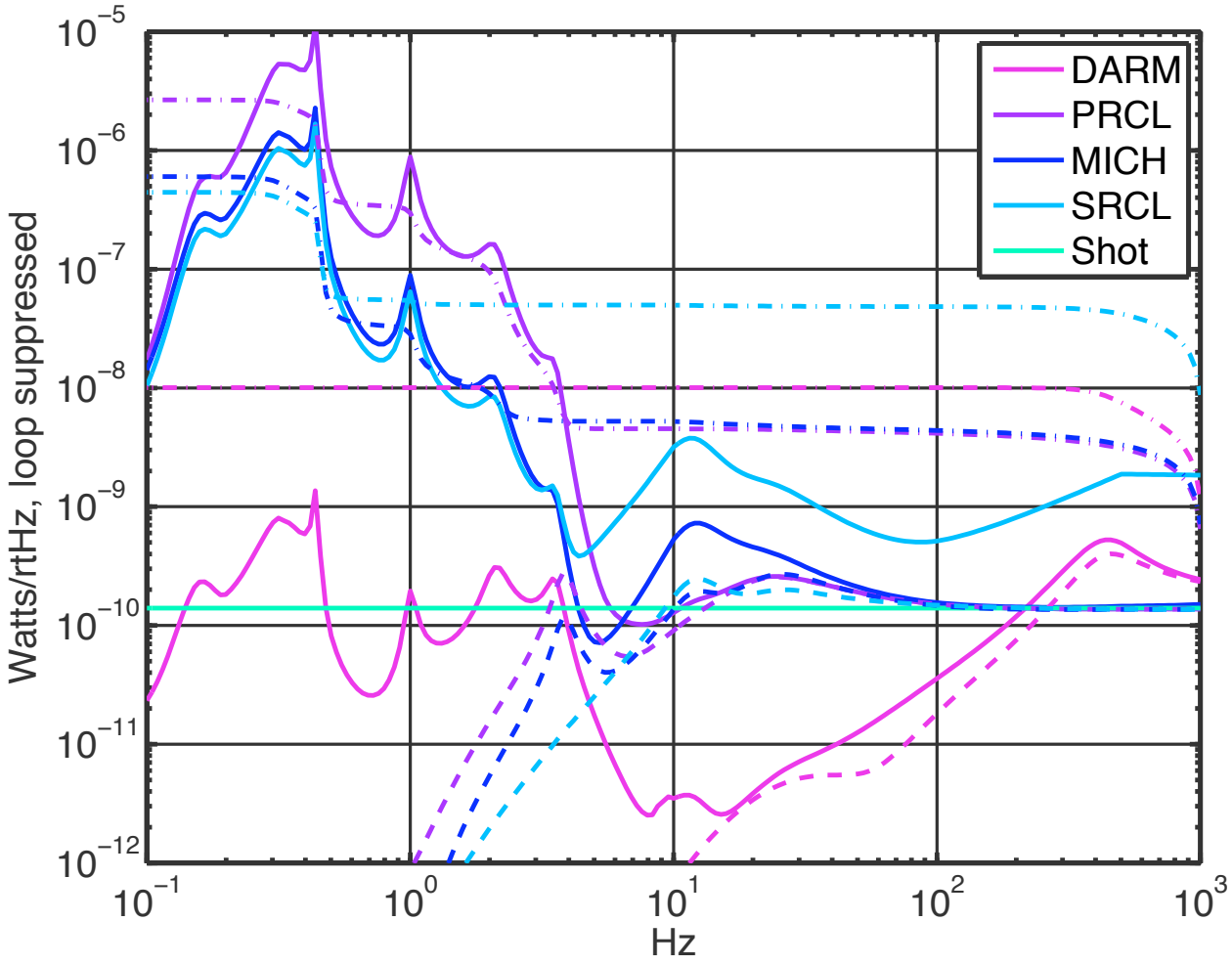

Figure 17: Error signals (loop-suppressed) for DARM, PRCL, MICH and SRCL. The corresponding RMS values (integrated from high to low frequency) are shown as dash-dot lines. The (loop-suppressed) quantum noise for each loop is shown as dashed lines. The (not loop-suppressed) sensing noise is indicated by the line labeled 'Shot'.

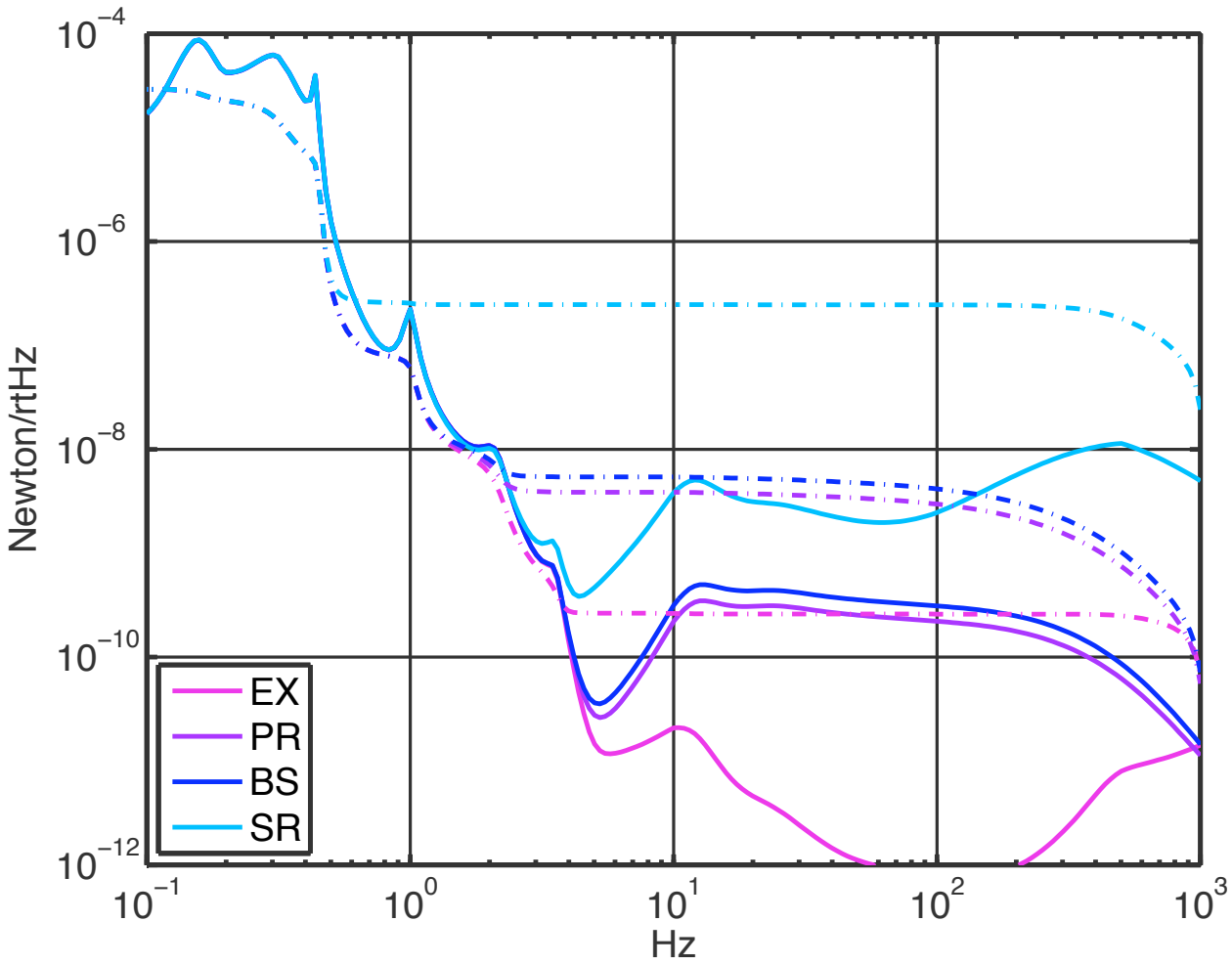

Figure 18: Control signals driving ETM, PR, BS and SR. All signals are calibrated in Newton at the test mass, assuming a free, 40 kg test mass (only appropriate for ETM). The corresponding RMS values (integrated from high to low frequency) are shown as dash-dot lines.

4 Alignment Sensing & Controls

4.1 Overview

The alignment of optical axis of the interferometer cavities as well as the centering of the beam spots on the optics are achieved and maintained by the Alignment Sensing and Control Subsystem (ASC).

The Figure 19 gives an overview of the sensing part of the ASC. Some fraction of the light beams exiting the interferometer dark, reflected and pickoff ports is sent to the Wave Front Sensors (WFS). Each core optic is instrumented with an optical lever and viewed by a CCD camera. In addition, the transmitted beam of each optic will be monitored by a quadrant photo detector (QPD). The ASC sensor signals are processed and send to the optics through the Suspension (SUS) system.

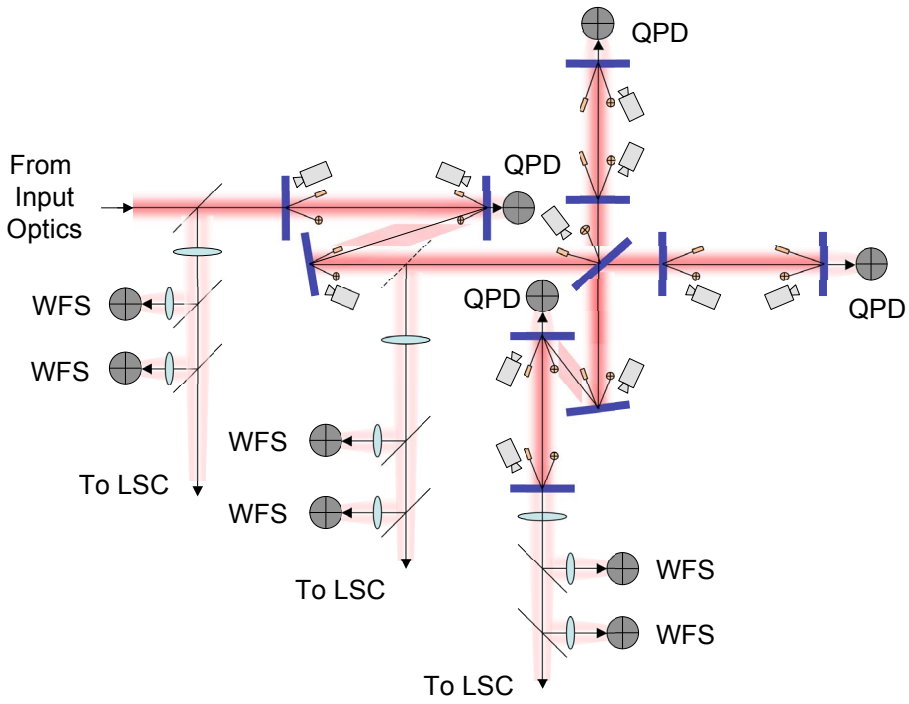

Figure 19: ASC sensor diagram.

4.2 Functions of the Alignment Sensing and Control System

The requirements for the residual angular motion of the test masses are specified in T070236.

- Before the interferometer longitudinal degrees of freedom are controlled by the LSC system the ASC system provides signals for the *initial alignment* of the cavity axes

to each other and the centering of the beams on the optics as well as the interferometer input beam alignment to the interferometer optical axes. The goal of the initial alignment is to attain a sufficiently high power buildup in the interferometer cavities so that the locking of the interferometer longitudinal degrees of freedom can begin.

- At the end of the lock acquisition sequence the longitudinal degrees of freedom become controlled by the LSC system and transition to the detection/science mode begins. Once the lock of all interferometer axial degrees of freedom is acquired, the angular degree of freedom control loops engage, providing the static optical cavities alignment and beam centering on the optics as well as the suppression of the optics angular motion up to several Hz.

- The ASC system implements the optical lever-based angular damping servos for those optics so equipped (optical lever hardware is provided by AOS). The optical levers are also used during the initial alignment step and for diagnostics purposes.

- The ASC system provides the damping of angular optical spring resonance produced by the radiation pressure from the main laser. In science mode, the role of the ASC is to maintain alignment of the optical cavities and prevent optical spring instabilities from building up. Consequently, the necessary unity gain frequency (UGF) of the ASC feedback system has to be about a factor 3 larger than the optical spring frequency. The slope of the feedback system at UGF shall be 1/f with additional low-pass filters kicking in at about 3 times UGF. As the UGF is a function of the power and the power as well as the displacement sensitivity depend on the mode of operation, the requirements on the ASC depend weakly on the mode of operation.

4.3 Assumptions and Dependencies

We assume that:

- The residual angular motion of the optics in the absence of radiation pressure from the main laser beam is assumed to meet the design requirements as specified by the suspension system design requirements document (T010007-01). These requirements are:

  - Test masses: $5 \times 10^{-18} \frac{\text{rad}}{\sqrt{\text{Hz}}} \frac{[10\,\text{Hz}]}{f}$ Pitch and Yaw, beam centering $< 1\,\text{mm}$
  - Recycling mirrors: (Beam centering $< 5\,\text{mm}$)

    Yaw: $2.7 \times 10^{-14} \frac{\text{rad}}{\sqrt{\text{Hz}}}$ at $10\,\text{Hz}$ falling to $1 \times 10^{-15} \frac{\text{rad}}{\sqrt{\text{Hz}}}$ at $100\,\text{Hz}$

    Pitch: $4.4 \times 10^{-14} \frac{\text{rad}}{\sqrt{\text{Hz}}}$ at $10\,\text{Hz}$ falling to $1.7 \times 10^{-15} \frac{\text{rad}}{\sqrt{\text{Hz}}}$ at $100\,\text{Hz}$
  - Beamsplitter: (Beam centering $< 5\,\text{mm}$)

    Yaw: $1.3 \times 10^{-15} \frac{\text{rad}}{\sqrt{\text{Hz}}}$ at $10\,\text{Hz}$ falling to $4 \times 10^{-17} \frac{\text{rad}}{\sqrt{\text{Hz}}}$ at $100\,\text{Hz}$

    Pitch: $2.9 \times 10^{-15} \frac{\text{rad}}{\sqrt{\text{Hz}}}$ at $10\,\text{Hz}$ falling to $8.6 \times 10^{-17} \frac{\text{rad}}{\sqrt{\text{Hz}}}$ at $100\,\text{Hz}$

- The optical lever design is part of the Auxiliary Optics System (AOS) design. The optical lever digital signal processing is done in the ASC.
- The ASC uses the same resonant and non-resonant phase modulation sidebands as LSC with frequencies and modulation indices.
- The CCD camera images of the beams on the optics and surrounding structure are sufficient to achieve the locking of the axial degree(s) of freedom in the following optical configuration(s): the simple Michelson interferometer (the input test masses plus the beam splitter), power- and/or signal-recycled Michelson interferometer(s) (the simple MI plus power- and/or signal-recycling mirror(s)).

4.4 Initial Alignment

During the initial alignment procedure it is assumed that:

- the input mode cleaner is aligned and locked in all degrees of freedom.
- the input mode is Gaussian (for example no clipping at the Faraday isolator) and that the mode matching between the input mode and the common arm cavity eigenmode is at least 95% w/o engaging any thermal compensation system.
- a subsystem of the LSC is installed which allows to lock each individual cavity alone.
- all mirrors can be sufficiently misaligned that each cavity and the short Michelson interferometer can be operated without being disturbed by any other cavity or interferometer.

At this stage the QPD signals and camera images will be used to center all beams on all mirrors and achieve an initial alignment stage where each individual arm cavity and recycling cavity can be controlled by a subsystem of the LSC when all other mirrors are sufficiently misaligned.

This goal of this stage is to get a first set of optical lever signals and QPD signals for the coarse alignment of the interferometer which

- reduces the angular and lateral mismatches between the various cavity eigenmodes to be smaller than their angular divergences and beam sizes.
- allows the LSC to achieve an initial lock of all longitudinal degrees of freedom.

4.5 Lock Acquisition

During the lock acquisition sequence the interferometer is brought from a state where the laser fields in the optical cavities are non-resonant and non-stationary to a state where the laser fields are close to resonance and stationary, and the cavity axial degrees of freedom are controlled by the LSC system.

In order to efficiently couple the input laser and the interferometer resonant fields as well as the interferometer cavity fields to each other, the relative angular and lateral mismatches between the various modes will further be reduced using the dither alignment scheme.

4.5.1 Dither Alignment Scheme

The initial alignment of the interferometer optics is achieved by sequentially locking the individual cavities starting with the single inline arm cavity, proceeding to the offline cavity and then to the power and signal recycling cavities. At each stage the pitch and yaw angles of appropriate optics are modulated in the frequency range from 5 to 15 Hz. The cavity power buildup and length sensing signals are synchronously demodulated to obtain the information about cavity alignment and beam centering on the optics. The beam centering can also be obtained using the QPDs and the camera. Fig. 20 shows the block diagram for the initial dither alignment scheme.

The dither alignment scheme and the initial alignment scheme using subsets of interferometers will need to be iterated to center the beam on each test mass and to center the action of the ASC actuators.

Note that the angular motion due to suspension noise rotates the mirrors around an axis through the center of mass of the test masses while the ASC actuators act on axis which also depends on the balance of the forces applied to the test mass. The beam has to be centerd within 1 mm with respect to center of mass and within 100 μm within the center of actuation of the ASC actuators for the test masses (TBD for the recycling mirrors, but it should be possible to do this during the commissioning phase).

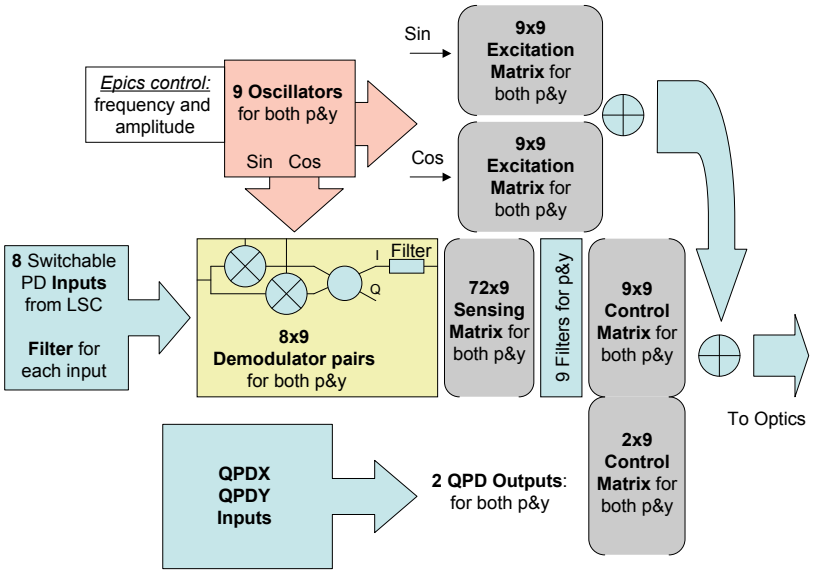

Figure 20: Initial dither alignment block diagram.

DC [W]	CR	SBu1	SBl1	SBu2	SBl2	DC
Dark	0.0021	0.000	0.000	0.0166	0.0166	0.0353
Refl	0.0026	0.0244	0.0244	0.0081	0.0081	0.0676
POP	0.2309	0.0088	0.0088	0.0011	0.0011	**0.2506**
OMC	0.000	0.000	0.000	0.0083	0.0083	0.0166
RF [W]	f1	f2	2xf1	2xf2	f2-f1	f2+f1
Dark	0.0001	0.0081	0.000	0.0332	0.0014	0.0023
Refl	0.0152	0.0068	0.0488	0.0163	0.0300	0.0563
POP	0.0893	0.0258	0.0176	0.0021	0.0109	0.0122
OMC	0.000	0.0040	0.000	0.0166	0.0007	0.0011

Table 5: DC and RF Power levels on the various detectors. These number include the assumed attenuation of the light power of 0.1 at Dark and Refl, 0.05 at OMC, and $2.5e-4$ for POP.

4.6 Detection Mode Alignment

In this state the misalignments of the optical cavities are sensed with the WFS array. The beam position on the end test masses is sensed by the ETM transmission QPDs. The video cameras that image the test mass faces can also be used to monitor beam position (as done in iLIGO for the beamsplitter beam position). There is also the possibility that optical lever damping of the quad suspensions, done at the penultimate mass stage, will be sufficiently useful and low-noise to remain engaged in detection mode.

4.6.1 Wavefront Sensing Scheme

In detection mode we use the well known wavefront sensing system, which measures the amplitude and phase of beat signals between 00- and 10-modes at various ports of the interferometer. The signals we have access to are the reflected port, the dark port, POX, and POP. The dark port signal can further be split up into a pick off of the dark port beam and the reflected field coming from the OMC. Note that the current design of the recycling cavity assumes a $\pi/2$ difference in the Gouy phases. As a consequence, the Michelson interferometer formed by the recycling cavities is dark for any 10-mode generated in the arms and the POX signals are strongly dominated by the X-arm tilts. This will allow us to lock the angular degrees of freedom of the X-arm independently from the Y-arm during lock acquisition in this phase.

However, for science mode operation we distinguish between the following six degrees of freedom: PR, SR, DITM, CITM, DETM, CETM.

25W Operation

The DC and RF power in the various ports in Case 1b are shown in Table 5. One potential wavefront sensing matrix for case 1a is shown in Table 6.

The scaling angle (α_0) for the ITM and ETM degrees of freedom are around 6 μrad. The

A/[α_0]	PR	SR	DITM	CITM	DETM	CETM
REFL f1 $\Psi_G = 5°$	**0.2858**	0.000	-0.0007	0.0130	0.0009	-0.0185
OMC 2f2 $\Psi_G = 160°$	0.0006	**0.0187**	0.0086	***-0.0175***	0.0010	0.0006
OMC f2mf1 $\Psi_G = 90°$	0.0001	-0.0002	**0.0846**	0.0001	0.0003	0.000
POP f1 $\Psi_G = 90°$	0.1249	0.000	0.0014	**0.3198**	0.000	***-0.2810***
DP f2 $\Psi_G = 10°$	0.000	0.0231	***-3.2937***	-0.0291	**3.6038**	0.0008
Refl f1 $\Psi_G = 90°$	***-0.5148***	0.000	-0.0063	***-1.4314***	0.0002	**1.5389**
OMC 2f2	0.0120	0.0312	-0.0385	**0.0782**	0.0265	-0.0038
POP f2 $\Psi_G = 90°$	0.0436	0.0001	-0.0017	**0.1118**	0.000	***-0.0981***

Table 6: ASC Sensing matrix for the non-detuned RSE case ($P_{in} = 25\,\mathrm{W}$, $\Gamma_{1,2} = 0.2$), in units of (amps/normalized angle). The RF-demodulation xphases are picked to give maximum signal. The bold straight entries are the ones we plan to use, the bold italic are the problematic ones. $\alpha_0 = \lambda/\pi\omega$ is the scaling angle, ω is the beam size on the tilted mirror.

	PRM	SRM	DITM	CITM	DETM	CETM
$\delta\alpha$ $10^{-15}\,\mathrm{rad}/\sqrt{\mathrm{Hz}}$	80	500	0.16	10	0.15	10

Table 7: Angle-equivalent sensing noise due to shot noise on the WFS. Shot noise is calculated using the power levels in Table 5, with the POP level limited to 100 mW. The sensing coefficients use the largest element in each column of Table 6, with some exceptions: PRM uses the element in the first row, since it is much better decoupled; CITM and CETM use the (rescaled) POP elements, since these DOF are so strongly coupled. The scaling angles for the PRM and SRM are 194 μm and 153 μm, respectively.

shot noise on the detectors is between $i_{sn} = 1 - 3 \times 10^{-10}\,\mathrm{A}/\sqrt{\mathrm{Hz}}$ on all relevant detectors. To calculate the angle-equivalent sensing noise of each DOF, we assume we can form the signal such that it is dominated by the largest element in the corresponding sensing matrix column. In general this gives an overly optimistic estimate of the noise, since other WFS signals will also be mixed in. However, we hope that for infiltration of WFS noise in the GW band, we can achieve something close to this by suitable filtering of the different channels. The sensing noise thus calculated are shown in Table 7.

125W-Operation

For operation at 125 W the power in REFL and POP require additional attenuation or parallel photo receivers. The DC and RF power levels shown in Table 8 for case 2 assume a 1% pick-off REFL and a $2.5e-5$ pick-off for POP.

A possible sensing matrix for this case is shown in Table 9.

The angle-equivalent sensing noise is calculated as before, and shown in Table 10.

DC [W]	CR	SBu1	SBl1	SBu2	SBl2	DC
Dark	0.0109	0.0001	0.0001	0.0096	0.0139	0.0347
Refl	0.0013	0.0122	0.0122	0.0114	0.0109	0.0480
POP	0.1154	0.0044	0.0044	0.0007	0.0012	0.1261
OMC	0.000	0.000	0.0001	0.0048	0.0070	0.0119
RF [W]	f1	f2	2xf1	2xf2	f2-f1	f2+f1
Dark	0.0004	0.0112	0.0002	0.0232	0.0035	0.0016
Refl	0.0076	0.0043	0.0244	0.0223	0.0150	0.0460
POP	0.0447	0.0106	0.0088	0.0018	0.0050	0.0080
OMC	0.000	0.0056	0.0001	0.0116	0.0017	0.0008

Table 8: DC and RF Power levels on the various detectors. These number include the assumed attenuation of the light power of 0.1 at Dark, 0.01 at Refl, 0.05 at OMC, and $2.5e-5$ for POP.

A/[α_0]	PR	SR	DITM	CITM	DETM	CETM
REFL f1 $\Psi_G = 5°$	**0.1431**	0.000	-0.0004	0.0069	0.0004	-0.0092
OMC 2f2 $\Psi_G = 160°$	0.0023	**0.01**	0.0016	-0.0073	0.0046	0.0003
OMC f2mf1 $\Psi_G = 90°$	0.0004	-0.0003	**0.2016**	0.0005	0.0006	0.000
POP f2 $\Psi_G = 90°$	0.0624	0.000	0.0010	**0.1599**	-0.0003	***-0.1405***
DP f2 $\Psi_G = 10°$	-0.0043	-0.0053	***-4.7349***	-0.0163	**5.1416**	0.01
Refl f1 $\Psi_G = 90°$	***-0.2570***	0.000	-0.0045	***-0.7157***	0.0016	**0.7694**

Table 9: ASC Sensing matrix for the detuned NS/NS case ($P_{in} = 125\,\mathrm{W}$, $\Gamma_{1,2} = 0.2$, ,$\phi_{SR} = 11°$). The RF-demodulation phases are picked to give maximum signal. The bold straight entries are the ones we plan to use, the bold italic are the problematic ones. $\alpha_0 = \lambda/\pi\omega$ is the scaling angle, ω is the beam size on the tilted mirror.

	PRM	SRM	DITM	CITM	DETM	CETM
$\delta\alpha$	140	800	0.11	8	0.10	8
$10^{-15}\,\mathrm{rad}/\sqrt{\mathrm{Hz}}$						

Table 10: Angle-equivalent sensing noise due to shot noise on the WFS. Shot noise is calculated using the power levels in Table 5, with the POP level limited to 100 mW. The sensing coefficients use the largest element in each column of Table 6, with some exceptions: PRM uses the element in the first row, since it is much better decoupled; CITM and CETM use the (rescaled) POP elements, since these DOF are so strongly coupled. The scaling angles for the PRM and SRM are $194\,\mu$m and $153\,\mu$m, respectively.

Mach-Zehnder and higher order sidebands

The code is currently only able to handle first order sidebands. The two signals which could be affected by higher order sidebands are the signals taken at the dark port. Nominally, the OMC signal should be carrier free and higher order sidebands should not create any problem. However, to play it safe, we studied the effect of higher order modes at the dark port instead of the OMC.

We first modeled the $2f2$ signals by changing the frequency of the $f1$ signal to $2 \times f_2$ and compared the original entries in that row of the sensing matrix with the new entries in that row. The difference was essentially zero.

To model the $f_2 - f_1$ sideband, we changed the f_1 frequency to $f_2 - f_1$ and calculated the signals at the dark port for this configuration for all degrees of freedom. The amplitude was in virtually all degrees of freedom three orders of magnitude below the amplitude in the WFS shown above (Case 1a), CETM was 'only' factor 400 smaller. Based on this we can go without a Mach-Zehnder.

4.7 Control Scheme

The modeling of the WFS-based alignment controls is just getting started. Compared to the iLIGO WFS system, we have the following challenges:

- WFS sensing noise must be sufficiently filtered out by 10 Hz, rather than 40 Hz
- we aim at achieving 1 nrad rms of residual test mass angular motion, rather than 10 nrad rms
- there is an optical spring resonance that must be stabilized by the ASC

On the other hand the seismic excitation of the test mass angles should be much smaller, owing to the SEI active isolation system. This helps with the first two challenges at least.

Expected angular motion

Figure 21 shows the modeled pitch motion of a test mass, as determined by the expected BSC ISI platform motion and the quad suspension dynamics. Because of the longitudinal-to-pitch coupling inherent in the suspension, we expect the pitch motion to be larger than the yaw motion (as in iLIGO). This predicts we need a factor of 50 stabilization from the WFS servos to reach a residual motion of 1 nrad rms, though notably suppression is needed only below 0.5 Hz.

There are also hopes that a local optical lever system, sensing and acting on the quad suspension penultimate mass, can further reduce the pitch motion around the lowest eigenfrequency, to 10 nrad rms or lower.

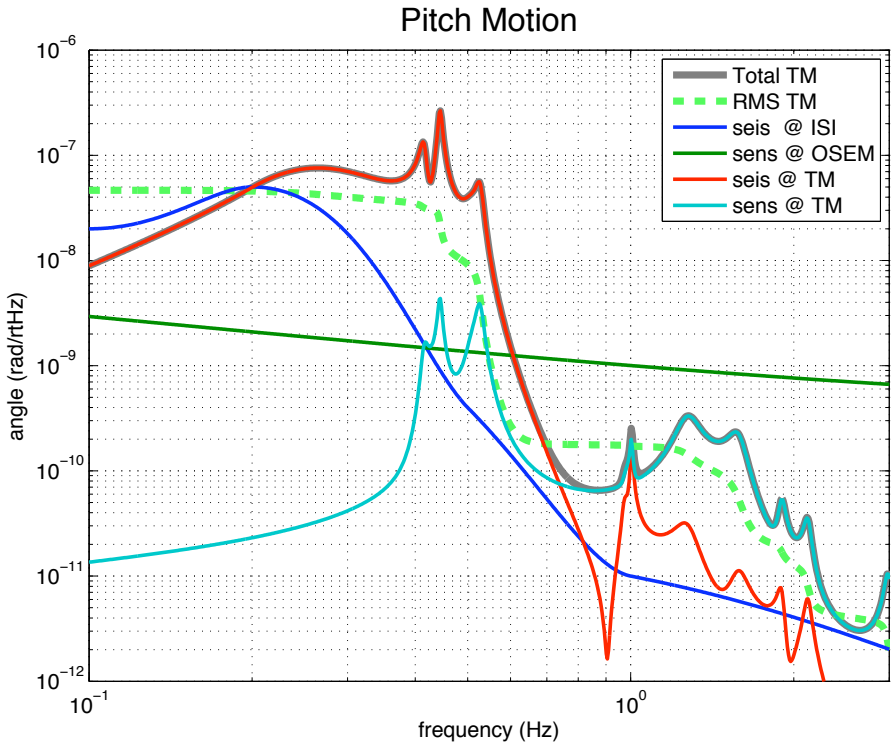

Figure 21: Modeled pitch motion of a quad suspension test mass, excited by seismic motion (i.e., BSC ISI platform, blue trace) and local sensor noise (dark green trace). The dashed bright-green trace gives the integrated rms pitch motion, which plateaus at about 50 nrad rms. (The suspension model used here has a higher minimum pitch eigenfrequency than the baseline model; this change is expected to be in the real design, precisely in order to reduce pitch noise.)

Bandwidth and noise infiltration

To reduce the residual angles to 1 nrad rms from the level shown in Fig. 21, a WFS bandwidth of a few Hz will be needed, so significant low-pass filtering can kick in around 10 Hz. If we can achieve a stable angle-to-length decoupling level of 10^{-4} m/rad, the open loop gain for the common mode test mass WFS signals would need to be 0.1 or less to get their noise below $10^{-19}\,\mathrm{m}/\sqrt{\mathrm{Hz}}$ in DARM.

It is not at all clear yet what kind of feedback we will need to stabilize the Siddles-Sigg angular instability. The eigenfrequency of the optical spring at $P = 125\,\mathrm{W}$ will be around 5 Hz. This would require a UGF of $10 - 15\,\mathrm{Hz}$ and the gain above 30 Hz can be rolled off faster than f^{-2} which is about the slope of the sensitivity curve. This represents the most demanding case in terms of bandwidth.

5 Photodetectors

5.1 Detector layout and detection frequencies

Figure 22 shows the layout for the main ISC photodetectors.

5.2 LSC RF Photodetectors

The main performance requirements for the LSC RF PDs that are used in science mode operation are: ability to operate at up to 100 ma of average photocurrent with no saturation; shot-noise limited detection at each of the detection frequencies, for photocurrents of 30 ma and greater. The 'shot-noise limited' criterion stipulates that shot-noise must dominate detector dark noise by a factor of 4 or more (in amplitude). RF photodetectors used only for acquisition will not need to handle such high photocurrent; the signal requirements of the acquisition detectors are still being determined.

Preamp. The initial LIGO LSC RF photodetectors use a resonant transimpedance formed with the photodiode capacitance and a tunable inductor, to make a single frequency tuned detector at the modulation frequency (25 MHz or 60 MHz). Notches are also added at twice the modulation frequency. For Advanced LIGO, there are some additional requirements and features that we want from the preamps:

- Higher frequency detection for lock acquisition (approximately 140 MHz)
- The ability to detect more than one RF frequency, typically the sum and difference of the two modulation frequencies
- The ability to handle larger signals without showing non-linear noise production (i.e., larger dynamic range)

We plan on changing the preamp to the series resonant circuit described by H. Grote in Ref. [2]; see also the circuit analysis by R. Abbott in Ref. [3]. This circuit type provides the

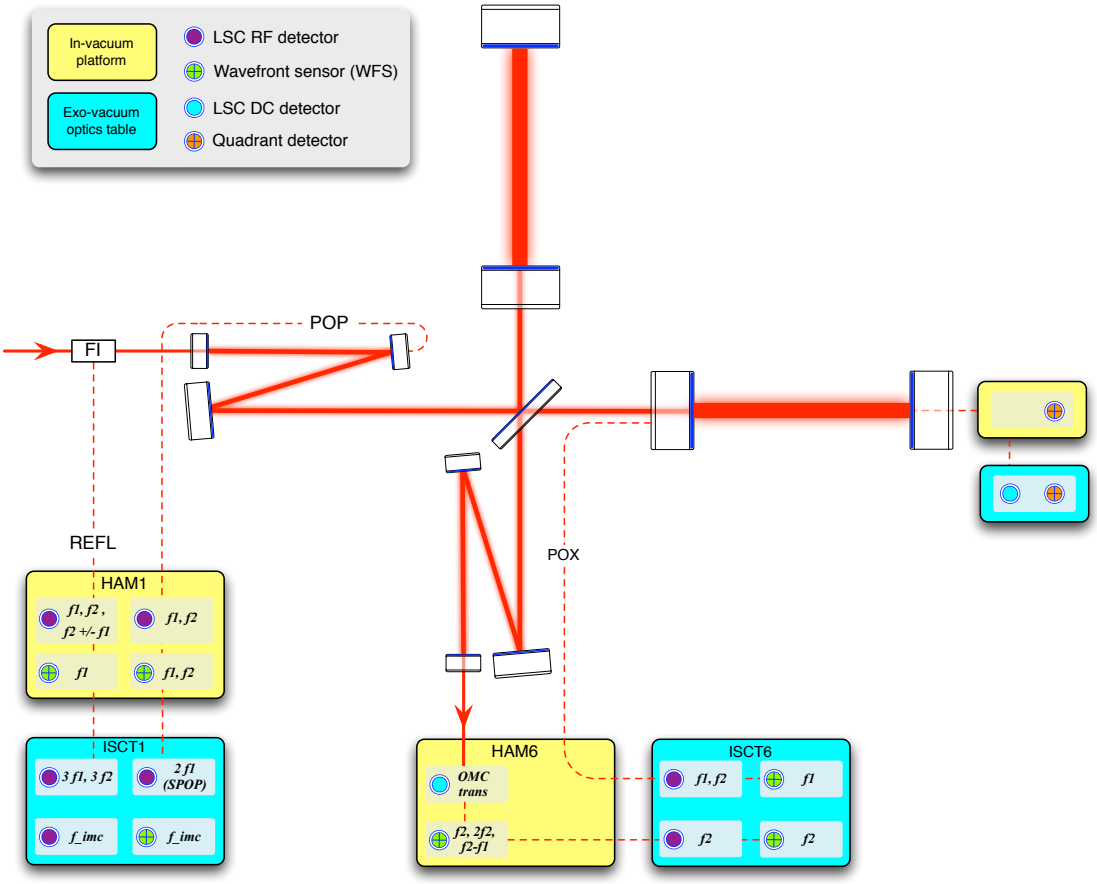

Figure 22: Layout of the ISC detectors.

second two features above. It will probably also be used for the high-frequency detection, but its performance is mostly determined by the photodiode capacitance.

Diodes. The initial LIGO diodes (Perkin-Elmer C30642G) are 2 mm diameter, and are capable of handling 100 ma of photocurrent. Thus they should be adequate for Advanced LIGO, but larger diodes could provide more margin for beam positioning, damage, etc. We will investigate whether 3 mm diameter diodes could be used, and still achieve the required sensitivity. New diodes on the marker will also be characterized and considered as alternatives to the PE units. There is also the possibility that the back-illuminated diodes being developed at Stanford will produce units capable of significantly higher photocurrent (200 ma is the goal); see Ref. [4].

Vacuum Packaging. To reduce vibrational noise contaminating the photodetection (through scattered light, beam clipping, or diode non-uniformities), all LSC RF PDs that are used in-loop will be operated in-vacuum, mounted directly to seismic isolation platforms (acquisition detectors will still be mounted outside the vacuum). The concept for this is to mount the preamp in a hermetically sealed box, with the diode itself mounted on the outside wall of the box (i.e., in the vacuum) with a hermetic socket; see Fig. 23.

5.3 LSC DC Photodetectors

These are the detectors that detect the light transmitted by the output mode cleaner, provide the error signal for the DARM loop, and of course provide the GW signal. Their main performance requirements are: ability to operate at up to 100 ma of average photocurrent with no saturation; shot-noise limited detection in the band 10 – 10,000 Hz, for photocurrents of 5 ma and greater; quantum efficiency greater than 90%. In this case, shot-noise must dominate detector dark noise by a factor of 10 or more.

DC photodetectors have been designed and built for Enhanced LIGO; they also serve as prototypes for AdvLIGO. These units, described in what follows, have been designed with AdvLIGO in mind. Experience with their operation in EnLIGO will inform any design changes for AdvLIGO.

Diodes. We will use 3 mm diameter InGaAs diodes. Several commercially available diodes have been tested, and the best one is the Anadigics PD3M:

Quantum efficiency	$> 99\%$
Reflectivity @7.5° incidence	0.3%
BRDF	10^{-4}/str
Thermal resistance, junction-to-case	14° K/W

Table 11: Parameters of the Anadigics PD3M, 3 mm diameter InGaAs photodiode.

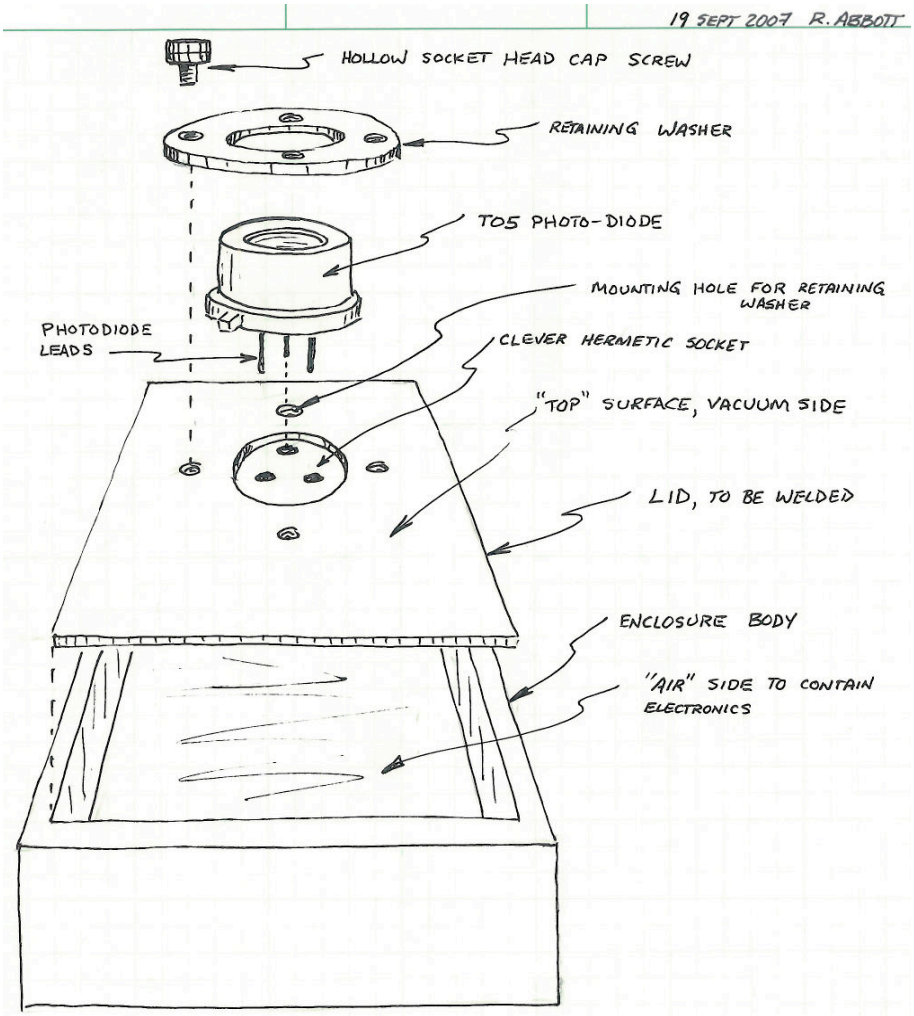

Figure 23: Concept for in-vacuum RF photodetector.

Preamp. The main design choice for the front end is whether to use a simple load resistor, or a transimpedance amplifier. We chose a load resistor because of the lower power dissipation of this design (the op-amp doesn't have to source the photocurrent). The preamp includes two selectable load resistors, and some signal whitening. A block diagram is shown in Fig. 24, and the full schematic is D060572 (rev B1 the latest as of this writing).

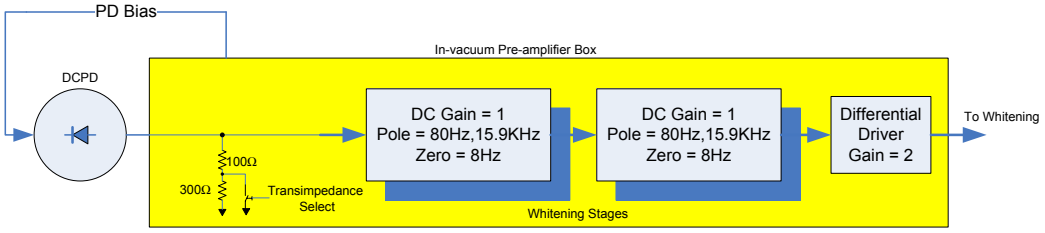

Figure 24: Block diagram of the in-vacuum photodetector for detecting the main output light of the interferometers (homodyne detector).

Figure 25 shows the modeled and measured noise spectra of the detector. The low frequency measured noise, below about 30 Hz, may be limited here by insufficient resolution in the measurement. Nonetheless, even assuming the modeled input noise, there is still some work to do to get the dark noise to be 10 times lower than shot at the very low frequency end.

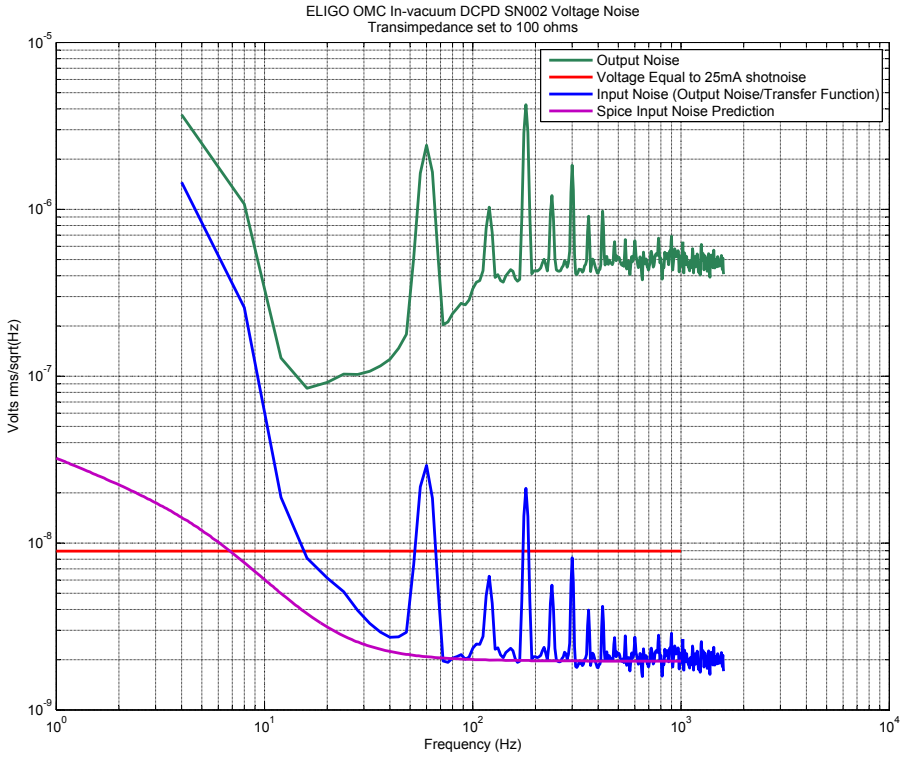

Figure 25: Modeled and measured voltage noise of the DC photodetector (D060572). The transimpedance was selected to be 100 ohms.

Vacuum Packaging. The photodetector packaging must be designed for vacuum compatibility and power dissipation. The preamp is enclosed in a hermetically sealed (laser welded) aluminum box. The photodiodes (sans window) are mounted separately, and are exposed to vacuum. The cable connecting the diode to its preamp is approximately 10 cm long.

Power handling was designed for 1 W dissipation in the diode (100 ma at 10 V bias), and 1.25 W dissipation in the preamp (100 ma through a 100 ohm resistor, plus 1/4 W for active devices). The diode is mounted to an aluminum radiator, approximately 60 cm^2 surface area. The radiator is coated with a high-emissitivity coating (aluminum oxide, $\epsilon = 0.96$), giving a thermal impedance of 18° K/W. So at 100 ma photocurrent, the estimated diode junction temperature rise is $14° + 18° = 32°$ K. The preamp box is also coated with aluminum oxide, and the load resistors are mounted directly to the inner walls of the box. The measured temperature rise of the preamp box (in-vacuum) is 14° K per watt.

5.4 ASC RF Photodetectors (Wavefront Sensors)

As in initial LIGO, we employ wavefront sensors (WFS) for global alignment sensing. These are RF photodetectors with similiar requirements to the LSC RF PDs, expect each detector uses a quadrant photodiode and thus has four RF channels. Compared to the initial LIGO WFS, we need the following added features:

- Much higher power detected – up to 100 mW (compared to a few mW)
- Multiple RF frequency detection (for some WFS)
- In-vacuum operation

We also plan on orienting the quad diodes in the '+' orientation, rather than the '×', as suggested by Kawabe [5].

Diodes. We will use quadrant InGaAs photodiodes, which weren't available for initial LIGO. Compared to the enhanced silicon diodes used now, these offer twice the responsivity, and the ability to handle high power. On the other hand they are smaller; the largest InGaAs quad diodes currently available are 3 mm diameter. We have characterized four InGaAs quad diodes, and the results are on the AdvLIGO wiki.[1] Our preferred device is the OSI Optoelectronics Q3000. Per quadrant, with a 10 V reverse bias, the diode capacitance and series resistance are 50 pF and 38 Ω, respectively (measured at 50 MHz). The optics have been tested optically, up to 50 mW on a segment, to look at the cross-coupling between quadrants. Fig. 26 shows the result; we believe a maximum segment coupling of −20 dB will work, which means these diodes can be used up to about 100 MHz.

5.5 ASC Quadrant Photodetectors

As in initial LIGO, we will use low-frequency quadrant detectors in the ETM transmission monitors, for beam centering. For AdvLIGO, we are adding two quad detectors on each ISC

[1] http://ilog.ligo-wa.caltech.edu:7285/advligo/ASC_Photodetection

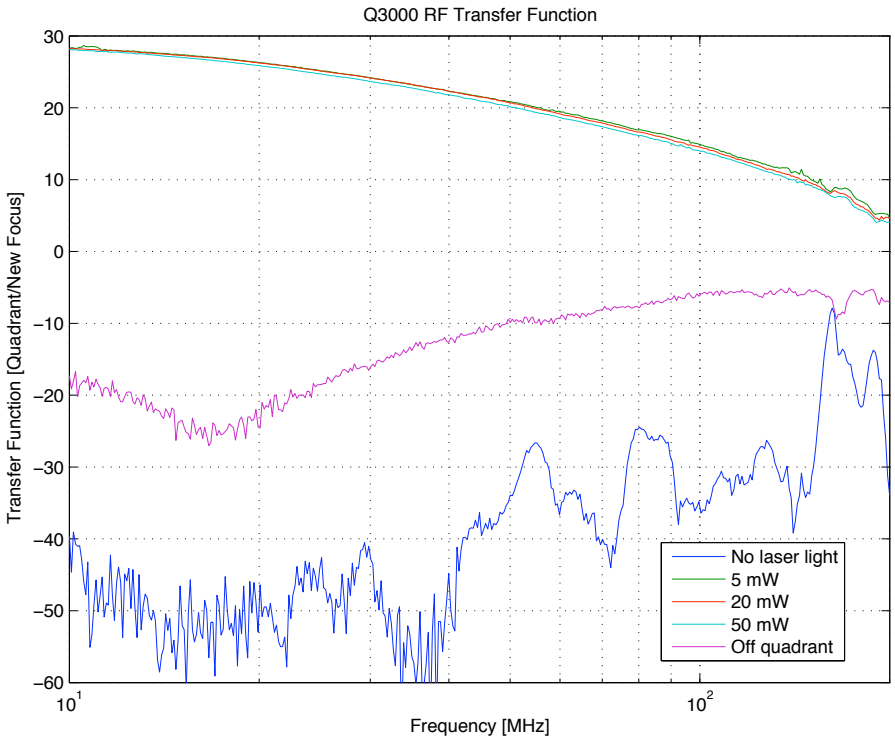

Figure 26: Response of the Q3000 quadrant diode, and cross-coupling between segments. Measurements made with an amplitude modulated diode laser (1064 nm), and the signal in each quadrant was read out with a 50 ohm load resistor. The 'Off quadrant' trace shows the cross-coupling to a non-illuminated segment.

beam line, for beam pointing control and stabilization. Performance requirements:

- Power handling: up to 100 mW for ETM transmission monitor; up to 10 mW for other beam lines
- Bandwidth: DC – 10 kHz
- In-vacuum operation

We will use the same 3 mm diameter quadrant diodes (OSI Q3000) as is planned for the WFS. The preamps will be standard transimpedance amplifiers; it is not clear whether the preamps need to be located in the vacuum system. We are supplying several such quad detectors for the EnLIGO readout chain, where the preamps are located outside the vacuum chamber. Experience with these detectors will tell us whether this will work for AdvLIGO, or whether to instead design in-vacuum preamps.

6 RF Source, Distribution & Demodulation

6.1 RF Source and Distribution

In contrast with the Initial LIGO, the Advanced LIGO RF components will take the heretical stance of keeping the good and throwing out the bad. Figure 27 is a representation of the building blocks used in distributing signals from the point of generation, to the point of use. Maintaining a clear sense of modularity to the design will allow leveraging using outside vendors to provide design solutions. Modular systems are more easily reconfigurable as the need arises.

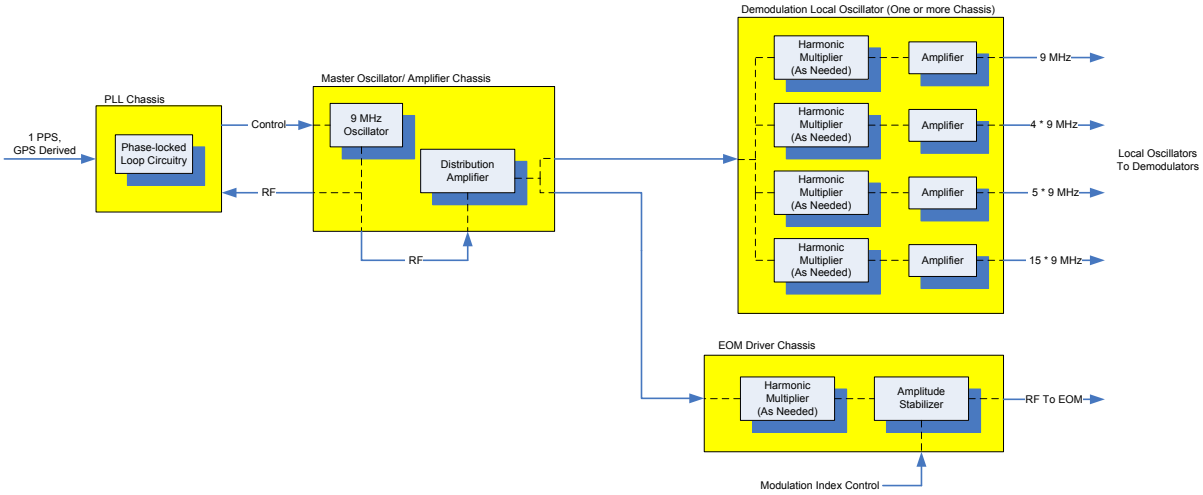

Figure 27: Block diagram of the proposed RF distribution system.

All RF oscillators will be phase-locked to the GPS based Master Timing System. This prevents non-stationary noise sources generated by unintentional mixing products. Frequency

distribution is accomplished by transmission of the fundamental 9 MHz signal in order to preserve a fixed phase relationship at each point of use. Predictable phase relationships are a side benefit to distribution systems based on frequency multiplication, vs. a system using frequency division.

All blocks in the frequency distribution separated by cables will employ means to avoid ground loops. This requires transformer coupling of RF inputs, and careful attention to system connections to power and monitoring subsystems. The signal levels in the transmission cables will be approximately 10 to 20 dBm to be significantly larger than competing noise, but not burdensome from the standpoint of RF leakage.

The inclusion of monitoring points at the design phase to measure the frequency, phase, amplitude, phase-lock status and other key performance related parameters is mandatory.

RF drive signals will be required for the Input Optics (IO) Modulators. The exact requirement for amplitude stabilization will be determined by comparing the residual AM noise in the distribution system RF signal to the IO AM noise requirement.

6.2 RF Demodulation

The ASC and LSC subsystems use heterodyne RF Demodulators to extract audio signals from RF modulation. Initial LIGO LSC loops used passive diode based demodulators, whereas Initial LIGO ASC loops used an active demodulator.

It is desirable, although not critical, that the AdLIGO demodulators are identical for the ASC and LSC functions. Certainly, this eases manufacture and testing.

Among the key performance requirements for the AdLIGO demodulators, linearity of the demodulation process is a watershed topic. Although no direct evidence pointed to a demand for increased linearity, active demodulators using FET switches offer promise of improved linearity in the presence of large RF signals. An R&D program is currently underway to examine tradeoffs between the two types of demodulators. Some areas of research for this program are:

- Active feedback to maintain RF quadrature in the I&Q (in-phase and quadrature) demodulator local oscillators.
- A low noise audio pre-amplifier boosts the level of the demodulated signals.
- Signal strength readback for the incident RF signals and the local oscillator.

7 Sensing Chains

In this section we cover the design of the ISC sensing chains, by which we mean the opto-mechanical and opto-electronic hardware for conditioning and detection of the various beams (other than custom photodetectors, which are covered in the preceding section). There are two significant differences in the design for the AdLIGO sensing chains compared to initial LIGO:

- Detection of all beams whose signals are used in science mode ISC servo control is done in-vacuum, on vibration isolated platforms.
- Active beam steering and stabilization is provided for the in-vacuum beam lines (except the ETM transmission detection)

7.1 Tip-Tilt Mount

For the active beam steering, we need a vacuum-compatible mirror mount that has suitable range and bandwidth. Some vibration isolation is also desirable to reduce scattered-light path length noise. It is hard to know how much range is really needed, but probably at least a few millirad. The bandwidth required for beam pointing stabilization is expected to be tens of Hz or less. On the other hand, we intend to generate alignment signals for the output mode cleaner via dither of the beam direction; this small-amplitude dither should be at as high a frequency as possible.

One option for the mount is a commercial PZT-based tip-tilt mirror, such as used in the iLIGO RBS system. However, these units have some disadvantages: their range is small (few mrad); in our experience they are not very robust; they offer no vibration isolation. Given these downsides, we decided to develop our own mount instead. The design concept for these is something between the Newport Fast-Steering Mirror and the iLIGO small-optics suspension (SOS). The design, called a tip-tilt mount, has been developed and tested at ANU, and is being implemented on the eLIGO OMC beam line.

The tip-tilt mount is based on a single loop wire suspension system, designed to hold a 2 inch diameter mirror. The actual mirror is mounted inside a metal ring to which the suspension wires are clamped. This mirror assembly is suspended by two separate wires of equal length which are clamped on each side. Also attached to this metal ring are four magnets, which are used in conjunction with the Birmingham OSEMs (BOSEM) for angular control and position.

The BOSEMs, in combination with large NEO magnets (10 mm diameter x 10 mm length), can achieve a force coefficient of 2.05 N/A. We assume a maximum coil current of 100 ma (it may be a little higher for the BOSEMs, 150-200 ma). Figure 28a shows the maximum mirror deflection with 100 mA of current through the OSEMs. At 1 kHz, the angular deflection is ~ 7 μrad. Figure 28b shows the maximum effective coil current and available torque. The corner in the current response is due to the coil inductance and the series resistor in the coil driver, which can easily been compensated for by modifying the output filter in the coil driver.

The tip-tilt suspension was designed so that all the resonant frequencies (longitudinal, pitch and yaw) are above 2 Hz. The Tip-Tilt mirror will be mounted on top of an isolated platform, which has resonances up to ~ 2 Hz. Although the isolated platform will be controlled, to prevent damage to the mirror in the situation that these controls fails, the table resonance will not overly excite the Tip-Tilt resonances.

The length of the suspension wire is 5.5 mm which makes the main pendulum resonance 2.12 Hz. The pitch resonance depends on the position the suspension wire is attached to the optic in respect to the centre of mass (c.o.m.) of the mirror assembly. This is set to

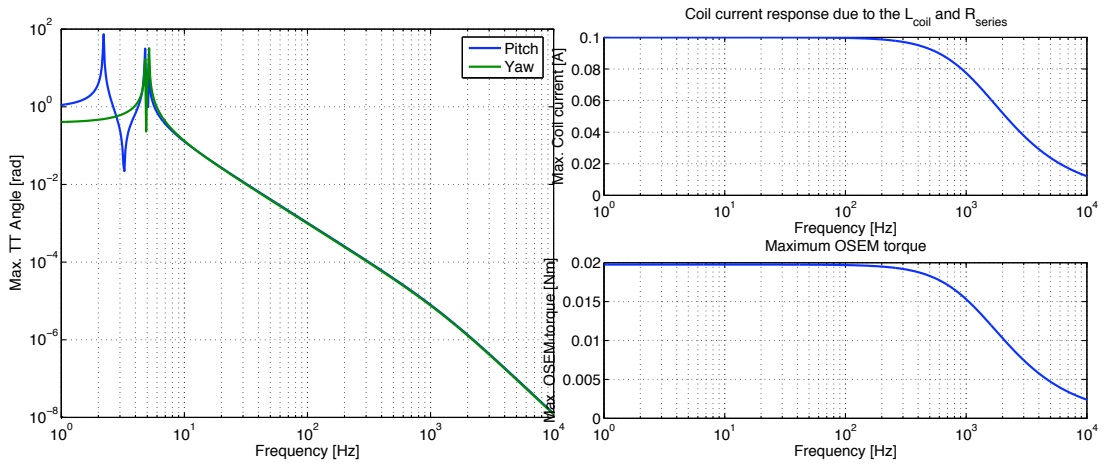

(a) (b)

Figure 28: a. Max. angular deflection with maximum allowable OSEM drive current; the dashed red line indicates the angular limit due to mechanical constraints (11 mrad) b. Coil driver output current response (top) and maximum OSEM torque response (bottom) due to the series resistor (100 Ω) and the coil inductance (13.1 mH).

1.1 mm above the c.o.m. resulting in a pitch resonance of 4.98 Hz. The yaw resonance is controlled by the separation of the suspension wires at the suspension point in respect to the effective diameter of the optic. This separation is set to 60 mm, resulting in a yaw resonance of 4.63 Hz. An attempt is made for the vertical bounce mode (or violin mode) to coincide with the iLIGO core optics vertical bounce mode, which is 343 Hz. This is achieved by using a suspension wire of 380 μm. All the major first order resonance frequencies are shown in table 12, while figure 29 shows the Tip-Tilt design drawing.

With four OSEMs, only three degrees of freedom (DOF) can be controlled (pendulum, pitch and yaw). The other three DOF, side, roll and vertical, are damped using Eddy Current Damping (ECD), which is located at the front of the mirror; see figure 29.

All modes of the tip-tilt suspension (except the high frequency ones) are actually strongly eddy-current damped, through the conductive BOSEM bodies. This makes the units easy to work with; they don't wobble too much even when the active controls aren't engaged.

Mode	Modeled	Measured	Deviation
Pendulum	2.04 Hz	2.27 Hz	10%
Pitch	4.42 Hz	5.35 Hz	17%
Yaw	4.92 Hz	5.46 Hz	10%
Side	3.02 Hz	3.07 Hz	2%
Vertical	371 Hz	*nm*	–
Roll	477 Hz	*nm*	–

Table 12: The measured and modeled resonance frequencies of the Tip-Tilt Stage (*'nm'*, not measured).

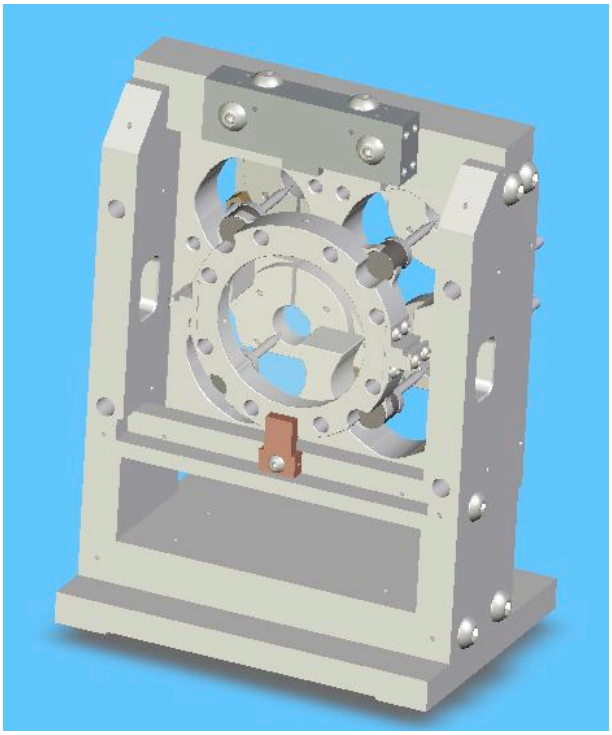

Figure 29: Drawing of the Tip-Tilt Stage (with no OSEMs).

This damping does limit the vibration isolation, though. Figure 30 shows the longitudinal transmissibility (modeled) with the measured damping coefficient (0.38 kg/s). The isolation factor at 10 Hz is 3.7. If it is determined that more isolation is needed, the BOSEM form material could be changed to something less conductive than aluminum.

7.2 ETM Transmission Detection

As in iLIGO, the beam transmitted by each ETM is used both for lock acquisition and beam position control in science mode. There is a very large dynamic range in this beam that must be accommodated; when a single arm cavity is locked, a few microwatts of power must be detected with good SNR, and with the full, high-power interferometer, the transmitted power is around 4 watts (see Table 13).

The conceptual design for the ETM detection is shown in Fig. 31. The design was guided by the following considerations: the quadrant detector used for low-noise operation should be located in-vacuum; detectors used for lock acquisition and transition are mounted outside the vacuum; dump as much light as possible in-vacuum, on an isolated platform; keep the in-vacuum hardware as simple as possible.

For the in-vacuum beam dumping, we propose mounting a steering mirror on a moveable stage, which would be inserted in the beam path to direct the beam to the dump (as opposed to making the dump itself moveable). The moveable stage design is TBD, but might be a rotary stage, or a flipper-mount type. The movement does not have to be fast (say, < 10 sec), nor does the registration of the steering mirror have to be particularly accurate, since it just points the beam into the dump. The dump itself will be a V-geometry trap made of low

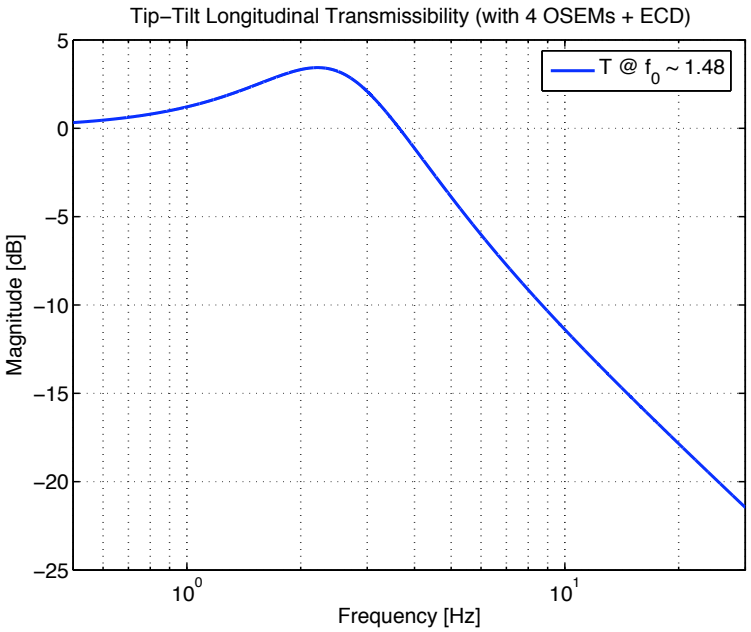

Figure 30: Calculated longitudinal transmissbility of the tip-tilt mount, using the measured eddy-current damping factor.

Input Power	ETM Trans. Power, full IFO	ETM Trans. Power, single arm
1 W	35 mW	18 μW
5 W	165 mW	
20 W	0.7 W	
125 W	4.4 W	

Table 13: Power levels in the ETM transmission beam for different cases. The minimum power we want to detect with good SNR (> 100, e.g.) is $1/10 - th$ the single arm power, or about $2\,\mu$W. These numbers are calculated assuming an ETM transmission of 5 ppm.

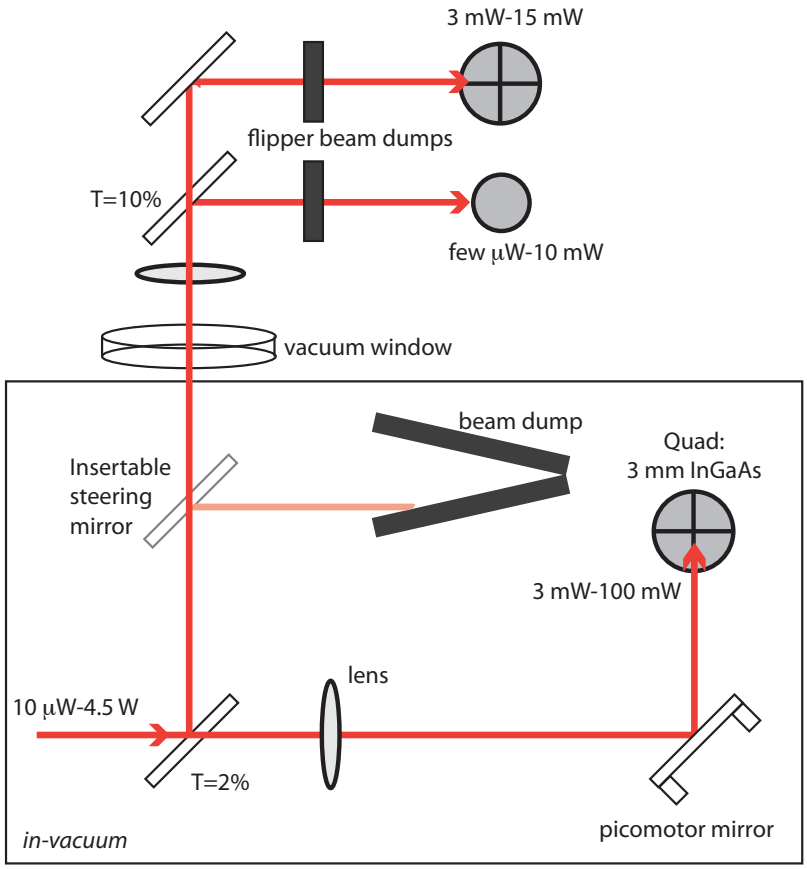

Figure 31: Concept for the ETM transmission detection. The in-vacuum components are mounted on a platform with the ETM beam reduction telescope; the platform is suspended from the BSC ISI. The exterior components will be mounted on an optics breadboard/table. Next to each detector is listed the power range over which that detector is expected to operate. Since only $\sim 100\,\mathrm{mW}$ is needed on the in-vacuum quad at full power, only a small fraction of the beam is taken for this. The beam delivered by the reduction telescope is 15 mm diameter, so further reduction is needed for the quad detector, likely with one lens as shown. The beam is steered to and centered on the quad with a picomotor-actuated mirror. It is not yet clear whether the preamps for the quad will be in the vacuum (we'll be guided by experience with eLIGO detectors); if so, the vacuum packaging developed for the LSC DC detectors can be used here. For acquisition, most of the exterior beam is directed to a single-element detector that must be sensitive enough to detect a fraction of the single arm power (i.e., microwatts; this can probably be a commercial detector, Thorlabs, e.g.). Its output will be sent to two or more ADC channels with different gain scalings, to cover the 3-4 orders of magnitude of this signal. A small fraction of the exterior beam is sent to a quad detector. The quad sum output can be used if the dynamic range of the first detector is exceeded. Also, the beam position information may be used during the power increase stage, to counteract radiation torques on the test masses. Each of these detectors is equipped with a flippable dump for protection (design TBD). For science mode operation, the high-power beam is dumped in-vacuum by inserting a HR steering mirror in the beam path to direct the beam to a dump instead of allowing it to exit the vacuum. Both the steering mirror and the vacuum-dump are mounted on the isolated platform.

back-scatter material; the top and bottom of the V will also be closed off. Some material options are: black glass; polished stainless-steel; steel coated with black ceramic.

7.3 Reflection port detection

The ISC sensing needs only $\sim$ 10% of the reflected power for its detectors. The REFL sample beam will be directed from HAM2 into HAM1, through a window in the HAM1-HAM2 septum plate. The beam line in HAM1 will include two tip-tilt mounts for beam direction control. We expect to sense the beam direction with two dedicated quadrant detectors on the HAM1 platform (as opposed to using the WFS/s on this beam line). A REFL beam sample will also be directed outside the vacuum onto ISCT1. This beam is used for the REFL lock aquisition detectors, and other monitors such as a video camera.

In HAM1, the optics platform is not being supplied by SEI, and is instead the responsibility of ISC to design and provide. The plan as of now is to use an iLIGO HAM optics table, but we do not yet have a firm concept for its vibration isolation. The scattered light analysis found later in this section suggests the isolation requirements are modest – a factor of ten isolation at 10 Hz. A couple of options for achieving this, which will be explored in the preliminary and final design phases, are: use iLIGO stack elements, but with fewer layers (so isolation starts at a lower frequency); an external passive mount, hopefully commercially supplied (e.g., from Minus-K or TMI).

7.4 Pick-off port detection

The POP beam (leakage through PR2) is extracted into HAM1. ISC will determine the transmission of this mirror, at a value that provides sufficient power for all modes of operation. We assume for now a transmission of 250 ppm, which would provide 6 mW-1.5 W in this beam, over the input power range 5-125 W. Since we don't plan on detecting more than 200 mW of power, at higher powers most of the light will need to be dumped. The dumping will be done in-vacuum, using something like the dump described for the ETM transmission detection.

7.5 Anti-symmetric port detection

The AS beam is delivered through the ISC into HAM6 by AOS, having passed through the output Faraday isolator and the HAM6 septum window. Description of the AS beam detection is found later in the section on the output mode cleaner (Section 8).

7.6 Input Mode Cleaner detection

ISC provides sensing and control of the input mode cleaner (IMC) length/frequency and alignment. Currently we plan on the IMC reflected beam detection being entirely outside the vacuum, as it is for iLIGO. It is not thought that these are sensitive channels with regards to scattered light or beam clipping. If deemed necessary in the future, the IMC detection could instead be done in HAM1, on the same isolated table on which the reflected beam is

detected. For the baseline (exo-vacuum) design, the detection chain design will be the same as it is for iLIGO.

7.7 Back-scattered light analysis

Here we analyze the back-scattering of light in the ISC detection chains back into the interferometer, and the resulting noise in the strain readout. Scattering from the AS port has been analyzed in T060303-00 [6]; repeating here the main conclusions:

- the back-scattered power is dominated by that from the output mode cleaner
- fluctuations in the optical path between the OMC and the signal recycling mirror must be below a level that is a few times smaller than the target HAM ISI platform noise at 10 Hz; i.e., ISC steering mirrors mounted to the HAM ISI should have some $f > 10$ Hz isolation.
- the HAM6 septum window for the AS beam may or may not be a problem for backscatter, depending on the level of scatter from this optic, which needs to be measured.

We expect the tip-tilt mount will provide enough (longitudinal) vibration isolation as currently designed (factor of about 4 at 10 Hz), though as mentioned earlier this could be increased by reducing the eddy-current damping. Regarding the septum window, we have the option of just removing it if necessary.

We follow the same analysis for the other ports: compute the coupling transfer functions; estimate the back-scattered light power; determine the limit on optical path noise.

Reflection Port. The coupling from reflection port retro-reflection to DARM has been calculated with the Optickle model. The full results can be found in the AdvLIGO wiki (under 'REFL_back-scatter'); here we use the result at 10 Hz to set the following requirement:

$$2.5 \times 10^{-8} \cdot (R_{sc}/10^{-6})^{1/2} \cdot x_{sc} < 10^{-20}\mathrm{m}/\sqrt{\mathrm{Hz}}\,. \tag{7.1}$$

The left hand side is the equivalent DARM noise due to scattered light, with the leading factor coming from Optickle (at 10 Hz), and the right hand side is the technical DARM noise limit at 10 Hz; R_{sc} is the back-scattered reflection coefficient, and x_{sc} is the scattered light path noise.

Apply this first to the septum window separating HAM1 and HAM2. The solid angle of the REFL beam (2.2 mm radius) is of order 10^{-7} str. We assume the AR of the window is 100 ppm, and its BRDF at 5 deg incidence is $10^{-4}\mathrm{str}^{-1}$, both of which are believed to be upper limits. Note that we plan on sampling 10% ($= R_{sample}$) of the full REFL beam. Then the fractional back-reflected power is $R_{sample}^2 \cdot R_{AR} \cdot \mathrm{BRDF} \cdot \Omega = 10^{-17}$. The path fluctuations back from the window would then need to be $x_{sc} < 10^{-7}\,\mathrm{m}/\sqrt{\mathrm{Hz}}$, which looks safe since the maximum window motion is expected to be $10^{-8}\,\mathrm{m}/\sqrt{\mathrm{Hz}}$.

Next we apply this to the ISC REFL detection chain, the back-scattering from which is expected to be dominated by the LSC photodiode; the fractional back-reflected power from this element is:

$$\mathrm{BRDF}_{diode} \cdot \Omega_{diode} \cdot R^2_{sample} = 10^{-4} 10^{-6} 10^{-2} = 10^{-12} \tag{7.2}$$

The path noise limit is then $x_{sc} < 4 \times 10^{-10} \mathrm{m}/\sqrt{\mathrm{Hz}}$. LVEA floor motion is typically about 10 times above this, so the HAM1 detection table needs about a factor of 10 vibration isolation at 10 Hz.

ETM Transmission Port. This coupling is simple to calculate because it looks just like a GW; the requirement at 10 Hz is thus:

$$T_{\mathrm{ETM}} \cdot \sqrt{R_{sc}} \cdot x_{sc} < 10^{-20} \mathrm{m}/\sqrt{\mathrm{Hz}}\,, \tag{7.3}$$

or $x_{sc}\sqrt{R_{sc}} < 2 \times 10^{-15}\,\mathrm{m}/\sqrt{\mathrm{Hz}}$.

For a path reflecting from the chamber wall/window ($x_{sc} \sim 10^{-8}\,\mathrm{m}/\sqrt{\mathrm{Hz}}$), we would require $R_{sc} < 4 \times 10^{-14}$ – which is why we plan on dumping all unused beams inside the chamber, before they can hit anything which moves so much. For the in-vacuum paths, assume the transmission detection platform has a residual motion of $\sim 10^{-14} \mathrm{m}/\sqrt{\mathrm{Hz}}$ at 10 Hz (1-2 orders of magnitude isolation from the BSC platform). Then the back-reflected power must be held to $R_{sc} < 0.01$, which is easily manageable.

8 Output Mode Cleaner

Advanced LIGO will employ DC readout for the DARM error signal. This choice is in part motivated by technical noises associated with RF readout, and in part by the recognition that the carrier light resonating in the 4 km arm cavities provides the most stable reference oscillator available. This section describes the decisions made in the design of the Output Mode Cleaner and their impact on the Advanced LIGO readout noise.

8.1 OMC Topology

The OMC is a cavity at the AS port of the IFO whose length is actively locked to the IFO carrier frequency. OMC The overall OMC design has been chosen to maximize the filtering of the RF sidebands and higher order spatial modes consistent with integration into a dual pendulum suspension. The suspension has been designed to provide additional vibration isolation for the OMC and to reduce the relative motion between the OMC and SRM in the gravitational wave detection band. The cavity bandwidth is given by

$$\omega_p = \frac{c}{L}\frac{\pi}{\mathcal{F}} = 1.9\ MHz\ \left[\frac{1\ m}{L}\right]\left[\frac{500}{\mathcal{F}}\right], \tag{8.1}$$

where $\mathcal{F}$ is the finesse, L is the cavity round trip length, and $\pi = 3.14$ is π. Naively, we would maximize the finesse in order to lower the cavity pole. In practice, we are limited by

the finite loss of the cavity mirrors to more modest values of $\mathcal{F}$. Given a round trip power loss of l, the decrease in transmission is

$$\delta P_T \approx -\frac{\mathcal{F} l}{\pi}. \tag{8.2}$$

For a reasonable round trip loss of 100 ppm and a finesse of $\mathcal{F} = 500$, the transmission loss is 1.5%. The choice of finesse fixes the‘q input and output coupler transmission to

$$T = \frac{\pi}{\mathcal{F}} = 6300\ ppm \left[\frac{500}{\mathcal{F}}\right]. \tag{8.3}$$

Higher order Gaussian modes (HOMs) accumulate a Guoy phase shift as they propagate through the stable OMC cavity. Ideally, they will not resonate in the OMC when it is locked to the TEM_{00} carrier and their contribution to the DC signal will be filtered by the cavity. The round trip phase shift accumulated by a TEM_{mn} mode is

$$\phi_{mn} = 2\,(m+n)\arccos g, \tag{8.4}$$

where the cavity g-factor is given by

$$g = 1 - \frac{L}{2ROC}, \tag{8.5}$$

for a symmetric cavity with two mirrors of radius of curvature ROC. ROC and L will be chosen to maximize the filtering for the RF and HOMs sidebands. To calculate the filtering, a model is required for the power in the HOMs and the RF sidebands present at the output port. These depend on currently unspecified details such as the RF modulation frequencies, RF modulator configuration, and recycling cavity configuration. For the Enhanced LIGO OMC, an $ROC = 2\ m$ and a length of $1.44\ m$ was chosen. Assuming the HOM power is distributed as $P_{mn} = (m+n)^{-1}$, this should give a filtering of better than $5e-4$ in power. Since the HOM content of the high power IFOs is not well understood, the OMC mechanical design can accommodate an range of cavity lengths.

There is an additional parity term not shown in Eq. 8.4 for HOMs with odd parity in cavities with an odd number of reflections which doubles the mode density. For this reason and to maximize the cavity path length within the suspension, the OMC will be a 4 mirror bow-tie cavity. The angle of incidence (AOI) on the cavity mirrors is compromise between scattering and astigmatism. Because of the finite mirror Back Reflected Distribution Function (BRDF), the AOI is larger than 5 degrees. However, the orthogonal axes incident on a curved mirror have different focal lengths (by $\cos(AOI)$). The resulting astigmatism breaks the degeneracy between horizontal and vertical HOMs, decreasing the filtering. For Enhanced LIGO, the $AOI \approx 6.5$ degrees.

The above considerations fix the cavity parameters, the cavity length, mirror reflectivity, mirror curvature, and the number of mirrors. A block diagram of the Enhanced LIGO OMC system is shown in Fig. 32.

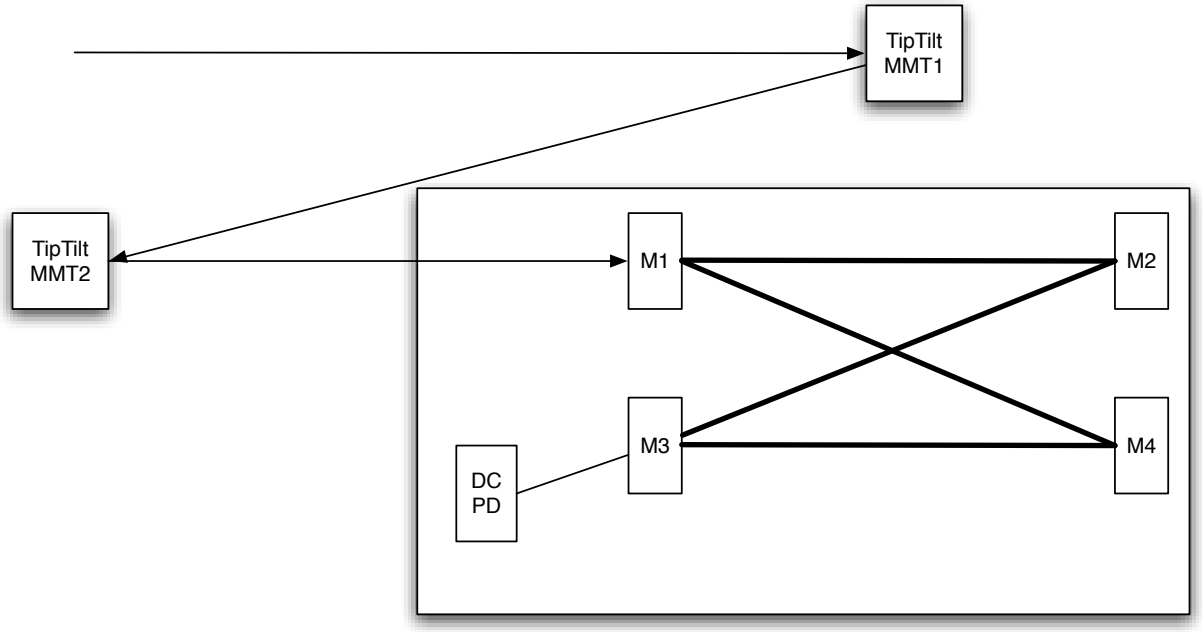

Figure 32: Block diagram of the OMC components.

8.2 OMC mechanical construction

In order to reduce the effects of vibrations and thermal noise on the OMC length, the OMC construction must maintain the inherent high quality factors of the materials with the highest possible resonant frequencies. A traditional fixed-spacer design does not provide the flexibility required to adapt the OMC design to a specific IFOs required OMC g-factor, nor does it allow simple mounting of the output photodiodes to the OMC spacer.

The Advanced LIGO OMC will be based on the breadboard and tombstone construction method shown in Fig. 33. The tombstones hold the optics and photo-detectors at a fixed height above the breadboard. The optic pitch is determined by the manufacturing tolerance of the breadboard and tombstone, chosen to be a conservative 30 μrad for the Enhanced LIGO OMC. The optic yaw is set during assembly. The substrate is made of Ultra Low Expansion (ULE) ceramic to minimize thermal expansion, while the tombstones and optics are made of fused silica. The fused-silica to fused-silica and fused-silica to ULE bonds are made with a vacuum compatible, high-strength, UV-cure epoxy which allows for precise alignment of the optics before bonding. The metal to glass bonds are either mechanical (with screws) or with the more compliant VacSeal UHV epoxy.

8.3 OMC control and noise

There are three main sources of OMC-induced noise: readout noise, cavity length fluctuations, and alignment fluctuations. The electronics noise related to readout has been addressed in Section 5.3. The remaining known issue is noise arising from pointing fluctuations on the diode sampling inhomogeneous gain. This term is expected to be minimized by mounting the DC photo-detectors directly to the OMC mechanical substrate, thereby greatly reducing

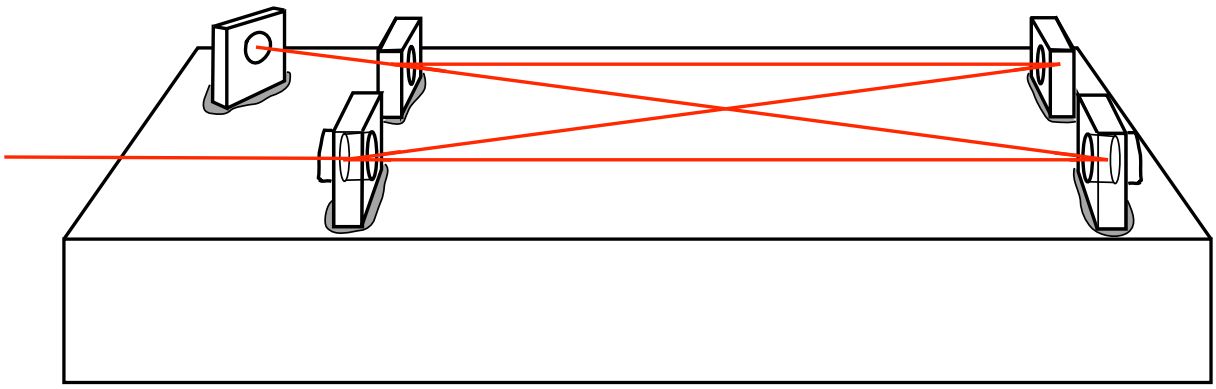

Figure 33: OMC breadboard and tombstone construction.

the possible pointing fluctuations.

8.3.1 Length control and noise

Length actuation is necessary in order to lock the OMC to the IFO output beam. The Enhanced LIGO OMC has two length actuators, a high-frequency, low range PZT and a low-frequency, high range thermal actuator system (OTAS). The PZT is bonded directly between the OMC spacer and a cavity mirror. The OTAS consists of an aluminum cylinder and heater mechanically attached to the OMC spacer and bonded to a cavity mirror. The noise contribution from these two elements is expected to overwhelm the thermal noises described above. However, the PZT actuator has a natural actuation bandwidth of ≥ 50 kHz which, in theory, will allow a high-bandwidth control loop to suppress the OMC length noise. In practice, the OMC length servo will be limited by cross-coupled noise terms that are not well understood. If length noise suppression is unnecessary, the Advanced LIGO OMC may do without a PZT between a mirror spacer and rely on slow thermal tuning. Results from the Enhanced LIGO OMC will be used to determine the final Advanced LIGO actuator requirements.

The OMC length noise is fundamentally limited by the thermal noise of the OMC mechanical spacer, mirror substrates, and mirror coatings. Following the derivations in *PRL93, 250602*, the noise terms are:

$$G_{spacer} = \frac{4k_BT}{\omega}\frac{L}{3\pi R^2 E}\phi_{spacer}, \tag{8.6}$$

$$G_{substrate} = \frac{4k_BT}{\omega}\frac{1-\sigma^2}{\sqrt{\pi}Ew_0}\phi_{substrate}, \quad \text{and} \tag{8.7}$$

$$G_{coating} = \frac{4k_BT}{\omega}\frac{2d\,(1-\sigma-2\sigma^2)}{\pi E w_0^2}\phi_{coating}. \tag{8.8}$$

Here G is the single sided displacement power-spectrum, T the temperature, L the Fabry-

Perot cavity length, R the radius of a cylindrical spacer, E the Young's modulus, σ the Poisson ratio, d the coating thickness, and w_0 the beam waist. The loss angle ϕ is a function of the material. The three noise sources are roughly comparable, assuming the cavity construction can maintain the high Q values of the bulk material. For a linear cavity constructed using similar materials as the OMC, the authors calculate a displacement noise at 10 Hz of $2 \times 10^{-18}\,\mathrm{m}/\sqrt{\mathrm{Hz}}$. We have not done detailed simulations of the thermal noise since For Enhanced LIGO, the mechanical aspects in the OMC assembly (for instance, the length actuator assemblies) are expected to dominate the OMC length noise. The actual Enhanced LIGO OMC length noise will be investigated using the 4 km IFO arm cavities as a reference.

8.3.2 Angular control and noise

Beam jitter of the IFO output beam incident on the OMC will generate noise in the OMC transmission. This has been analyzed by V. Mandic in Ref. [7]. The predicted motion of the IFO arm cavity mode is sufficient to contribute to the OMC noise spectrum at an unacceptable level if left uncorrected.

The OMC auto-aligment will be done using dither locking. The tip-tilt steering mirrors will be dithered in pitch and yaw in the kHz regime to obtain an error signal on the DC photodiodes in transmission through the OMC. In effect the dither will slightly misalign the beam incident on the OMC, creating sidebands at the dither frequency. The signal at the DC photodiodes will be demodulated at this frequency to obtain an error signal for the pitch and yaw degree of freedom. This will be done for both tip-tilt mirrors, which in total will amount to four degrees of freedom (pitch and yaw for in the near-field and far-field). Each degree of freedom can have its own dither frequency, resulting in 4 additional signals around one kHz. In addition there will be cross-modulation products in the lower frequency regime (around 100 to 500 Hz). One approach is to dither each tip-tilt mirror with a single frequency, but the pitch and the yaw dither signals are 90-degress out of phase. This will result in the beam making a circular motion at the OMC waist. There are only 2 dither frequencies required, and when the frequencies are separated by ~ 1 kHz, the cross-product will be at one kHz also. The dither signals on the DC photodiodes need to be strong enough to be measured, but not dominate the DC photodiode signal in the detection band.

In addition, two quadrant photodetectors are mounted on the OMC breadboard, and these signals can also be used to monitor, and possibly control, the alignment.

The OMC alignment servo could be required to have a bandwidth as high as 100 Hz. The alignment noise will be studied in detail by the Enhanced LIGO OMC.

9 Lock Acquisition

The lock acquisition strategy presented here is being designed in order to reach the operating point in a deterministic way and in a short time (not longer than a few minutes). In other words, we want a technique which is robust, fast and easy to implement. In this section results for lock acquisition of a broad-band signal recycled IFO are presented. Once the IFO is locked in this configuration, the operating point for the detuned case can be reached by

changing continuously the control scheme, as described in figure 7.

9.1 Optical Configuration

The optical parameters adopted (see Table 14) are slightly different with respect to the ones proposed at the beginning of this document, but no significant differences in the interferometer response are expected.

Quantity	Value (Final design value)
Arm Finesse	621 (446)
ITM transmission	0.010 (0.014)
PRM transmission	0.0318 (0.027)
SRM transmission	0.19 (0.2)
Schnupp asymmetry	0.043 (0.05)
l_{PRC}	55.815 m
l_{SRC}	9.563 m (57.410 m)
l_{EX}	3994.75 m
l_{EY}	3994.75 m
Lower mod. frequency (f1)	$9,399,566$ Hz
Upper mod. frequency (f2)	$46,997,832$ Hz
Modulation index (f1, f2)	0.2

Table 14: Optical parameters adopted in the lock acquisition simulation. The current values chosen for Advanced LIGO, when different, are reported in parenthesis.

9.2 Sensing and Control

By means of an SPI [8], the locking sequence starts with the arm cavities locked away from resonance, with the CARM d.o.f. detuned by about 10 nm with respect to the operating point. The d.o.f's of the central cavity (PRCL, MICH, SRCL) are then locked, so as to have a globally controlled state of the IFO from the beginning of the locking sequence. From this stable state, the IFO is brought to its operating point by progressively reducing the CARM offset. In order to do that, we have to deal with several problems. First of all, we need to find a good error signal for CARM in presence of a CARM detuning, when standard Pound-Drever-Hall signals are not good error signals. Moreover, the CARM detuning induces an optical resonance, whose frequency is proportional to the detuning itself (75 Hz/nm) The optical resonance changes therefore its frequency while the CARM offset is reduced. The frequency response of all the signals sensitive to CARM changes as well, and it needs to be compensated in order to have a stable loop over the whole sequence. Good error signals for the central cavity have to be found as well. They need to be as independent as possible from the CARM detuning, to avoid complicating the locking sequence. The error signals investigated for the science mode configuration do not have these features. Suitable error signals have been selected after investigating their behavior by means of the frequency domain simulation Optickle (see appendix C).

In the following paragraph the locking sequence will be described in terms of the CARM offset. Figure 34 gives us an idea of how much power circulating in the IFO is associated with a given CARM offset. It shows the power measured in transmission of one arm cavity of the signal-recycled IFO as function of the CARM offset, normalized with respect to the power measured when PRM and SRM are misaligned (about 60 μW, single cavity configuration). When the IFO is on its operating point, about 1000 times more power is expected to be measured in transmission than the single cavity case.

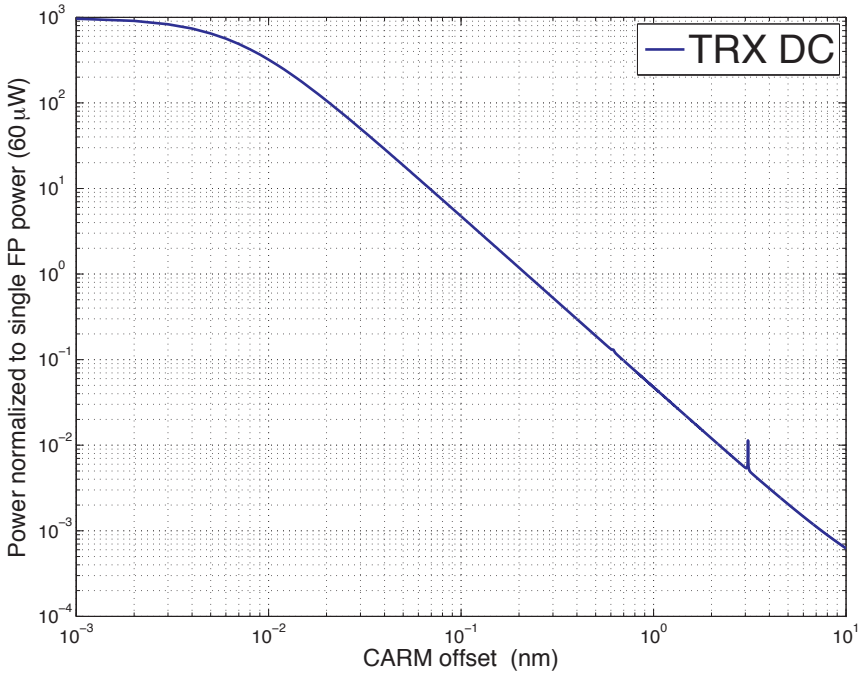

Figure 34: Power transmitted by one arm cavity in signal recycled configuration, normalized by the power measured in single cavity configuration (PRM and SRM misaligned).

9.2.1 Arm cavity error signals

The use of the power signals transmitted through the arm cavities as error signals has been investigated, following the strategy adopted in the experimental locking tests carried on at the LIGO-40m laboratory [9]. Figure 35 shows the frequency response to a CARM motion of a combination of the two arm cavities transmitted powers (TRX_DC and TRY_DC), more precisely the square root of the sum. The plot shows the optical resonance in the presence of different values of the CARM offset. The optical resonance frequency moves from several hundred Hz down to a few Hz. For offset values smaller than a few nm, the gain is almost constant above 200 Hz.

Concerning DARM, a good error signal turned out to be the difference between TRX_DC and TRY_DC, with a frequency response which is flat up to a few hundred Hz.

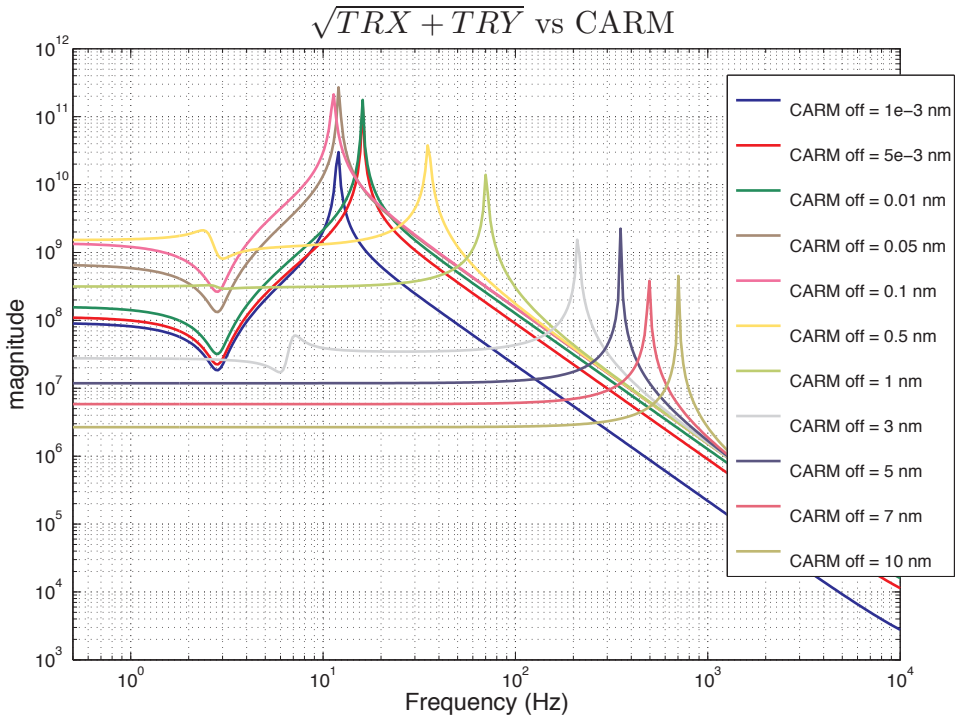

Figure 35: Frequency response of the CARM error signal $\sqrt{(TRX + TRY)}$ to a CARM motion.

9.2.2 Central cavity error signals

Standard Pound-Drever-Hall signals generated by the beating between carrier and sidebands and demodulated at the modulation frequency are strongly dependent on the behavior of the carrier inside the arm cavities. These signals are therefore affected by changes of the CARM offset, and they are not useful for controlling the central cavity d.o.f's in our scheme. Moreover, in broad-band configuration, double demodulation ($f_1 + f_2$, $f_2 - f_1$) does not provide useful error signals for control. In order to get signals which are independent from the CARM offset, the use of signals demodulated at three times the modulation frequency (3f) have been studied. The main features of these signals is that they are produced by the beating between 2f and f sidebands and between 3f sidebands with the carrier. The second contribution is typically smaller than the first one, so that the 3f signal depends very little on the carrier behavior [10]. Signals detected in reflection and demodulated at $3f_1$ and $3f_2$ are in fact very good signals for PRCL, MICH and SRCL, as shown in figure 36. For different values of the CARM offset, the behavior of a 3f-demodulated signal is compared with the single f-demodulated signal planned to be used in science mode. Where the f-demodulated signal is strongly dependent on the CARM offset, the 3f-demodulated signal is almost independent.

The resulting control scheme for lock acquisition is shown in Table 15.

Control filters for each degree of freedom are plotted in figure 37.

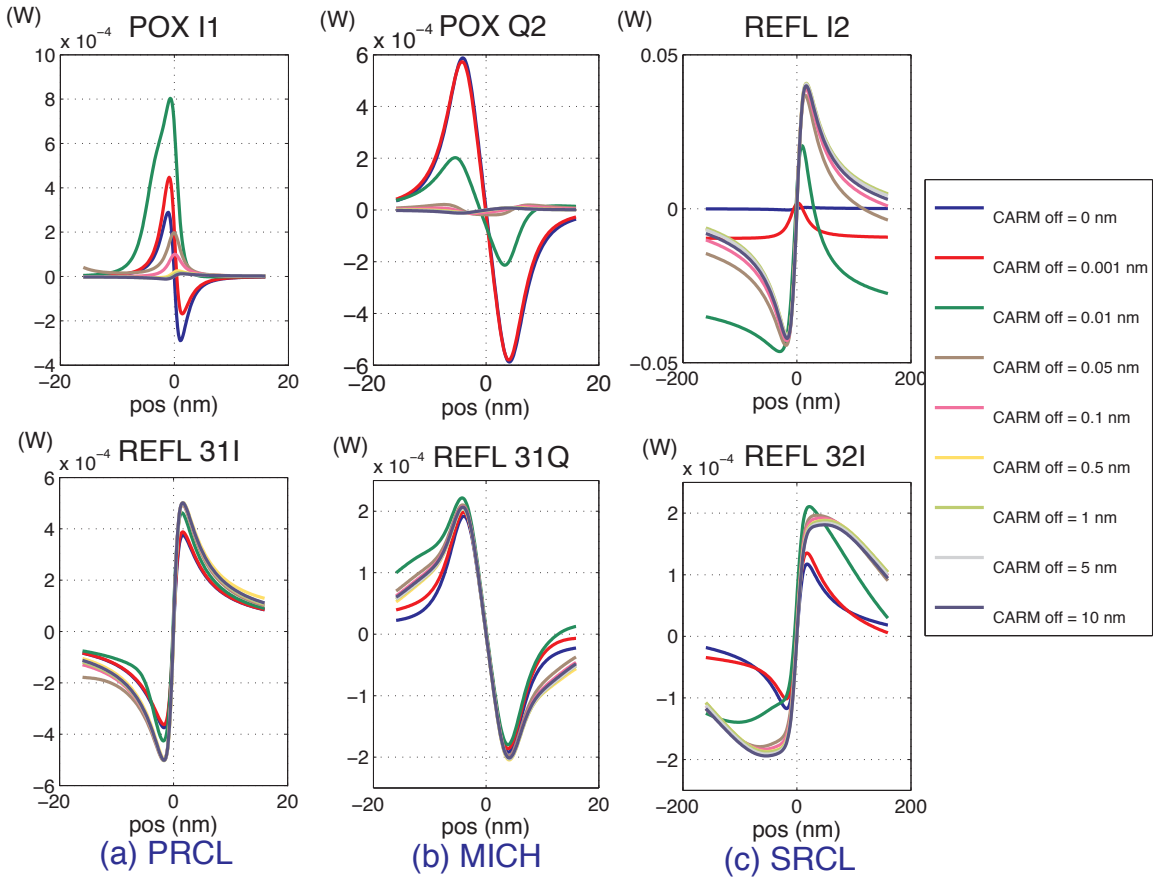

Figure 36: Error signals for PRCL, MICH and SRCL, plotted at different CARM offsets: (top) signal planned to be used in science mode; (bottom) signal 3f-demodulated. REFL 31 means signal extracted in reflection demodulated at the frequency $3f_1 \sim 28$Hz. Similarly, REFL 32 means demodulation at $3f_2 \sim 141$Hz. For MICH, both REFL 31Q and REFL 32Q show the same behavior (only REFL 32Q plotted here).

9.3 Time domain simulation of lock acquisition

A time domain simulation based on the E2E model has been developed in order to test the designed control scheme for lock acquisition. The main features of the simulation are the following:

- simplified suspensions (double pendulum for BS, simple pendulum for the other mirrors);
- saturation of the end mirror actuators at 200 μN (Electrostatic Drive limit), saturation at 10 mN for PR and SR (standard LIGO I actuators), 600 mN for BS (actuation from the penultimate mass);
- shot noise, electronic noise (see section 9.4 for details).

D.o.f	Error signal	Driven Mirrors
CARM	$\sqrt{TRX + TRY}$	Frequency servo
DARM	$TRX - TRY$	ETMX, ETMY
PRCL	REFL 31I	PRM
MICH	REFL 31Q (or REFL 32Q)	BS, PRM, SRM
SRCL	REFL 32I	SRM

Table 15: Summary of the error signals used to control each d.o.f during lock acquisition, and the mirrors driven by the relative correction signals.

As described in [11], the lock acquisition with full power entering the IFO (125 W) would be compromised by radiation pressure effects. For this reason, we plan to acquire the lock with a lower incoming power, which will be then brought to its nominal value once both longitudinal and angular controls are active. This simulation uses 1 W of incoming power, and assumes therefore that radiation pressure effects and thermal effects are negligible. A proper simulation of the SPI is not present yet. Its behavior is reproduced by setting the initial position of the end mirrors so as to have both DARM and CARM offsets of a few nm, then sweeping the end mirrors to reduce the CARM offset. The central cavity is locked when the arm cavities are away from resonance, and remains stably locked during the CARM offset reduction. When the transmitted power of one of the two arms goes above a given threshold, that arm is locked by using the transmitted power as an error signal. The threshold is set at about 30μW, which corresponds to half of the transmitted power in single cavity configuration. This power level can be easily reached by reducing the CARM offset with the SPI given less than a 3 nm initial offset for DARM. Since the SPI will provide an accuracy of about 1 nm on the mirror positions, this requirement is not stringent. As soon as the transmitted power of the second arm goes above the threshold, a common and differential control of the two cavities is engaged, according to the control scheme described in table 15. The DARM control is done by fed-back to the end mirrors. The CARM d.o.f. is instead expected to be controlled by feed-back to the laser frequency, with an initial loop bandwidth of about 200 Hz (see section 9.3.1). From this globally controlled state, the CARM offset is then progressively reduced. The final step of lock acquisition consists of moving the control of the arm cavities from DC to RF signals (REFL I1 for CARM and AS Q2 for DARM).

Figure 38 shows the full lock acquisition of the IFO.

9.3.1 Frequency servo

In initial LIGO a globally controlled stable state of the IFO is reached only at the end of the lock acquisition sequence [12]. A frequency servo is engaged when the IFO is already on its final operating point. The feedback to the laser frequency is fully analog, with a bandwidth of about 20 kHz. With the locking scheme described here the IFO is instead brought to the operating point by passing through stable states, which allows the activation of a frequency servo even during lock acquisition. Because of the weakness of the end mirror actuators, controlling CARM by feed-back to the laser frequency (and not to the end mirrors) is much more robust.

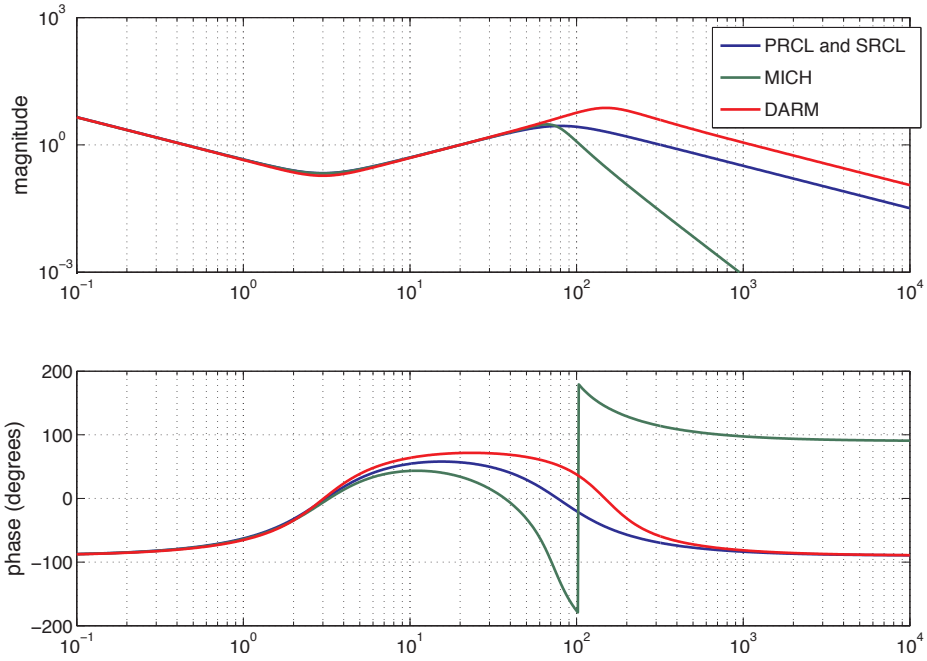

Figure 37: Control filters for DARM and the central cavity degrees of freedom. The corrections sent to the BS are further filtered in order to compensate for the double pendulum in the penultimate mass to mirror mechanical transfer function. The frequency servo is described in section 9.3.1.

Possible strategies for implementing a frequency servo during the locking sequence have been studied. The error signal of the frequency servo described in the previous section is a combination of the the arm cavities transmitted powers, TRX_DC and TRY_DC. A few hundred Hz is the maximum loop bandwidth which can be achieved with the current LIGO digital system. A high bandwidth analog frequency servo is likely not to be mandatory for acquiring the lock, but it might turn out to be useful. The implementation of a high bandwidth analog frequency servo using the arm cavities transmitted power as error signal, even if it is possible, would require a non negligible commissioning time because of the kilometric distance between the end stations and the laser. Moreover, for the same reason, not more than a few kHz of bandwidth will probably be achieved. One solution could be the use of the DC signal in reflection from the IFO ($REFL\_DC$), which is sensitive to CARM. Since this signal is nearly AC coupled (as shown in figure 39), another signal would need to be used at low frequency.

A possible implementation, similar to the strategy used to lock the LIGO-40m prototype, is the following:

- beginning of the locking sequence: $\sqrt{TRX + TRY}$ as error signal, digital loop, low bandwidth (∼200Hz);

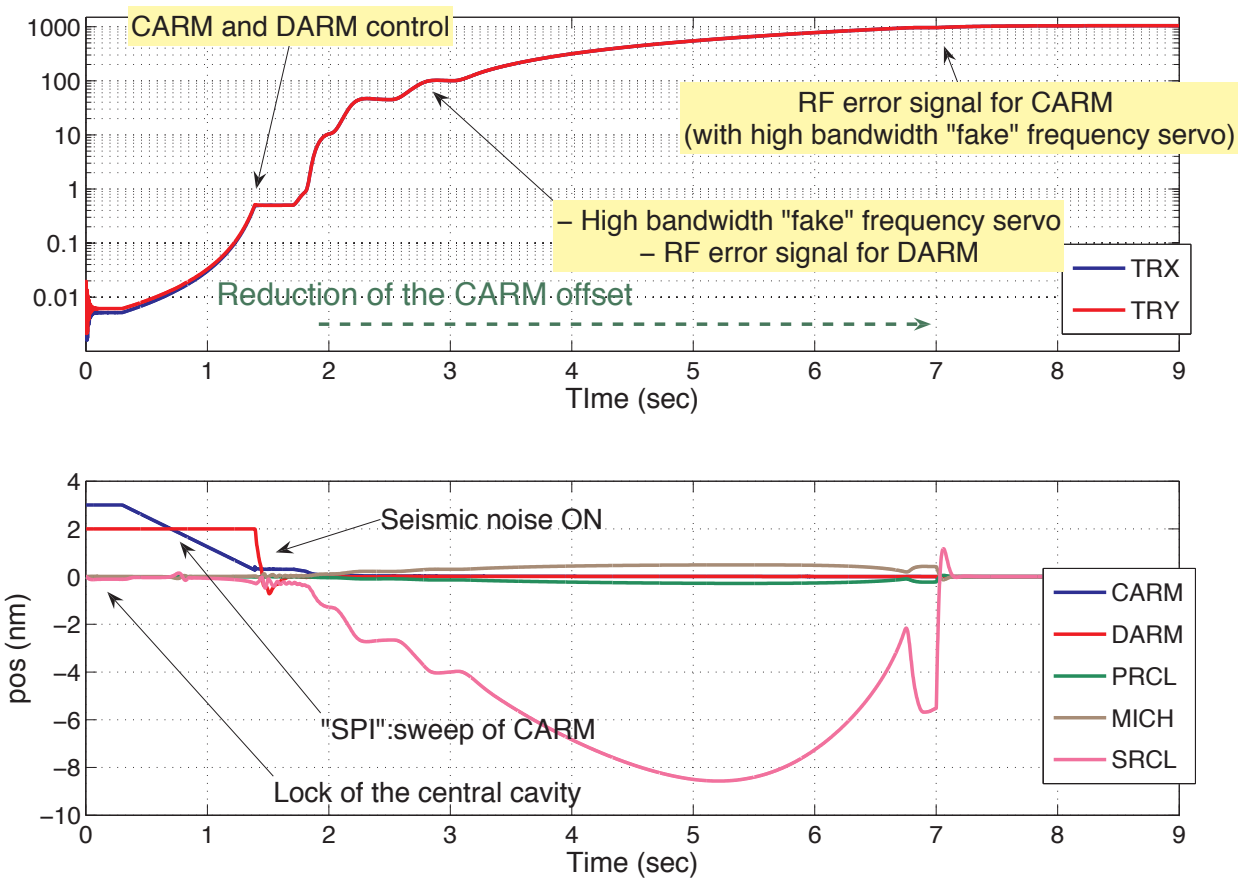

Figure 38: Full lock acquisition sequence.

- during the sequence: combination of $\sqrt{TRX + TRY}$)(digital, DC − 50Hz) and $REFL\_DC$ (analog, 50 Hz - 20 kHz);
- final state: REFL I1 as error signal, analog loop, high bandwidth ($\sim 20kHz$).

This strategy has been tested in simulation. The effect of a frequency servo has been reproduced by a "fake" servo in which the CARM correction signal is sent to the end mirrors by-passing the mechanics and therefore avoiding saturations. In the lock acquisition sequence shown in figure 38, the switch from a low bandwidth to a high bandwidth loop is done when the arm cavity transmitted power is about 100 times the single cavity power. The reason for this is that $REFL\_DC$ does not appear to be very sensitive to CARM in presence of bigger CARM offsets. However, a deep investigation on this point has not been done yet, and a transition at an earlier stage might be possible anyway.

9.4 Read-out noise requirements

The design of signal read-out is typically done in order to produce signals which are shot noise limited. However, this constraint is not really necessary during lock acquisition, where we are not concerned about sensitivity issues. Since the lock acquisition scheme involves

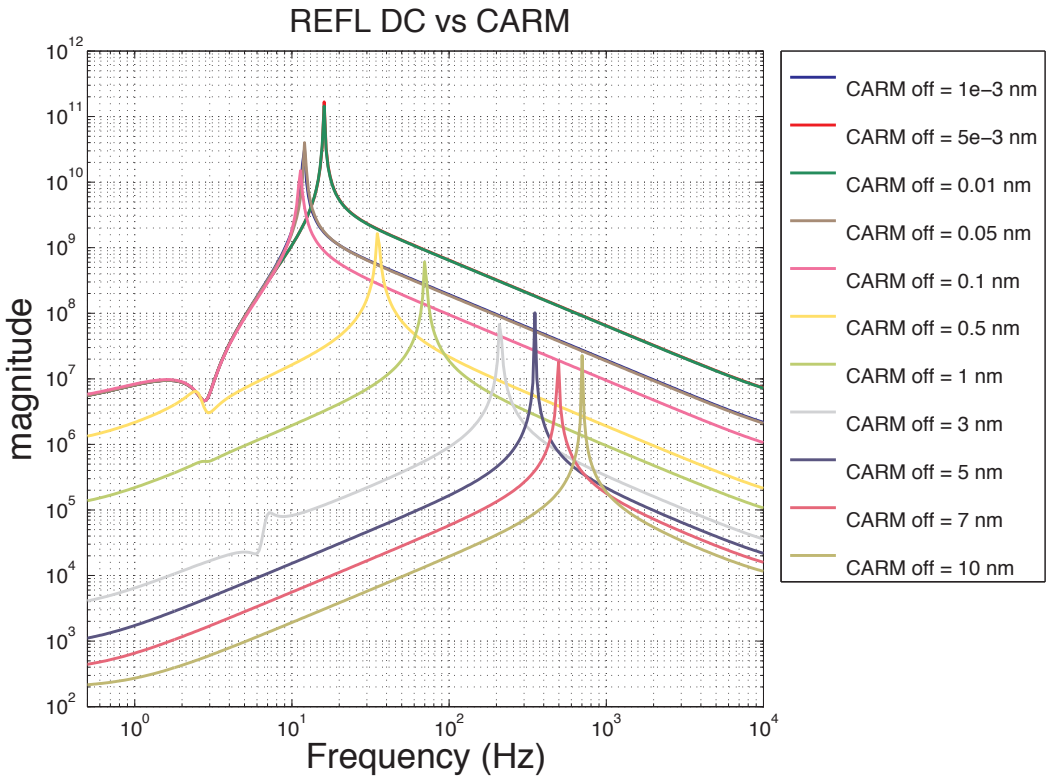

Figure 39: Frequency response of $REFL\_DC$ to a CARM motion.

signals at quite high frequency, like REFL 32 at 141 MHz, is useful to know the tolerance that we have on the read-out noise (amplifier noise, Johnson noise, etc..), in order to possibly simplify the read-out design for lock acquisition.

In the following part the only requirement that we impose on the performance of the read-out system is that the RMS of the correction signals sent to each mirror are at least a factor 10 lower than the relative actuator limit, in order to be safely far from saturations. The maximum correction signal (RMS) acceptable on each mirror according to this criterium is summarized in table 16:

Mirror	**Max correction signal (RMS)**
ETMX, ETMY	20 μN
PRM, SRM	1 mN
BS	60 mN

Table 16: Summary of the maximum correction signal (RMS) allowed for each mirror.

The control filters used for the analysis which follows are the ones shown in figure 37. A maximum incident DC power of 10mW on each diode and a diode efficiency η equal to 1, will be considered.

Mirror	Corrections shot noise limited (RMS)
PRM:	4×10^{-6} N
BS:	$\mathbf{4 \times 10^{-3}}$**N**
SRM:	1.4×10^{-5} N

Table 17: RMS of the correction signal (shot noise limited) sent o to each mirror.

9.4.1 RF Photodiodes at the reflection port: REFL31 and REFL32

At the reflection port signals are extracted both at 28 MHz and 141 MHz. At the beginning of the locking sequence, all the input power is reflected back from the IFO, so that a 99% attenuator is needed on this path in order to have 10 mW on each diode. This condition corresponds to the worse case in terms of level of shot noise. The power impinging upon the diode is mostly carrier power, which contributes only to increase the shot noise, but not to make signal (produced by the beating between the sideband). The maximum shot noise level, both in power and in current, is therefore:

$$\widetilde{P}_{shot} = \sqrt{1 h\nu P_0/\eta} = 4.5 \times 10^{-11} \text{ W}/\sqrt{\text{Hz}} \tag{9.1}$$

$$\widetilde{I}_{shot} = \frac{\eta e}{h\nu} \widetilde{P}_{shot} = 3.3 \times 10^{-11} \text{ A}/\sqrt{\text{Hz}} \tag{9.2}$$

where $P_0 = 10$mW. The most stringent constraint for setting the requirements on the read-out noise performance of REFL 31 and REFL32 is expected to come by the BS control. In fact, since the actuation from the BS is done from the PM (cite??), an f^3 controller is needed in order to compensate for the PM to mirror transfer function (instead of an f controller). Since the noise is propagated to the mirror through the control filter, this makes the re-injected noise grow by a factor f^2 faster than in the other loops. On the other hand, the BS actuator limit is only a factor 60 bigger than PRM and SRM's one.

The possibility of controlling the BS position using both REFL 31 and REFL 32 is considered.

I) REFL31 (MICH controlled by REFL31_Q)

For each mirror of the central cavity, the RMS of the correction signal shot noise limited, measured in simulation, is shown in table 17.

As said above, the BS actuator limit is 60 times bigger than for PRM and SRM, while the RMS of its correction signal is more than a factor 100 bigger. It is therefore the BS control which sets the requirement for the maximum allowed read-out noise (called generically electronic noise), which can be a factor 15 above shot noise:

$$\widetilde{P}_{elect} = 6.75 \times 10^{-10} \text{ W}/\sqrt{\text{Hz}} \tag{9.3}$$

$$\widetilde{I}_{elect} = 4.95 \times 10^{-10} \text{ A}/\sqrt{\text{Hz}} \tag{9.4}$$

II) REFL32 (MICH controlled by REFL32_Q)

Mirror	Corrections shot noise limited (RMS)
PRM:	2.0x10^{-6} N
BS:	**1.7x10^{-3}N**
SRM:	1.1x10^{-5} N

Table 18: RMS of the correction signal (shot noise limited) sent o to each mirror.

For each mirror of the central cavity, the RMS of the correction signal shot noise limited, measured in simulation, is:

With the same argument as before, the maximum electronic noise allowed can be about factor 30 above shot noise:

$$\widetilde{P}_{elect} = 1.35 \times 10^{-9} \text{ W}/\sqrt{\text{Hz}} \tag{9.5}$$
$$\widetilde{I}_{elect} = 9.90 \times 10^{-10} \text{ A}/\sqrt{\text{Hz}} \tag{9.6}$$

9.4.2 DC Photodiodes in transmission to the arms: TRX and TRY

DC signals transmitted to the arms are used during lock acquisition. The maximum power on the diodes is achieved at the end of the locking sequence: 31.5 mW. An about 75% attenuator is therefore needed in order to have a maximum power of about 10 mW on the diodes. The signal to shot noise ratio in this case is proportional to the square root of the power impinging upon the diode, so that the worse condition arises at the beginning of the locking sequence, when the power on the diode is the lowest one (about $P_0 = 3.7\mu W$). The shot noise level, both in power and in current, is:

$$\widetilde{P}_{shot} = \sqrt{2hvP_0/\eta} = 1.2 \times 10^{-12} \text{ W}/\sqrt{\text{Hz}} \tag{9.7}$$
$$\widetilde{I}_{shot} = \frac{\eta e}{hv}\widetilde{P}_{shot} = 9.8 \times 10^{-13} \text{ A}/\sqrt{\text{Hz}} \tag{9.8}$$

Measurements in simulation give an RMS of the correction signals sent to the end mirrors of 3.4x10^{-6} N. Since the maximum RMS allowed for the end mirrors is 20x10^{-6} N, the maximum photodiode noise allowed can be about factor 5 above shot noise:

$$\widetilde{P}_{elect} = 6.0 \times 10^{-12} \text{ W}/\sqrt{\text{Hz}} \tag{9.9}$$
$$\widetilde{I}_{elect} = 4.9 \times 10^{-12} \text{ A}/\sqrt{\text{Hz}} \tag{9.10}$$

9.4.3 RF Photodiode at the anti-symmetric port: AS2

During the locking sequence, when the arm transmitted power is about 100 times bigger than the single Fabry-Perot cavity power, the DARM control is moved form a DC to the RF

signal at the second modulation frequency, about 46 MHz. The power at the anti-symmetric port is about 4.6 mW. Since this is the gravitational wave signal port, not more than 1% is likely to be available for lock acquisition photodiodes. For this reason, we consider having a power on the diode of about $P_0 = 46\mu$W. This power is dominated by the f2 sideband power, since the carrier and the f1 sidebands are not resonant inside the signal recycling cavity, and they are poorly transmitted to the anti-symmetric port. The f2 sideband power is also contributing to make signal, so that the shot noise level, both in power and in current, is given by:

$$\widetilde{P}_{shot} = \sqrt{1.5 h\nu P_0/\eta} = 3.7 \times 10^{-12}\ \mathrm{W}/\sqrt{\mathrm{Hz}} \tag{9.11}$$

$$\widetilde{I}_{shot} = \frac{\eta e}{h\nu}\widetilde{P}_{shot} = 3.0 \times 10^{-12}\ \mathrm{A}/\sqrt{\mathrm{Hz}} \tag{9.12}$$

The maximum photodiode noise can be up to a factor 3000 above shot noise:

$$\widetilde{P}_{elect} = 1.1 \times 10^{-8}\ \mathrm{W}/\sqrt{\mathrm{Hz}} \tag{9.13}$$

$$\widetilde{I}_{elect} = 9.0 \times 10^{-9}\ \mathrm{A}/\sqrt{\mathrm{Hz}} \tag{9.14}$$

9.4.4 Summary

Table 19 summarizes all the results obtained before.

Photodiode	**Signal**	**Power**	**Shot noise limit**$(\mathrm{A}/\sqrt{\mathrm{Hz}})$	**Max elect noise**$(\mathrm{A}/\sqrt{\mathrm{Hz}})$
REFL 31	RF	10 mW	3.3×10^{-11}	($\times$**15**) 4.9×10^{-10}
REFL 32	RF	10 mW	3.3×10^{-11}	($\times$**30**) 9.9×10^{-10}
TRX , TRY	DC	3.7 μW	9.8×10^{-13}	($\times$**5**) 4.9×10^{-12}
AS2	RF	46 μW	3.0×10^{-12}	($\times$**3000**) 9.0×10^{-9}

Table 19: Summary of the specifications for each photodiode.

10 List of changes (V00 to V01)

- Section 2.2.2 More text to explain SRM tuning.
- Section 2.2.5 Section rewritten for clarity.
- Figure 6: More explanation in caption.
- Section 2.5 "(Electrical) RF power at sensing ports" added
- Section 3.3 Added comments to shot noise and oscillator phase noise.

- Figure 15: Added MICH noise budget for zero detuning.
- Figure 16: Added illustration for MICH and SRCL correction paths.
- Section 3.5 Rewrote first paragraph.

A Appendix: Full sensing matrix

Figures 20 and 21 show the full sensing matrix at 1 kHz for the NS/NS tuning and the zero-detuning case.

B Appendix: Sensing marix with and without Mach Zehnder

The following tables compare the sensing matrices with (table 22, 24, 26, 28) and without Mach Zehnder (table 23, 25, 27, 29) . They are calculated for the NS/NS (mode 2) (22, 23, 24, 25) and the no detuning case (mode 1b) (26, 27, 28, 29) , both at 20 Hz and 1 kHz. The only matrix elements that show a significant change are highlighted in magenta. The units for all matrices are Watts per meter.

Also figure 40 shows the REFL IM and IP double demodulation signal as a function of the SRC cavity detuning.

Port	CARM	DARM	PRCL	MICH	SRCL	IMCL
REFL DC	1.1e+07	9.1e+04	2e+06	1e+06	4.6e+05	0.0055
REFL I1	**9.4e+08**	2e+05	7.3e+07	1.1e+06	**5.5e+03**	0.49
REFL Q1	6.2e+05	1.5e+03	1.9e+06	5.2e+04	8.6e+02	0.00032
REFL IM	1.4e+06	**2.5e+04**	**5.1e+06**	4.5e+05	**2.8e+05**	0.00074
REFL QM	4.9e+06	5.9e+04	3e+06	1e+06	8.5e+04	0.0025
REFL IP	1.4e+06	2.6e+04	5e+06	4.6e+05	2.8e+05	0.00075
REFL QP	4.9e+06	5.8e+04	3.1e+06	1e+06	8.5e+04	0.0026
REFL I2	5.7e+08	1.3e+05	1.6e+07	1.5e+06	2.5e+05	0.29
REFL Q2	6.1e+08	1.9e+05	5.3e+06	3e+06	4.7e+04	0.31
AS DC	1.3e+06	**4.2e+09**	2.8e+05	1.5e+07	7.6e+06	0.00066
AS I1	1.4e+05	1.2e+07	5.5e+04	4e+04	2.7e+04	7.4e-05
AS Q1	2.9e+04	6.8e+06	4.9e+03	5.9e+04	1.3e+04	1.5e-05
AS IM	3e+03	3.5e+03	2.1e+03	2.9e+03	3.7e+02	1.6e-06
AS QM	2.2e+03	7.6e+03	3.4e+03	4.5e+03	1.6e+02	1.1e-06
AS IP	2.9e+03	6.2e+03	5.3e+02	3.8e+03	1.1e+02	1.5e-06
AS QP	1e+03	5.6e+03	3.5e+03	1.3e+03	3.9e+02	5.3e-07
AS I2	2e+06	6.2e+07	5.3e+05	2.4e+05	1e+05	0.001
AS Q2	2.6e+06	7e+07	2.1e+05	2.2e+05	9.4e+04	0.0013
POX DC	2.7e+05	5.4e+07	1.7e+05	1.7e+05	4.4e+04	0.00014
POX I1	3.1e+07	2.5e+06	**1.2e+07**	5.8e+04	6.5e+03	0.016
POX Q1	3.6e+06	2.8e+05	2.4e+05	8.2e+03	1.3e+03	0.0019
POX IM	1.6e+05	2.2e+03	6.7e+04	2.6e+04	1.5e+04	8e-05
POX QM	1.9e+05	3.5e+03	1.3e+05	4e+04	2.3e+03	9.9e-05
POX IP	1.5e+05	2.5e+03	7e+04	2.6e+04	1.5e+04	8e-05
POX QP	1.7e+05	3.3e+03	9.1e+04	4.1e+04	2.3e+03	8.8e-05
POX I2	4.2e+06	8.2e+05	2.4e+06	1.5e+05	**4.6e+04**	0.0022
POX Q2	1.5e+07	1.2e+06	**2.1e+06**	**5.3e+05**	4.2e+04	0.0079
POY DC	9.1e+04	5.5e+07	4.1e+04	2.1e+05	4.1e+04	4.7e-05
POY I1	3.1e+07	2.6e+06	**1.2e+07**	4.7e+04	7.3e+03	0.016
POY Q1	3.6e+06	3e+05	2.5e+05	1.3e+04	1.3e+03	0.0019
POY IM	3.4e+04	8.7e+02	6.7e+04	1.3e+04	5.7e+03	1.8e-05
POY QM	1.6e+05	1.3e+03	8.5e+04	2.3e+04	3.3e+03	8.3e-05
POY IP	3.3e+04	5.6e+02	6.5e+04	1.3e+04	5.7e+03	1.7e-05
POY QP	1.5e+05	1.5e+03	7e+04	2.3e+04	3.3e+03	7.9e-05
POY I2	9.9e+06	6.4e+05	2.7e+06	1.5e+05	**1.1e+04**	0.0051
POY Q2	1.1e+07	8.2e+05	**6.5e+05**	**3.3e+05**	2.5e+04	0.0059
POB DC	3e+05	5.4e+07	1.8e+05	2.3e+05	4.4e+04	0.00015
POB I1	3.2e+07	3.7e+06	**1.2e+07**	4.9e+04	7.3e+03	0.016
POB Q1	3.7e+06	4.1e+05	2.5e+05	2e+04	3.4e+02	0.0019
POB IM	1.6e+05	2.4e+03	6.9e+04	2.7e+04	1.5e+04	8.5e-05
POB QM	1.9e+05	3.7e+03	1.4e+05	4.1e+04	2.3e+03	0.0001
POB IP	1.6e+05	2.7e+03	7.1e+04	2.6e+04	1.5e+04	8.4e-05
POB QP	1.7e+05	3.4e+03	9.4e+04	4.2e+04	2.3e+03	9e-05
POB I2	4.3e+06	8e+05	2.4e+06	1.6e+05	**4.6e+04**	0.0022
POB Q2	1.6e+07	1.8e+06	**2.2e+06**	**6e+05**	4.7e+04	0.0082
POP1 DC	1.7e+05	2e+04	1e+05	3e+04	4.6e+03	8.6e-05
POP1 I1	3.1e+07	6.5e+03	**1.2e+07**	6.1e+03	3e+02	0.016
POP1 Q1	3.6e+06	7.4e+02	2.4e+05	1.9e+03	12	0.0019
POP1 IM	1.1e+05	8.3e+02	3.4e+04	1.6e+04	9.4e+03	5.9e-05
POP1 QM	1.7e+05	1.9e+03	1.1e+05	3.3e+04	2.8e+03	8.6e-05
POP1 IP	1.1e+05	8.3e+02	3.5e+04	1.5e+04	9.4e+03	5.9e-05
POP1 QP	1.5e+05	1.9e+03	8.3e+04	3.3e+04	2.8e+03	7.9e-05
POP1 I2	5.7e+06	8.3e+02	2.6e+06	1.5e+05	**2.7e+04**	0.003
POP1 Q2	1.4e+07	2.3e+04	**1.4e+06**	**4.2e+05**	2.9e+04	0.0074
POP2 DC	1.7e+05	2.1e+04	1e+05	3.1e+04	4.9e+03	8.6e-05
POP2 I1	3.2e+07	6.7e+03	**1.2e+07**	**6.8e+03**	**3.1e+02**	0.017
POP2 Q1	3.7e+06	7.5e+02	2.5e+05	1.9e+03	12	0.0019
POP2 IM	1.2e+05	8.6e+02	3.7e+04	1.6e+04	9.8e+03	6.1e-05
POP2 QM	1.7e+05	1.9e+03	1.1e+05	3.5e+04	2.9e+03	8.9e-05
POP2 IP	1.2e+05	8.6e+02	3.9e+04	1.6e+04	9.8e+03	6.1e-05
POP2 QP	1.6e+05	1.9e+03	8.6e+04	3.5e+04	2.9e+03	8.2e-05
POP2 I2	6.2e+06	8.6e+02	2.6e+06	1.5e+05	2.8e+04	0.0032
POP2 Q2	1.5e+07	2.3e+04	**1.4e+06**	**4.3e+05**	**3e+04**	0.0076
OMC DC	4.4e+07	7.1e+05	2e+07	1.2e+07	7.3e+06	0.023
OMC I1	6.1e+03	1.2e+04	3.3e+03	3e+03	2.9e+02	3.1e-06
OMC Q1	5.4e+02	1.7e+05	6.9e+02	1.1e+03	4.1e+02	2.8e-07
OMC IM	1.1e+06	2.2e+04	1.8e+06	4.7e+05	2.2e+05	0.00057
OMC QM	1.7e+06	3.1e+04	1.3e+06	2.8e+06	3.3e+03	0.00088
OMC IP	1e+06	2e+04	1.8e+06	1.8e+05	2.2e+05	0.00052
OMC QP	1.3e+06	1.1e+04	6.3e+05	2.2e+06	5e+03	0.00068
OMC I2	1.7e+03	5.5e+06	1.9e+02	1.9e+04	3.2e+03	9.1e-07
OMC Q2	3.6e+02	1e+06	87	3.1e+03	5.8e+02	1.9e-07
TRX DC	7.8e+02	2.4e+06	1.8e+02	8.3e+03	1.9e+03	4e-07
TRY DC	6.8e+02	2.4e+06	1.6e+02	8.3e+03	1.9e+03	3.5e-07

Table 20: Sensing matrix at 1000 Hz, NSNS tuning, no closed loops, calculated by Optickle. Bold red shows the main elements used for control. Alternative error signals and important cross-couplings are marked with different collors. POP1 is the power recycling cavity pick off for light travelling from the PRM to the BS, while POP2 sees the light travelling from BS to PRM. The contractions used in the port name are: I: I-phase, Q: Q-phase, 1: demodulated at f_1, 2: demodulated at f_2, M: demodulated at $f_2 - f_1$, P: demodulated at $f_2 + f_1$. The units are Watts per meter.

Port	CARM	DARM	PRCL	MICH	SRCL	IMCL
REFL DC	1.7e+06	3e+04	5e+03	3.3e+04	5e+02	0.0009
REFL I1	**9.4e+08**	1.3e+05	7.3e+07	1e+06	**1.4e+04**	0.49
REFL Q1	7.4e+05	2.9e+03	2e+06	7.3e+04	3.1e+03	0.00038
REFL IM	1e+03	**2e+02**	**1e+03**	3.1e+02	92	5.4e-07
REFL QM	4.5e+03	6.2e+02	6.3e+02	7.7e+02	35	2.3e-06
REFL IP	2.7e+03	4.8e+02	1.1e+03	5.9e+02	89	1.4e-06
REFL QP	3.4e+03	4.5e+02	5.5e+02	6e+02	34	1.8e-06
REFL I2	4.3e+08	1.4e+05	8.6e+06	1.9e+06	1.9e+06	0.22
REFL Q2	3.6e+08	3e+05	9.9e+06	5.1e+06	2.8e+05	0.19
AS DC	3e+06	**9.7e+09**	6.7e+05	3.4e+07	7e+03	0.0016
AS I1	1.3e+05	3.3e+07	5.1e+04	1.3e+05	5.6e+03	6.8e-05
AS Q1	6.7e+04	1.7e+07	1.9e+04	5.3e+04	2.7e+03	3.5e-05
AS IM	2.1e+02	0.78	0.99	34	8.8	1.1e-07
AS QM	4.2e+02	1.1	1.3	18	19	2.2e-07
AS IP	3.6e+02	0.95	1.2	17	16	1.9e-07
AS QP	3.1e+02	0.97	1.1	19	14	1.6e-07
AS I2	5.8e+05	1.3e+08	1.3e+05	5e+05	9.7e+03	0.0003
AS Q2	7.5e+05	2e+08	5.8e+04	7.3e+05	2.7e+04	0.00039
POX DC	4.1e+04	7.2e+05	9e+03	4.8e+03	1.4e+05	2.1e-05
POX I1	3.1e+07	7.8e+06	**1.2e+07**	4.6e+04	1.2e+03	0.016
POX Q1	3.6e+06	8.7e+05	2.4e+05	1e+04	6.5e+02	0.0019
POX IM	1e+02	1.4	15	11	7.8	5.4e-08
POX QM	32	1.2	17	3.2	3.7	1.6e-08
POX IP	1.1e+02	1.5	16	11	8.1	5.8e-08
POX QP	28	1	7.8	3.1	3.4	1.4e-08
POX I2	6.1e+06	1.4e+06	1.7e+06	4.5e+04	**4.3e+05**	0.0032
POX Q2	1.2e+07	3.3e+06	**1.1e+06**	**9.5e+05**	2.2e+05	0.0064
POY DC	4.2e+04	7.5e+05	9.3e+03	3.6e+03	1.4e+05	2.2e-05
POY I1	3.1e+07	8e+06	**1.2e+07**	3.9e+04	1.6e+03	0.016
POY Q1	3.6e+06	9e+05	2.5e+05	1.5e+04	6.6e+02	0.0019
POY IM	95	1.3	5.1	2.7	4.6	4.9e-08
POY QM	20	0.42	14	0.61	1.1	1e-08
POY IP	95	1.3	7.7	2.6	4.8	4.9e-08
POY QP	19	0.52	9.2	1.2	0.76	9.7e-09
POY I2	1.1e+07	2.8e+06	1.7e+06	1.5e+05	**1.4e+05**	0.0056
POY Q2	5e+06	1.3e+06	**3.9e+05**	**4.9e+05**	1.2e+05	0.0026
POB DC	4.4e+04	9.2e+05	9.9e+03	3.6e+03	1.4e+05	2.3e-05
POB I1	3.2e+07	8.9e+06	**1.2e+07**	4.1e+04	1.7e+03	0.016
POB Q1	3.7e+06	9.9e+05	2.5e+05	1.8e+04	4.1e+02	0.0019
POB IM	1.2e+02	1.4	16	11	8.1	6.1e-08
POB QM	33	1.2	17	3.4	4.1	1.7e-08
POB IP	1.3e+02	1.5	17	11	8.4	6.5e-08
POB QP	29	1	7.7	3.4	3.7	1.5e-08
POB I2	6.3e+06	1.6e+06	1.8e+06	3.3e+04	**4.4e+05**	0.0032
POB Q2	1.3e+07	3.7e+06	**1.2e+06**	**9.9e+05**	2.2e+05	0.0067
POP1 DC	4.3e+02	4.7e+03	13	4.8e+03	59	2.2e-07
POP1 I1	3.1e+07	4.3e+03	**1.2e+07**	5.9e+03	2.9e+02	0.016
POP1 Q1	3.6e+06	5e+02	2.4e+05	2e+03	12	0.0019
POP1 IM	36	1.1	17	5	3.1	1.9e-08
POP1 QM	12	0.89	6.3	4	1.1	6.1e-09
POP1 IP	38	1.2	14	5	3.1	2e-08
POP1 QP	12	0.87	3.5	4	1.1	6.1e-09
POP1 I2	8.3e+06	8.8e+03	1.7e+06	9.7e+04	**2.9e+05**	0.0043
POP1 Q2	8.7e+06	4.1e+04	**4.5e+05**	**7.2e+05**	8.6e+04	0.0045
POP2 DC	4.3e+02	4.8e+03	15	4.9e+03	61	2.2e-07
POP2 I1	3.2e+07	4.4e+03	**1.2e+07**	**6.6e+03**	**3e+02**	0.017
POP2 Q1	3.7e+06	5.1e+02	2.5e+05	2e+03	11	0.0019
POP2 IM	37	1.2	18	5.4	3.3	1.9e-08
POP2 QM	14	0.75	6.3	4.5	1.1	7.2e-09
POP2 IP	39	1.2	15	5.4	3.3	2e-08
POP2 QP	14	0.76	3.5	4.4	1.1	7.1e-09
POP2 I2	8.7e+06	9e+03	1.8e+06	9.9e+04	**3e+05**	0.0045
POP2 Q2	8.7e+06	4.2e+04	**4.6e+05**	**7.4e+05**	**8.8e+04**	0.0045
OMC DC	3.9e+04	1e+03	9e+03	7.6e+03	2.8e+03	2e-05
OMC I1	8.5e+03	3.4e+05	2.5e+03	2.9e+03	1.7e+03	4.4e-06
OMC Q1	2.4e+03	2.8e+05	9.6e+02	1.1e+03	1.2e+03	1.3e-06
OMC IM	7.1e+02	18	2e+02	74	72	3.7e-07
OMC QM	4.7e+02	14	94	3e+02	37	2.4e-07
OMC IP	9.3e+02	25	1.5e+02	3.3e+02	75	4.8e-07
OMC QP	4e+02	11	1.1e+02	18	38	2.1e-07
OMC I2	4.6e+03	1.4e+07	8.6e+02	5e+04	2.3e+03	2.4e-06
OMC Q2	23	1.3e+04	56	5.1e+02	2.2	1.2e-08
TRX DC	69	4e+03	18	32	6e+03	3.6e-08
TRY DC	98	4e+03	18	36	6e+03	5.1e-08

Table 21: Sensing matrix at 1000 Hz, zero detuning, no closed loops, calculated by Optickle. Bold red shows the main elements used for control. Alternative error signals and important cross-couplings are marked with different collors. POP1 is the power recycling cavity pick off for light travelling from the PRM to the BS, while POP2 sees the light travelling from BS to PRM. The contractions used in the port name are: I: I-phase, Q: Q-phase, 1: demodulated at f_1, 2: demodulated at f_2, M: demodulated at $f_2 - f_1$, P: demodulated at $f_2 + f_1$. The units are Watts per meter.

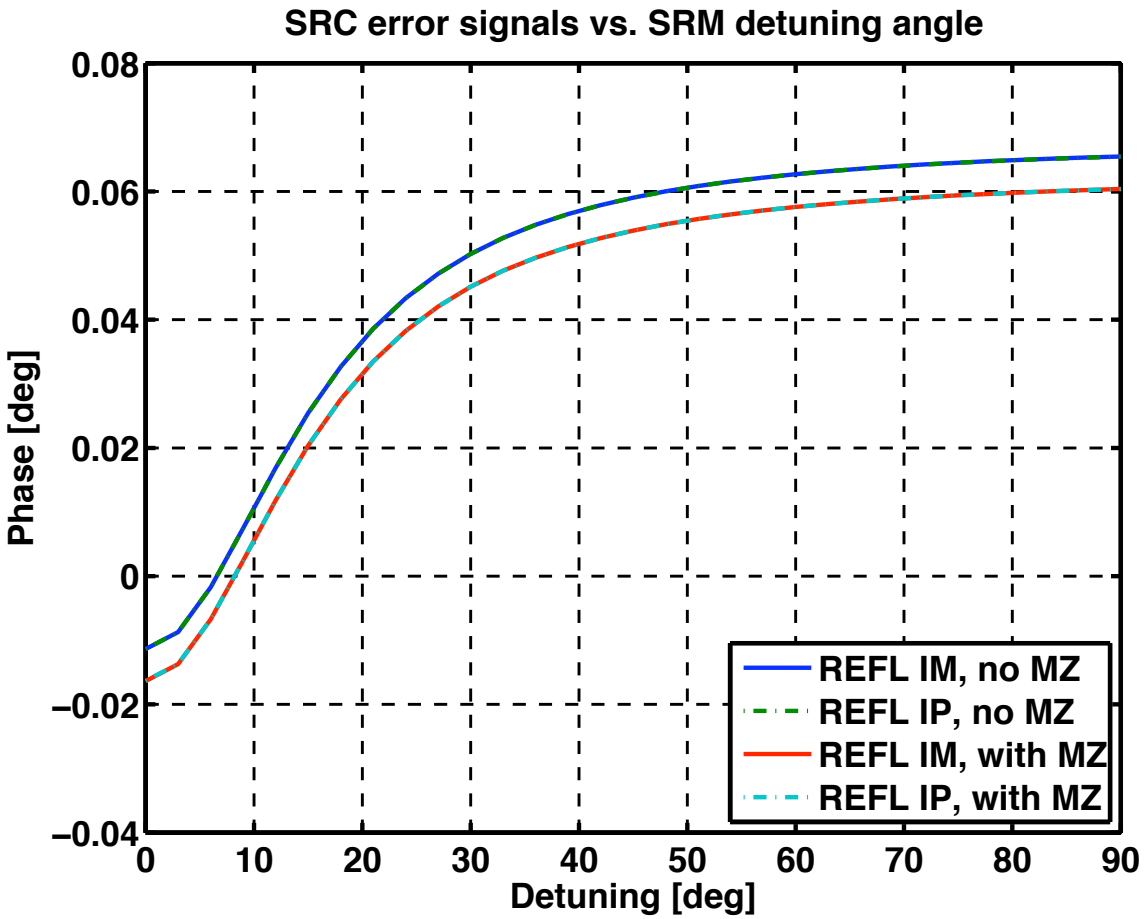

Figure 40: REFL double demodulation error signals with and without a Mach-Zehnder Interferometer. The difference is due to direct beating of 4xf1 and 6xf1 sidebands against the carrier, and hence is proportional to amount of carrier reflected from the interferometer.

Port	CARM	DARM	PRCL	MICH	SRCL	IMCL
REFL I1	**2.8e+09**	7.7e+07	1.5e+08	3e+06	**2e+05**	1.5
AS DC	1.4e+06	**3.8e+09**	2.7e+05	1.3e+07	1.1e+07	0.0007
POX I1	3.2e+07	2.1e+06	**1.3e+07**	**1.1e+04**	**6.6e+03**	0.016
POX Q2	4.6e+06	4.4e+05	**1.5e+06**	**1.3e+06**	**1.1e+04**	0.0024
REFL IM	2.3e+05	**3e+05**	**2.7e+07**	4.1e+05	**2.1e+06**	0.00012
REFL I2	5.1e+08	1.4e+07	4.3e+07	2.9e+05	9.2e+05	0.26
POX I2	1.9e+07	1.2e+06	3.8e+06	9.4e+02	8.5e+04	0.0099
IMC I3	7.3e+09	0	0	0	0	**0.0083**

Table 22: Sensing matrix at 20 Hz with Mach-Zehnder, NSNS tuning

Port	CARM	DARM	PRCL	MICH	SRCL	IMCL
REFL I1	**2.8e+09**	7.7e+07	1.5e+08	3e+06	**1.4e+05**	1.5
AS DC	1.4e+06	**3.8e+09**	2.7e+05	1.3e+07	1.2e+07	0.0007
POX I1	3.2e+07	2.1e+06	**1.4e+07**	**1.1e+04**	**6.6e+03**	0.016
POX Q2	4.6e+06	4.5e+05	**1.5e+06**	**1.3e+06**	**1.1e+04**	0.0024
REFL IM	2.4e+05	**3.3e+05**	**2.7e+07**	4.2e+05	**2.1e+06**	0.00013
REFL I2	5.1e+08	1.5e+07	5.5e+07	3.7e+05	9.2e+05	0.26
POX I2	1.9e+07	1.2e+06	3.8e+06	9.5e+02	8.5e+04	0.0099
IMC I3	7.4e+09	0	0	0	0	**0.0083**

Table 23: Sensing matrix at 20 Hz no Mach-Zehnder, NSNS tuning

Port	CARM	DARM	PRCL	MICH	SRCL	IMCL
REFL I1	**2.8e+09**	5.9e+05	1.5e+08	3.3e+06	**4.1e+03**	1.4
AS DC	1.2e+06	**4.2e+09**	3e+05	1.5e+07	7.7e+06	0.00064
POX I1	3.1e+07	2.5e+06	**1.3e+07**	**1.9e+04**	**6.6e+03**	0.016
POX Q2	4.5e+06	6.1e+05	**1.5e+06**	**1.3e+06**	**1.1e+04**	0.0024
REFL IM	1.1e+07	**1.9e+03**	**2.6e+07**	4e+05	**2.1e+06**	0.0059
REFL I2	5e+08	1.4e+05	4.4e+07	3.2e+05	9.4e+05	0.26
POX I2	1.9e+07	9.8e+05	3.8e+06	4e+04	8.4e+04	0.0098
IMC I3	7.3e+09	0	0	0	0	**0.41**

Table 24: Sensing matrix at 1000 Hz with Mach-Zehnder, NSNS tuning

Port	CARM	DARM	PRCL	MICH	SRCL	IMCL
REFL I1	**2.8e+09**	5.9e+05	1.5e+08	3.3e+06	**6.5e+04**	1.4
AS DC	1.3e+06	**4.3e+09**	3e+05	1.5e+07	7.8e+06	0.00065
POX I1	3.1e+07	2.6e+06	**1.3e+07**	**1.9e+04**	**6.6e+03**	0.016
POX Q2	4.6e+06	6.1e+05	**1.5e+06**	**1.3e+06**	**1.1e+04**	0.0024
REFL IM	1.2e+07	**9.7e+03**	**2.6e+07**	4.1e+05	**2.1e+06**	0.006
REFL I2	5e+08	1.4e+05	5.6e+07	4e+05	9.4e+05	0.26
POX I2	1.9e+07	9.9e+05	3.8e+06	4e+04	8.5e+04	0.0099
IMC I3	7.3e+09	0	0	0	0	**0.41**

Table 25: Sensing matrix at 1000 Hz no Mach-Zehnder, NSNS tuning

Port	CARM	DARM	PRCL	MICH	SRCL	IMCL
REFL I1	**2.8e+09**	2.6e+08	1.5e+08	4.2e+06	**8.2e+05**	1.5
AS DC	5.8e+06	**1.6e+10**	1.4e+06	5.7e+07	4.9e+07	0.003
POX I1	3.2e+07	1e+07	**1.3e+07**	**3.1e+04**	**3e+04**	0.016
POX Q2	4.2e+06	1.3e+06	**7.3e+05**	**9.4e+05**	**1.6e+05**	0.0022
REFL IM	2.5	**27**	**2.5e+02**	7.6	6.7	2.2e-09
REFL I2	7.3e+08	6.8e+07	2.8e+07	1.5e+06	4.6e+06	0.38
POX I2	1.3e+07	4.1e+06	2.2e+06	3.5e+02	**3.9e+05**	0.0068
IMC I3	7.3e+09	0	0	0	0	**0.0083**

Table 26: Sensing matrix at 20 Hz with Mach-Zehnder, zero detuning

Port	CARM	DARM	PRCL	MICH	SRCL	IMCL
REFL I1	**2.8e+09**	2.6e+08	1.5e+08	4.2e+06	**1.2e+06**	1.5
AS DC	5.8e+06	**1.6e+10**	1.4e+06	5.7e+07	5e+07	0.003
POX I1	3.2e+07	1e+07	**1.4e+07**	**3.2e+04**	**3e+04**	0.016
POX Q2	4.2e+06	1.3e+06	**7.4e+05**	**9.5e+05**	**1.6e+05**	0.0022
REFL IM	1.4e+04	**1.3e+05**	**1.1e+02**	2e+03	4.2e+02	7.1e-06
REFL I2	7.4e+08	6.9e+07	4e+07	1.6e+06	4.6e+06	0.38
POX I2	1.3e+07	4.1e+06	2.2e+06	3.6e+02	**3.9e+05**	0.0068
IMC I3	7.4e+09	0	0	0	0	**0.0083**

Table 27: Sensing matrix at 20 Hz no Mach-Zehnder, zero detuning

C Appendix: Bench, Optickle and Looptickle simulation code and configuration files

Much of the LSC optimization was done with Bench62, Optickle and Looptickle. These software packages are available in CVS at *emvogil-3.mit.edu:/export/cvs/iscmodeling*

- Bench62
- Optickle
- Looptickle

Port	CARM	DARM	PRCL	MICH	SRCL	IMCL
REFL I1	**2.8e+09**	4e+05	1.5e+08	3.3e+06	**4.2e+03**	1.4
AS DC	2.9e+06	**9.8e+09**	6.8e+05	3.5e+07	7.2e+03	0.0015
POX I1	3.1e+07	7.8e+06	**1.3e+07**	**3.3e+04**	**1.2e+03**	0.016
POX Q2	4.1e+06	1e+06	**7.1e+05**	**9.4e+05**	**1.6e+05**	0.0021
REFL IM	1.2e+02	**0.41**	**2.5e+02**	6.3	6.7	6.5e-08
REFL I2	7.3e+08	1.1e+05	2.7e+07	1.2e+06	4.8e+06	0.38
POX I2	1.3e+07	3.2e+06	2.2e+06	1.8e+04	**4e+05**	0.0067
IMC I3	7.3e+09	0	0	0	0	**0.41**

Table 28: Sensing matrix at 1000 Hz with Mach-Zehnder, zero detuning

Port	CARM	DARM	PRCL	MICH	SRCL	IMCL
REFL I1	**2.8e+09**	4e+05	1.5e+08	3.3e+06	**3.6e+05**	1.5
AS DC	2.9e+06	**9.9e+09**	6.9e+05	3.5e+07	7.3e+03	0.0015
POX I1	3.1e+07	7.9e+06	**1.3e+07**	**3.4e+04**	**1.2e+03**	0.016
POX Q2	4.1e+06	1e+06	**7.2e+05**	**9.5e+05**	**1.6e+05**	0.0021
REFL IM	1.3e+04	**1.9e+03**	**1.4e+02**	1.9e+03	23	6.9e-06
REFL I2	7.4e+08	1.1e+05	3.9e+07	1.3e+06	4.8e+06	0.38
POX I2	1.3e+07	3.3e+06	2.2e+06	1.9e+04	**4e+05**	0.0068
IMC I3	7.3e+09	0	0	0	0	**0.41**

Table 29: Sensing matrix at 1000 Hz no Mach-Zehnder, zero detuning

Time domain simulations for lock acquisition have been developed using the LIGO time domain model E2E (*http://www.ligo.caltech.edu/ e2e/*).

References

[1] S. Ballmer, "LIGO Interferometer Operating as a Radiometer", `http://www.ligo.caltech.edu/docs/P/P060043-00.pdf`

[2] H. Grote, *High power, low-noise, and multiply resonant photodetector for interferometric gravitational wave detectors*, Rev. Sci. Instrum. **78,** 054704 (2007). LIGO-P-060032-00-Z.

[3] R. Abbott, *RFPD Topology Comparison*, LIGO-T060268-02-C.

[4] B. Lantz, *Development of Improved Photodiodes for Advanced LIGO*, LIGO-T070018-00-R.

[5] K. Kawabe, *Orientation of Quadrant Diode for Wave Front Sensing*, LIGO-T060035-0-D.

[6] P. Fritschel, *Backscattering from the AS port: Enhanced and Advanced LIGO*, LIGO-T060303-00-D.

[7] V. Mandic, *Estimate of the Beam Jitter at the Output Mode Cleaner*, LIGO-T060178-00-D.

[8] SPI feasibility study, to be distributed by ANU.

[9] Osamu Miyakawa et al. *J. Phys.: Conf. Ser.* **32** 265-269 (2006)

[10] K Arai et al. *Class. Quantum Grav.* **19** 1843-184 (2002)

[11] Miyakawa and Yamamoto *Lock Acquisition Studies for Advanced Interferometers*, Proceedings Amaldi 2007

[12] M.Evans et al. *Lock acquisition of a gravitational-wave interferometer*, Optics Letters vol.27, n.8, April 15 (2002)